THESIS FOR THE DEGREE OF DOCTOR OF PHILOSOPHY

Metal-exchanged zeolites for NH_3-SCR applications

Activity and Deactivation studies

Soran Shwan

Department of Chemical and Biological Engineering
CHALMERS UNIVERSITY OF TECHNOLOGY
Gothenburg, Sweden, 2014

CHALMERS

Metal-exchanged zeolites for NH_3-SCR applications
Activity and Deactivation studies
SORAN SHWAN

ISBN: 978-91-7597-103-2

Doktorsavhandlingar vid Chalmers tekniska högskola
Ny serie nr 3784
ISSN 0346-718X

Department of Chemical and Biological Engineering
Chalmers University of Technology
SE-412 96 Gothenburg
Sweden
Telephone + 46 (0)31-772 1000

Cover:
Iron-exchanged zeolite BEA showing different iron species. Further details about the figure can be found in section 9.3.

Chalmers Reproservice
Gothenburg, Sweden 2014

Metal-exchanged zeolites for NH_3-SCR applications

Activity and Deactivation studies

Soran Shwan
Department of Chemical and Biological Engineering
Chalmers University of Technology

Abstract

Emissions of nitrogen oxides (NO_X) formed during the burning process in internal combustion engines is a major contributor to global air pollutions. One effective way to reduce NO_X in lean environments, i.e. oxygen excess is selective catalytic reduction with ammonia (NH_3-SCR). Metal-exchanged zeolites have proven to be active as SCR catalysts, where copper and iron are the most common metals. When using metal-exchanged zeolites in exhaust aftertreatment systems, several challenges arise. Resistance towards hydrothermal deactivation and chemisorption of impurities on the active sites of the catalyst are two of the more important challenges. Temperatures between 600-700^oC can be seen during regeneration of the particulate filter, which usually is placed upstream close to the SCR catalyst in the exhaust aftertreatment system, and therefore hydrothermal stability of the metal-exchanged zeolite is crucial. Furthermore, high tolerance against catalyst poisons which originate from (bio-) fuels and lubricating oils is desired, where phosphorous and potassium are among the more important poisons.

In this thesis thermal and chemical deactivation of iron-exchanged zeolite BEA as SCR catalyst is experimentally studied with special focus paid on the active iron species. Based on the experimental results a kinetic model is developed to predict the decreased activity of the catalyst after deactivation. Several characterization techniques are used to evaluate and correlate structural changes in the catalyst with the decreased activity. Catalysts are prepared and characterized using BET, XPS, XRD, TPD, *in-situ* FTIR and UV-Vis. The catalytic performance of the samples is measured using a flow-reactor system.

It is concluded that the hydrothermal deactivation of Fe-BEA is a result of migration of isolated iron species forming iron cluster inside the zeolite pores and iron particles located on the external surface of the zeolite crystals. Further, it is shown that the growth of iron clusters and particles can be partially reversed by high temperature hydrogen treatment. The chemical deactivation due to phosphorous exposure is the result of formation of metaphosphates replacing hydroxyl groups on the active isolated iron species. Furthermore, the chemical deactivation of Fe-BEA by potassium is concluded to be due to exchange and loss of active isolated iron species in the zeolite forming smaller iron clusters inside the zeolite pores.

A kinetic model where different iron species are included was developed based on the hydrothermal deactivation experiments and validated using phosphorous and potassium exposed samples. By fitting and fix the kinetic parameters towards a fresh sample, the decreased SCR activity can be predicted by just decreasing the number of active iron sites, representing loss of active iron species due to hydrothermal treatment and poisoning.

The effect of gas atmosphere during solid-state ion-exchange of copper-zeolites was studied as well. It is concluded that copper becomes highly mobile due to formation of copper-ammine complexes in presence of NH_3 after reduction of Cu^{II} to Cu^{I} by adding NO in the exposing gas during the solid-state ion-exchange. Copper-exchanged zeolites could be prepared by exposing physical mixtures of copper-oxides with zeolites to NO and NH_3 at as low temperature as 250^oC.

Finally, the ammonia formation during the rich period of NO_X storage and reduction (NSR) cycles was studied using kinetic modeling for the possibility of combining NSR and SCR catalysts in the exhaust aftertreatment system. It is concluded that the formation of ammonia is due to stored NO_X and hydrogen from the gas in the first half of the catalyst. However, it was further concluded that the formation of ammonia is delayed due to formation of N_2O from stored NO_X and formed NH_3.

Keywords: Emissions, Nitrogen oxides, Catalyst, NH_3-SCR, Ammonia, Hydrothermal, Chemical, Deactivation, Ageing, Poisoning, Kinetic, modeling, Iron, Copper, Zeolite, NSR, NH_3, NO_X.

List of papers

This thesis is based on the work presented in the following publications

I. Hydrothermal stability of Fe-BEA as an NH_3-SCR catalyst
Soran Shwan, Radka Nedyalkova, Jonas Jansson, John Korsgren, Louise Olsson and Magnus Skoglundh
Industrial & Engineering Chemistry Research, 51 (39), (2012) 12762–12772.

II. Influence of hydrothermal ageing on NH_3-SCR over Fe-BEA – Inhibition of NH_3-SCR by ammonia
Soran Shwan, Radka Nedyalkova, Jonas Jansson, John Korsgren, Louise Olsson and Magnus Skoglundh
Topics in Catalysis, 56 (2013) 80-88.

III. Effect of thermal ageing on the nature of iron species in Fe-BEA
Soran Shwan, Emma Catherine Adams, Jonas Jansson and Magnus Skoglundh
Catalysis Letters, 143 (2013) 43-48.

IV. Improved low-temperature SCR activity for Fe-BEA catalysts by H_2-pretreatment
Radka Nedyalkova, Soran Shwan, Magnus Skoglundh and Louise Olsson
Applied Catalysis B: Environmental, 138-139 (2013) 373-380.

V. Effect of post-synthesis hydrogen-treatment on the nature of iron species in Fe-BEA as NH_3-SCR catalyst.
Soran Shwan, Jonas Jansson, Louise Olsson and Magnus Skoglundh
Catalysis Science & Technology, 4 (2014) 2932-2937.

VI. Chemical deactivation of Fe-BEA as NH_3-SCR catalyst – Effect of Phosphorous
Soran Shwan, Jonas Jansson, Louise Olsson and Magnus Skoglundh
Applied Catalysis B: Environmental, 147 (2014) 111-123.

VII. Chemical deactivation of H-BEA and Fe-BEA as NH_3-SCR catalysts – Effect of Potassium
Soran Shwan, Jonas Jansson, Louise Olsson and Magnus Skoglundh
Submitted for publication (2014).

VIII. Kinetic modeling of H-BEA and Fe-BEA as NH_3-SCR catalyst – Effect of hydrothermal treatment
Soran Shwan, Jonas Jansson, John Korsgren, Louise Olsson and Magnus Skoglundh
Catalysis Today, 197 (2012) 24-37.

IX. Kinetic deactivation model of Fe-BEA as NH_3-SCR catalyst – Effect of Phosphorous
Soran Shwan, Jonas Jansson, Louise Olsson and Magnus Skoglundh
Accepted for publication in AIChE Journal (2014).

X. **NH_3-SCR activity of H-BEA and Fe-BEA after potassium exposure**
Soran Shwan, Jonas Jansson, Louise Olsson and Magnus Skoglundh
Submitted for publication (2014).

XI. **Deactivation mechanisms of iron-exchanged zeolites for NH_3-SCR applications**
Soran Shwan, Jonas Jansson, Louise Olsson and Magnus Skoglundh
Submitted for publication (2014).

XII. **Solid-state ion-exchange of copper into zeolites facilitated by ammonia at low temperature**
Soran Shwan, Magnus Skoglundh, Lars F. Lundegaard, Ramchandra R. Tiruvalam, Ton V.W. Janssens, Anna Carlsson and Peter N.R. Vennestrøm
Accepted for publication in ACS Catalysis (2014).

XIII. **Kinetic modeling of NO_X storage and reduction – Using spatially resolved MS measurements**
Soran Shwan, William Partridge, Jae-Soon Choi and Louise Olsson
Applied Catalysis B: Environmental, 147 (2014) 1028-1041.

Contribution report

I. Performed the experimental work, interpreted the results together with my co-authors, wrote the first draft and wrote the manuscript together with my co-authors.

II. Performed the experimental work, interpreted the results together with my co-authors, wrote the first draft and wrote the manuscript together with my co-authors.

III. Performed the experimental work, interpreted the results together with my co-authors, wrote the first draft and wrote the manuscript together with my co-authors.

IV. Performed some of the experimental work, interpreted the results together with my co-authors and wrote the manuscript together with my co-authors.

V. Performed the experimental work, interpreted the results together with my co-authors, wrote the first draft and wrote the manuscript together with my co-authors.

VI. Performed the experimental work, interpreted the results together with my co-authors, wrote the first draft and wrote the manuscript together with my co-authors.

VII. Performed the experimental work, interpreted the results together with my co-authors, wrote the first draft and wrote the manuscript together with my co-authors.

VIII. Performed the experimental work, developed the kinetic model, interpreted the results together with my co-authors, wrote the first draft and wrote the manuscript together with my co-authors.

IX. Performed the experimental work, developed the kinetic model, interpreted the results together with my co-authors, wrote the first draft and wrote the manuscript together with my co-authors.

X. Performed the experimental work, developed the kinetic model, interpreted the results together with my co-authors, wrote the first draft and wrote the manuscript together with my co-authors.

XI. Performed the experimental work, developed the kinetic model, interpreted the results together with my co-authors, wrote the first draft and wrote the manuscript together with my co-authors.

XII. Performed the experimental work, interpreted the results together with my co-authors, wrote the first draft and wrote the manuscript together with my co-authors.

XIII. Developed the kinetic model, interpreted the results together with my co-authors, wrote the first draft and wrote the manuscript together with my co-authors.

Table of Contents

1 Introduction 1

2 Objective 3

3 Catalysis 5

4 NH_3-SCR 7

4.1 SCR chemistry 8

4.2 SCR catalysts 9

4.2.1 Metal-exchanged zeolites 10

4.3 Activity and deactivation 10

4.3.1 Hydrothermal deactivation 11

4.3.2 Chemical poisoning 12

5 NO_X storage and reduction 13

5.1 Materials 13

5.2 NO_X storage 13

5.3 NO_X reduction 14

5.4 Combining NSR and NH_3-SCR 14

6 Experimental methods 15

6.1 Sample preparation 15

6.2 Hydrothermal treatment and chemical deactivation 15

6.3 Flow reactor system 16

6.4 Sample characterization 16

6.5 Activity measurements 18

7 Theory and modeling 19

7.1 Reactor model 19

7.2 Kinetic parameters 20

7.2.1 Thermodynamic restrictions 20

8 Hydrothermal deactivation 23

8.1 Catalyst characterization 23

8.1.1 Ammonia storage capacity 23

8.1.2 Oxidation state of iron 23

8.1.3 NO storage capacity 25

8.2 Catalytic activity 25

8.2.1 NO and NH_3 oxidation 25

8.2.2 NH_3-SCR 26

8.2.3 Ammonia inhibition 27

8.3 DRIFT spectroscopy 27

8.4 H_2 - pretreatment 29
9 Chemical deactivation 31
9.1 Phosphorous exposure 31
9.1.1 Ammonia storage capacity 31
9.1.2 X-ray photoelectron spectroscopy and NO adsorption 31
9.1.3 NO and NH_3 oxidation 31
9.1.4 NH_3-SCR and ammonia inhibition 32
9.2 Potassium exposure 33
9.2.1 Ammonia storage capacity 33
9.2.2 NO_X adsorption 33
9.2.3 NH_3-SCR and ammonia inhibition 34
9.2.4 X-ray photoelectron spectroscopy 35
9.3 Summary of the deactivation and regeneration mechanism 36
10 Kinetic deactivation model 39
10.1 Reaction rates 39
10.1.1 NH_3 and NO adsorption and desorption (subsystem 1) 39
10.1.2 NH_3 and NO oxidation (subsystem 2) 40
10.1.3 NH_3-SCR 40
10.2 Results 41
10.2.1 NH_3 and NO storage and oxidation 41
10.2.2 NH_3-SCR 42
10.2.3 Ammonia inhibition 44
10.3 Comparison and validation to chemically deactivated Fe-BEA 47
11 Low-temperature solid-state ion-exchange of copper 49
12 Ammonia formation in NO_X storage and reduction catalysts 51
13 Concluding discussion 53
Acknowledgments 55
Nomenclature 57
References 59

1 Introduction

Currently, there are considerable discussions on the impact of emissions from combustion of fossil fuels on the human health and the global climate, where one of the major contributors to air borne emissions is the transport sector. The air pollutions are negative for our health and the environment but are also suspected to cause global climate changes [1].

The necessity to control vehicle emissions began in the 1970s in the United States. The federal government established air pollution regulations for key-pollutants with the Clean Air Acts of 1970, 1977, and 1990 [1], which were passed by the U.S. Congress. The Congress also established air quality standards in the U.S. for six outdoor pollutants; carbon monoxide (CO), nitrogen oxides (NO_X), sulfur dioxide (SO_2), suspended particulate matter (PM), volatile organic compounds (VOC or HC), ozone (O_3), and lead (Pb) [1].

The products formed during the burning process in internal combustion engines are major contributors to global air pollution, where CO, HC and NO_X are the major components of the exhaust gases. With more stringent environmental legislations of NO_X emissions, there is a need for more active and durable emission control systems [2]. The technologies to reduce NO_X emissions falls into two general categories: *Primary control technologies*, that are used to minimize the amount of NO_X initially produced in the combustion zone and *Secondary control technologies*, which are used to reduce the NO_X present in the exhaust gas from the combustion zone, in a so called aftertreatment system.

For mobile applications several secondary control technologies have been developed in order to remove NO_X from exhaust gases. Nowadays, the three-way catalyst (TWC) is used worldwide in vehicles with engines operating under stoichiometric conditions (air-to-fuel mass ratio, 14.6), such as conventional gasoline engines [3, 4]. However, economic and environmental concerns have led to increased demands of increased fuel economy for vehicles. To be able to improve the fuel economy (decrease the fuel consumption), engines need to be operated under lean conditions, meaning with oxygen excess during the combustion process [2], which gives more complete combustion and higher fuel efficiency compared to stoichiometric combustion. However, under lean conditions the TWC cannot efficiently reduce NO_X since CO and HC, which otherwise act as reducing agents for NO_X, are oxidized by the excess oxygen [5].

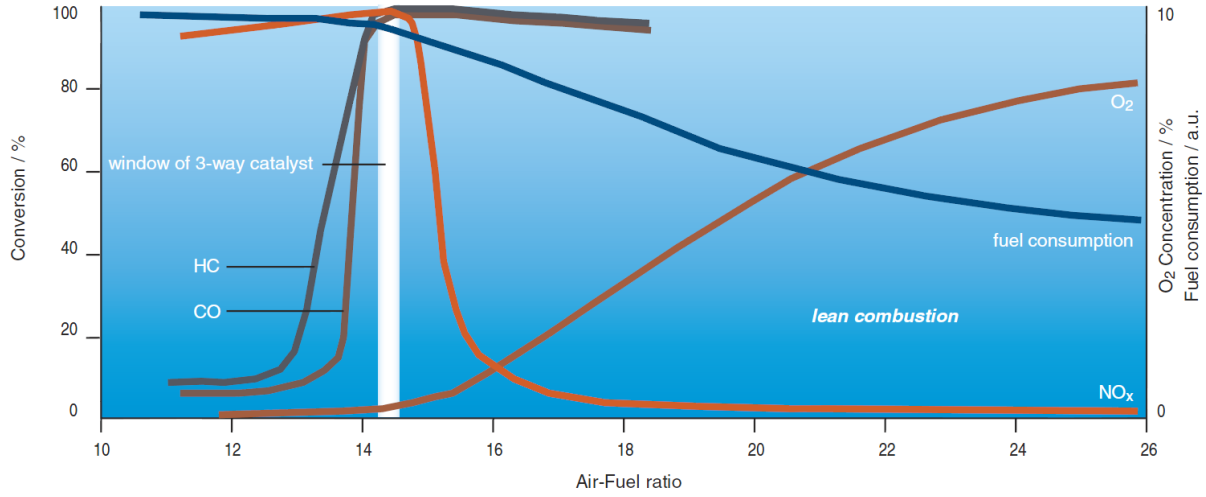

Figure 1.1. *Fuel consumption and TWC catalyst performance of a gasoline engine as a function of air-to-fuel ratio. Figure adapted from ref. [6].*

The use of engines running under lean conditions has resulted in the need for new catalysts, which selectively can reduce NO_X in oxygen excess. One solution for this is the use of NO_x storage and reduction (NSR) catalysts. In this concept the catalyst is subjected to mixed lean operation, with relatively long lean periods followed by short rich pulses. During the lean periods NO_x is stored in the catalyst and during the short rich pulses the stored NO_x is released and reduced, and thereby the storage component is regenerated. However, the process has disadvantages such as high demand of engine control as well as high fuel consumption when running the engine under rich conditions.

Another well-established and effective method to eliminate nitrogen oxides under oxygen excess is selective catalytic reduction of NO_X using ammonia as reducing agent (NH_3-SCR) according to the stoichiometry [7]:

$$4\ NH_3 + 4\ NO + O_2 \rightarrow 4\ N_2 + 6\ H_2O \qquad (1.1)$$

Vanadia-based catalysts were initially used for SCR applications. However, problems including catalyst ageing and also the toxicity of vanadia, which may form volatile compounds at high temperatures, have promoted the development of alternative catalysts, especially for mobile applications. Metal-ion exchanged zeolites have in this connection proven to be very active and promising alternatives to vanadia as SCR catalysts [7-9], where copper [10-15] and iron [7, 11, 16-19] presently are the most common metals.

Several challenges arise when using these materials in exhaust gas aftertreatment systems for diesel and lean burn vehicles. Two of the more important issues are the tolerance against chemical poisoning and the hydrothermal stability of the ion-exchanged zeolites [7].

Chemical poisoning is strong chemisorption of impurities on the active sites of the catalyst [20], where good tolerance against poisons such as calcium (Ca), potassium (K), magnesium (Mg), phosphorous (P), sulphur (S), and zinc (Zn), which originate from fuel, lubricating oils, impurities of (bio-)diesel fuel and urea solution is needed [21, 22]. Furthermore, severe chemical deactivation can result in physical deposition of species onto the surface, blocking the active sites of the catalyst. Another problem is pore blockage caused by hydrocarbons [23-25], especially during cold-start conditions. However, the resistance of metal-exchanged zeolites towards hydrocarbon poisoning can be enhanced by addition of a protection layer over the zeolite [23].

Hydrothermal deactivation is a known problem mainly due to the high temperatures needed during regeneration of the particulate filter, which is placed upfront of the SCR catalyst in the exhaust aftertreatment system. Different mechanisms have been proposed for the deactivation caused by hydrothermal treatment. According to Bartholomew et al. [20], the deactivation mechanisms due to hydrothermal treatment are not completely understood where it is suggested that the deactivation proceeds via two major mechanisms; (i) loss of catalytic surface area due to pore collapse of crystallites of the active phase, and (ii) loss of support area due to support collapse and crystallite growth.

Bartholomew et al. [20] have pointed out the need for more fundamental understanding of different deactivation mechanism of catalysts which can provide the fundamental basis for development of deactivation models. Improving the understanding of deactivation is of great interest to be used in designing new catalyst formulations and optimizing the operation conditions for catalytic processes. For mobile applications, like NH_3-SCR, catalyst deactivation is a practical concern in terms of sizing the catalyst for the lifetime of the vehicle and accounting for the performance loss over time for the SCR catalyst.

2 Objective

Catalyst deactivation is a significant and inevitable problem in many important applications. The deactivation causes negative economic as well as environmental effects and there is a considerable motivation to understand the mechanisms for catalyst decay in order to design stable catalysts and catalytic processes.

The objective of this thesis is to study activity and deactivation of metal-exchanged zeolites for NH_3-SCR applications with special focus on understanding the fundamental deactivation mechanisms for this type of catalyst with attention paid on the active species.

The project is divided in four parts where the first part is an experimental study of hydrothermal and chemical deactivation, and regeneration of Fe-BEA as NH_3-SCR catalyst **(Paper I-VII)**. The objective is to study deactivation with focus on the active iron species in the catalyst. This is performed by using multiple characterization techniques in combination with studies of the catalytic performance of Fe-BEA. In **Paper I-III**, hydrothermal deactivation is studied by correlating changes of the physiochemical properties of the catalyst with the catalytic activity with respect to NO- and NH_3-oxidation, NH_3-SCR and inhibition of the SCR reaction due to high surface coverage of ammonia. DRIFT analysis is used to further study the evolution of the different iron species in the catalyst after thermal treatment. In **Paper IV and V**, the possibility to regenerate the catalyst using hydrogen after hydrothermal treatment is investigated with focus on the active iron sites. Furthermore, chemical deactivation of the catalyst due to phosphorous and potassium exposure is studied in **Paper VI and VII**.

In the second part, presented in **Paper VIII-X**, a multi-site kinetic model is developed to simulate and predict deactivation of Fe-BEA as NH_3-SCR catalyst. The model is based on the experimental results from the studies of hydrothermal deactivation with focus on the active iron sites and validated using the results from the chemical deactivation studies. In **Paper XI** the results from part one and two are summarized and discussed with focus on future catalytic deactivation models.

In the third part, **Paper XII**, low-temperature solid-state ion-exchange of copper into different zeolites is studied for preparation of active copper-exchanged NH_3-SCR catalysts.

Finally, in the fourth and final part, in **Paper XIII**, ammonia formation in NO_X storage and reduction catalysts is studied for the possibility of combining NSR and SCR catalysts.

3 Catalysis

In the beginning of the 19th century, Berzelius introduced the terms catalysis and catalyst, even though catalysis was used in many industrial processes [26]. Catalysis is the phenomenon in which a relatively small amount of a foreign material, called a catalyst, increases the rate of a chemical reaction without itself being consumed. Other pioneers active early in this field during the 19th century include Berthelot, Davy, Faraday, Ostwald and Sabatier. In the beginning of the 20th century tremendous advances in catalytic processing were made as ammonia synthesis from N_2 and H_2, ammonia oxidation to nitric acid, the synthesis of hydrocarbons and organics from H_2 and CO, and hydrogenation of oils and fats were developed. After Langmuir's contribution between 1915 and 1920 to the field of catalysis, which provided a relationship between adsorbed species and measurable experimental parameters, modeling of quantitative kinetics of reactions occurring on catalytic surfaces begun. Catalysts can enable reactions that would otherwise be blocked or significantly slowed by kinetic barriers. The catalyst may increase the reaction rate or selectivity, or enable the reaction to proceed at lower temperatures [26]. This effect can be illustrated with a Boltzmann and energy profile diagram, see Figure 3.1.

However, catalysts do **not** change the extent of a reaction; i.e. the catalyst has **no** effect on the chemical equilibrium of a reaction because the rate of the forward and the reverse reaction are both affected. Due to the complexity of catalytic processes, catalysis is an interdisciplinary field, combining knowledge from chemistry, physics, mathematics, chemical engineering and materials science [26]. Catalysts come in multitudes of forms from atoms to larger structures, which can be employed in various surroundings from liquids, gases and surfaces of solids. In general the subject catalysis is divided in three disciplines: homogeneous, heterogeneous and bio-catalysis [27].

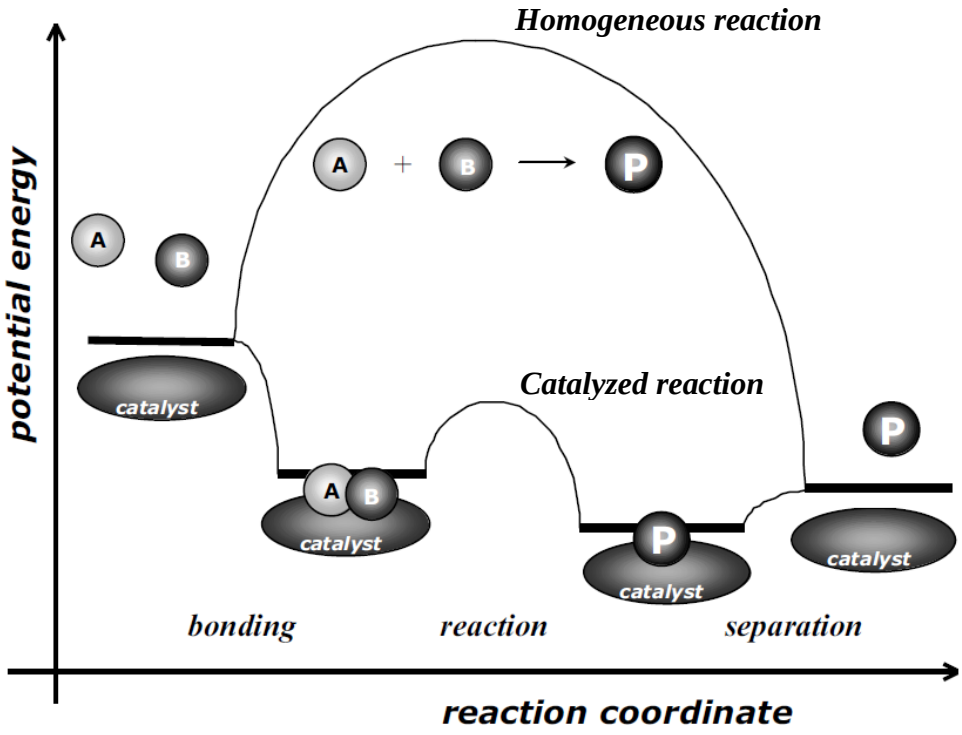

Figure 3.1. *The presence of the catalyst opens a different reaction pathway with lower activation energy compared to the homogeneous reaction. Figure adapted from ref. [27].*

In homogeneous catalysis both the catalyst and the reactants are in the same phase, i.e. gas phase or liquid phase. For example, decomposition of ozone in the atmosphere is a common example of homogenous catalysis, where ozone decomposes to oxygen via a reaction with chlorine atoms, which acts as catalyst.

Enzymes are the nature's example of catalysis, biocatalysts. Enzymes allow biological reactions to occur at a specific rate necessary for the specific bio-reaction, where one common example is the breakdown of alcohol to acetaldehyde inside the body by the specific enzymes.

In heterogeneous catalysis the catalyst and the reactants are in different phases, e.g. solid materials which catalyze reactions of molecules in gas or liquid phase. Heterogeneous catalysts are the most common catalyst used in the chemical and petrochemical industry. Another example of the applications of heterogeneous catalysis is cleaning automotive exhausts. The major air pollutants from gasoline vehicles like NO_X, CO and HC need to be removed or converted to harmless compounds. This is performed by a catalytic converter, se Figure 3.2. To maintain a conversion at a high level, catalysts with complex structures are needed, involving many different parts. The core or substrate is often a ceramic honeycomb in modern catalytic converters, but stainless steel is also used. The role of the honeycomb structure is to increase the surface area available to support the catalyst, and is therefore often called a "catalyst support". The substrate is in turn coated with a washcoat which forms a rough, irregular surface which has a far higher surface area than the flat substrate, which increases the total surface area available for the active phase significantly.

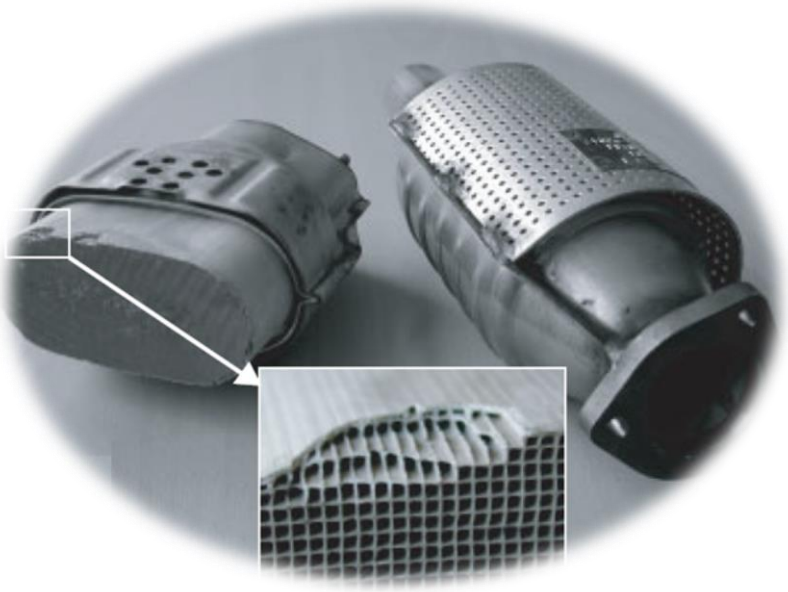

Figure 3.2. *A typical catalytic exhaust converter for automotives. Figure adapted from ref. [27].*

4 NH_3-SCR

Selective catalytic reduction of NO_X with ammonia is since the 70's a well-established and effective method to eliminate nitrogen oxides under oxygen excess for stationary applications as a *secondary control technology* [28]. It is relative straight forward today to develop aftertreatment processes for stationary sources, where the NO_X emissions can be reduced by up to 96% with a standard SCR system [28]. Stationary sources usually operate at constant load, relatively high temperatures and restrictions according to size are usually limited, and hence installing an SCR system which is optimized for efficient NO_X reduction is attractive. However, using NH_3-SCR technology for mobile vehicle applications is not a trivial task. The engine operates at different loadings which results in a varying temperature and flow rate of the exhaust gases over time. This makes the implementation of the NH_3-SCR system a challenging task. Furthermore, due to limited space for mobile applications the running conditions for the SCR system needs to be optimized. Additionally, the implementation of an NH_3-SCR system includes other requirements, like a well-distributed infrastructure for urea (decomposes into ammonia used as the reducing agent) and a well-functioning urea injection to avoid ammonia slip. Figure 4.1 shows the fraction of NO_X as function of temperature from a Euro IV engine during a NEDC-cycle (New European driving cycle). It can be observed how the NO_X distribution varies with temperature compared to a stationary source which has a relative stable outlet temperature; hence it is very important for a mobile NH_3-SCR catalyst to be active over a wide temperature range to effectively reduce the outlet NO_X.

Since ammonia is gaseous and toxic under normal pressure and temperature, other ammonia containing sources than ammonia are required for mobile SCR applications. Held et al. [29] published one of the first investigations where it was suggested to use non-toxic urea that decomposes to ammonia as the ammonia source for SCR. Today, urea-water solutions are used as an onboard source of ammonia for mobile applications where ammonia is formed from urea by thermal decomposition and hydrolysis [30, 31]. Ideally, this process would result in two moles of ammonia released per mole of injected urea. The decomposition and hydrolysis of urea in presence of water proceed according to:

$$NH_2 - CO - NH_2 \xrightarrow{\Delta T} NH_3 + HNCO \quad (4.1)$$

$$HNCO + H_2O \rightarrow NH_3 + CO_2 \quad (4.2)$$

However, in the following discussions of this thesis, ammonia (NH_3) will be referred to as reducing agent instead of urea, although all coming statements about NH_3-SCR also can be applied to urea-SCR [7].

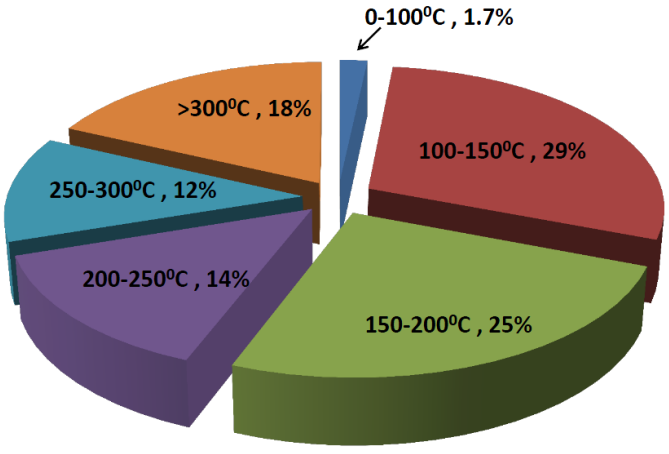

Figure 4.1. *Typical engine out NO_X temperature distribution from a diesel engine. Figure adapted from Haldor Topsøe A/S.*

4.1 SCR chemistry

The exhaust gases from diesel engines contain many species, where the nitrogen oxides mainly are composed of NO. Only a minor fraction is nitrogen dioxide (NO_2) [30]. Under those conditions, reduction of NO with ammonia is the main SCR reaction, and is usually referred to as the "standard SCR reaction" [30, 32-37]:

$$4\,NH_3 + 4\,NO + O_2 \rightarrow 4\,N_2 + 6\,H_2O \quad (4.3)$$

However, the reaction between NO, NO_2 and NH_3 is much faster if the ratio between NO and NO_2 is equal. Under those conditions, the so-called "fast SCR reaction" occurs [30, 32, 33, 35, 37-39]:

$$2\,NH_3 + NO + NO_2 \rightarrow 2\,N_2 + 3\,H_2O \quad (4.4)$$

The fast SCR reaction is important for diesel aftertreatment systems to reach a high NO_X conversion and therefore an oxidation catalyst, usually called diesel oxidation catalyst (DOC), is used in the system to oxidize NO to NO_2 (c.f. eq. 4.6). Furthermore, there is a third SCR reaction that occurs if the NO:NO_2 ratio is below 0.5 where NH_3-SCR with only NO_2 takes place [30, 33, 34]:

$$4\,NH_3 + 3\,NO_2 \rightarrow 3.5\,N_2 + 6\,H_2O \quad (4.5)$$

There are also several side reactions that occur and compete with the previous reactions during SCR conditions. At higher temperatures oxidation reactions can occur. NO and NH_3 oxidation are two major reactions that may appear [7]. Oxidation of NO to NO_2 is considered to be the rate determining step in NH_3-SCR, to improve the fast SCR reaction step (eq. 4.4) [11, 32]:

$$NO + \frac{1}{2}\,O_2 \leftrightarrow NO_2 \quad (4.6)$$

However, NH_3 oxidation is not a desirable reaction, thus less NH_3 will be available for NH_3-SCR and at higher temperatures the oxidation of ammonia becomes more pronounced. Ammonia can be oxidized to NO or N_2 according to [33, 40-42]:

$$4\,NH_3 + 5\,O_2 \rightarrow 4\,NO + 6\,H_2O \quad (4.7)$$

$$4\,NH_3 + 3\,O_2 \rightarrow 2\,N_2 + 6\,H_2O \quad (4.8)$$

Further reactions, e.g. the formation of N_2O have been observed for metal exchanged zeolites under NH_3-SCR conditions according to eq. 4.9-11. However, for Fe-exchanged zeolites reaction (4.9) and (4.10) have not been observed [18, 32, 43, 44].

$$2\,NH_3 + 2\,O_2 \rightarrow N_2O + 3\,H_2O \quad (4.9)$$

$$4\,NH_3 + 4\,NO + 3\,O_2 \rightarrow 4\,N_2O + 6\,H_2O \quad (4.10)$$

$$4\,NH_3 + 4\,NO_2 + O_2 \rightarrow 4\,N_2O + 6\,H_2O \quad (4.11)$$

The formed N_2O can be reduced to nitrogen by ammonia over metal-exchanged zeolites, thus N_2O appears only at low temperatures [7, 10, 32, 45-48].

Reactions 4.3, 4.6 and 4.8 are the main reactions studied and evaluated in the present thesis. However, the NH_3-SCR mechanism over metal-exchanged zeolite catalysts is more complex and contains multiple reactions steps. Brandenberger et al. [7] have summarized the SCR reaction process over iron-exchanged zeolites according to the scheme in Figure 4.2.

4.2 SCR catalysts

Vanadia supported on titania [7, 49-52] was the first ammonia SCR catalyst that was commercialized for mobile applications. The catalyst is active around 350-450^{0}C. However, at lower or higher temperatures the NO_X reduction decreases, especially at higher temperatures where the selectivity decreases due to enhanced oxidation of ammonia [53]. Nevertheless, problems like deactivation, toxicity of volatile vanadia and the high oxidation rate of SO_2 to SO_3, have promoted the development of alternative catalysts like metal-exchanged zeolites. Metals such as copper [10-15] and iron [7, 11, 16-19] are the most common metals used. Copper-based zeolites are usually more active in the low-temperature (<300^{o}C) range while iron-based zeolites are more active at higher temperatures (>300^{o}C) during steady-state conditions when reaction 4.3 is dominating. However, for mobile applications where an oxidation catalyst usually is placed upstream to the SCR catalyst, reaction 4.4 dominates where the ratio between NO and NO_2 is equal, iron-based zeolites have shown higher activity than copper-based zeolites [54]. However, in real-world performance where steady-state conditions are rarely reached when used for mobile applications, Kamasamudram et al. [55] have shown that during transient conditions (where concentration of the reactants constantly varies) iron-exchanged zeolites achieve an overall higher NO_X conversion than copper-exchanged zeolites. Additionally, iron-exchanged zeolites have shown relatively good resistance against sulfur poisoning as compared to copper-exchanged zeolites [35].

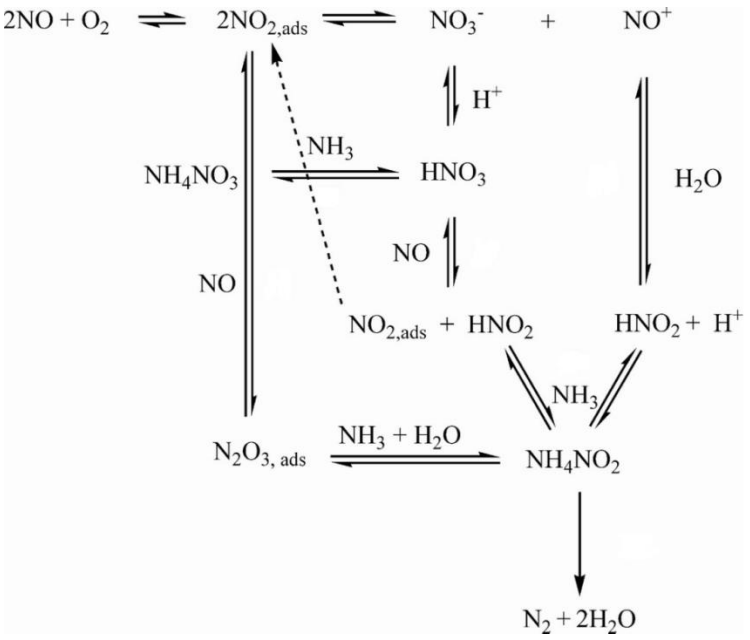

Figure 4.2. *NH_3-SCR reaction process over iron-exchanged zeolites according to Brandenberger et al. Figure adapted from ref. [7].*

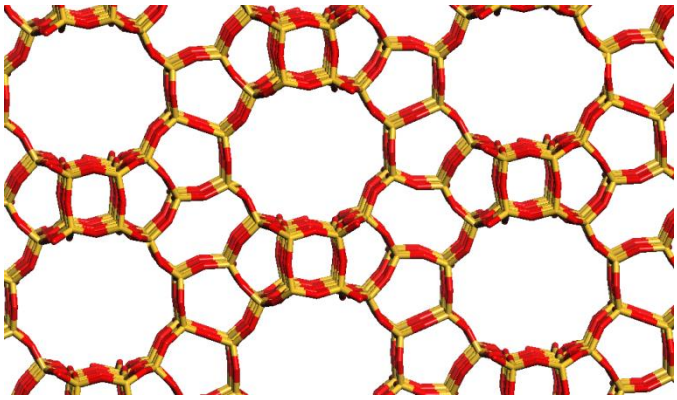

Figure 4.3. *Framework structure of zeolite BEA, where red spheres represent oxygen, yellow spheres silicon or aluminum.*

4.2.1 Metal-exchanged zeolites

In 1756 Axel Fredrik Cronstedt, a Swedish mineralogist, was the first person to the term zeolite [56, 57]. Zeolites have a well-defined porous structure and can easily adsorb liquids. Large amounts of steam are produced when heating the found material, thus named zeolite, from the Greek "*zeo*" (to boil) and "*lithos*" (stone), the boiling stone [57]. Zeolites are also referred to as "molecular sieves" due to the ability to sort out molecules based on their size, controlled by the dimensions of the zeolite pores. There are several types of zeolites used for SCR applications, where zeolites with *BEA, MFI and CHA structure are the most common ones. The first two framework structures have large and medium pore sizes containing 12 (*BEA) and 10 (MFI) O-atoms in the window opening, respectively. Small pore zeolites with CHA structure have a smaller window size with 8 O-atoms [58]. Figure 4.3 shows an example of a silicon based zeolite with *BEA framework structure doped with aluminum. The BEA zeolite can be synthesized in a wide range of SiO_2/Al_2O_3 ratios. Due to that aluminum has one unit charge lower than silicon the negative charges are balanced by framework cations such as protons or other positive ions [59]. The zeolites can be ion-exchanged with transition metal ions by several methods. As mentioned previously, copper and iron are the most used transition metals in metal based zeolites for NH_3-SCR applications.

There are several methods to introduce the active copper species into zeolites. The most conventional method is by exchange with Cu^{2+} ions in aqueous solutions. An alternative method is to introduce the metal-ions into the zeolite by solid-state ion-exchange in absence of a solution. [7]. However, there are several drawbacks with these methods. Using an aqueous solution, the exchange procedure has to be repeated several times to obtain a high exchange level. Furthermore, using zeolites with relatively small pore sizes, limits the applicability of solution based ion-exchange procedures. Solid-state ion-exchange requires a relatively high temperature which restricts the method to thermally stable zeolites only. In **Paper XII**, this issue has been addressed for copper-exchanged zeolites, where low-temperature solid-state ion exchange is investigated.

Similar to copper-exchanged zeolites, iron-exchanged zeolites can also be prepared by several methods. Aqueous solutions of different iron precursors like $FeCl_2$ [60-63] or $FeSO_4{\cdot}7H_2O$ [45, 64] can be used. Incipient wetness impregnation is also a common way to introduce metal ions into the zeolite framework. These methods results in different iron species, isolated Fe^{3+}, dimeric Fe^{2+} or smaller and larger Fe_xO_y clusters depending on the amount of iron exchanged into the zeolite. Brandenberger et al. [65] showed that a lower Fe/Al ratio than 0.15, mainly results in isolated iron Fe^{3+} species, while for higher ratios larger iron species are the dominating species (c.f. Figure 4.4).

4.3 Activity and deactivation

The active sites of copper- and iron-exchanged zeolites for NH_3-SCR are still debated in the literature and no general conclusion has been able to be drawn.

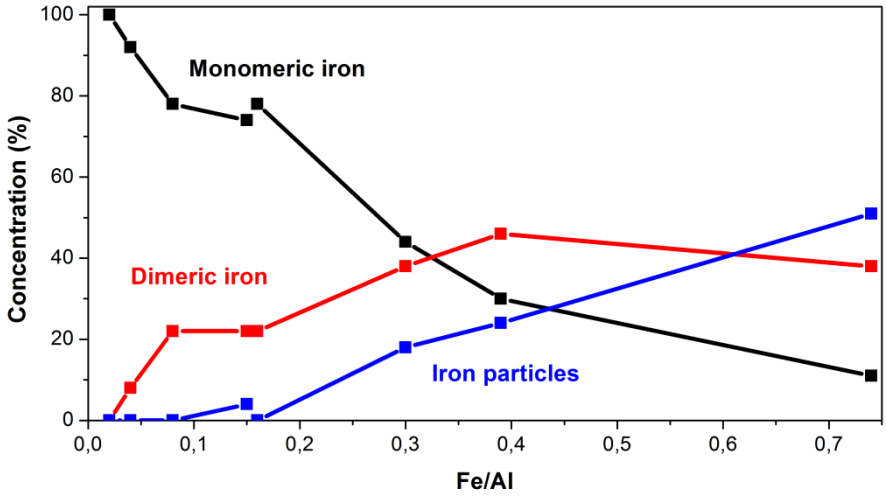

Figure 4.4. *Relative concentration of various iron species in Fe-ZSM-5 samples measured by UV-Vis spectroscopy. Adapted from ref. [65].*

For copper-exchanged zeolites it has been suggested that both Cu^{+} and Cu^{2+} species are active for NH_3-SCR as either monomers or dimers [66]. Kwak et al. [67] studied the catalytic activity as a function of copper exchange level and found that the first sites that are exchanged are the most active ones for NH_3-SCR. For ion-exchanged zeolites, several iron species have been proposed as active sites, which includes smaller iron species such as monomeric or dimeric iron and larger species such as Fe_xO_y clusters or particles. Grünert et al. [68, 69] concluded that isolated Fe species as well as bridged Fe species are active during NH_3-SCR. Furthermore, Brandenberger et al. investigated the active site for NH_3-SCR in Fe-ZSM-5 in terms of turnover frequencies (TOF) values and found that monomeric and dimeric iron species are the active sites for NH_3-SCR, which agrees well with the results by Grünert et al. Furthermore, it was found that the formation of different iron species could be correlated to the iron loading in the zeolite. The UV-Vis results from Brandenberger et al. [65] are shown in Figure 4.4 where the relative concentration of different iron species at different iron loadings are presented. Similar results were reported by Capek et al. [70] and Gutierrez et al. [71] concluding that it is not possible to prepare Fe-zeolites with exclusively isolated iron species for iron ratios above Fe/Al = 0.2. Lower iron loadings, i.e. Fe/Al < 0.1 will mostly result in the formation of isolated monomeric iron species (Fe-O-OH) because the iron ions will be located too far from each other to interact, while higher amounts will result in interaction between the iron ions forming binuclear oxygen bridged dimeric iron (OH-Fe-O-Fe-OH) species and iron particles (Fe_2O_3). The relative concentration of the different iron species was correlated with activity for NO_X reduction and NH_3 oxidation activity [65]. It was found that the SCR reaction primarily proceeds over monomeric iron species up to 300^0C. However, at higher temperatures >300^0C, dimeric iron species starts contributing to the SCR reaction and also larger iron species. Additionally, it was observed that dimeric iron species govern the NH_3 oxidation and the monomeric sites are relatively inactive up to 500^0C. Devadas et al. showed that Fe_2O_3 particles are not active in the SCR reaction but in the oxidation of NO [72]. It was observed that oxidation of NO to NO_2 over Fe^{3+} is favored by Fe_2O_3 particles in Fe-ZSM-5.

4.3.1 Hydrothermal deactivation

Due to the growing interest in iron-exchanged zeolites as SCR catalysts for mobile applications, the hydrothermal stability of the catalyst needs to be further investigated. The fraction produced NO_X from a diesel engine at various temperatures, presented in Figure 4.1, shows a wide temperature range, where about 18% of the NO_X is produced at temperatures above 300^0C. Previous studies of Fe-ZSM-5 have shown that this catalyst is thermally stable up to 500^0C in presence of water (hydrothermal

treatment). However, after hydrothermal treatment above 500^0C, deactivation is always observed [18, 56, 73-75]. Diesel engines are usually equipped with a diesel particulate filter (DPF), which is placed upstream of the SCR catalyst. The DPF is installed to meet the soot particle emission standards and needs to be regenerated regularly to be able to meet the legislation requirements. The DPF is regenerated by heating to high temperatures around 600-700^0C whereby the carbon in particulates is oxidized which directly affect the temperature of the gases out from the DPF and into the SCR catalyst [76]. Regeneration of the DPF at high temperatures may damage the SCR catalyst resulting in decreased efficiency to reduce NO_X. With time, the catalyst becomes less active and is not able to reduce the incoming NO_X effectively, hence the temperature of the SCR catalyst needs to be increased to be able to reduce the NO_X and fulfill the emission standards. The produced NO_X can further be controlled by the engine, *primary control technology* (cf. introduction), by increasing the amount of fuel, meaning decreasing the air-to-fuel ratio (c.f. Figure 1.1). However, this way of reducing NO_X results in increased fuel consumption which is not sustainable and therefore the need of understanding and preventing the deactivation processes of the SCR catalyst are becoming more important.

Brandenberger et al. proposed a deactivation mechanism which agrees well with the general mechanism of thermal deactivation suggested by Bartholomew [20] (cf. introduction), for the hydrothermal deactivation of Fe-ZSM-5. The deactivation is dominated by three parallel processes: (i) rapid dealumination of Brønsted sites (i.e. Al-OH-Si), (ii) depletion of dimeric iron species, and (iii) migration of isolated iron ions followed by dealumination [74]. The hydrothermal stability of Fe-BEA has been further studied in **Papers I-V**.

4.3.2 Chemical poisoning

Today 95% of the world's transportation fuel originates from fossil sources [21]. However, as the production of biodiesel grows, chemical deactivation (poisoning) is becoming more relevant. In order to reduce the dependency on fossil fuels and to control climate changes the need of renewable energy carriers is growing [77, 78] and therefore the use of biodiesel and other fuels from biomass is rapidly increasing. Due to chemical impurities originating from (bio-)diesel fuel, lubricating oils and urea solutions, high tolerance against catalyst poisons is desired [21], where poisons such as phosphorous and potassium are two of the more important catalyst poisons along many others [21, 22]. Lubricating oils are normally the major source of phosphorous, while potassium mainly originates from biofuels. The need of deeper research in the area of phosphorus and potassium poisoning is therefore essential in order to meet future emission limits.

In this context, chemical poisoning is referred to as strong chemisorption of reactants, products or impurities on sites otherwise active for the desired reaction [20]. One example of the former is strong adsorption of one reactant that hinders adsorption of the other reactant i.e. self-poisoning. Catalyst poisons can also be categorized into non-selective or selective poisons, depending on whether the poisoning takes place over the entire catalyst surface or only on certain sites.

Presently, there are not many studies on phosphorous or potassium poisoning of zeolite-containing catalysts. Most studies of chemical deactivation of NH_3-SCR catalysts are carried out by wet-impregnating the samples with one or multiple impurities. Castellino et al. [79] showed that for NH_3-SCR catalysts exposed to flue gases doped with impurities the deactivation is more severe compared to wet-impregnation of the samples by impurities which most likely results in both physical and chemical deactivation of the catalyst.

The understanding of individual and combined effects of poisons as well as the influence of simultaneous poisoning and thermal deactivation is not understood and further fundamental studies on poisoning are thus needed. Especially, systematic studies focusing on chemical deactivation of the catalytic sites, using relatively low amounts of chemical poisons. Chemical deactivation of Fe-BEA due to phosphorous and potassium exposure has been further studied in **Papers VI-VII**.

5 NO_X storage and reduction

NO_X storage and reduction is another possible and promising solution for NO_X reduction for lean burn engines next to NH_3-SCR. This method is based on mixed lean operation, where the NO_X is stored under the lean phase for about 60-90 seconds followed by the NO_X regeneration period where the engine operates in a rich mode (oxygen deficient) for a short period of time (3-5 seconds) in which NO_X is released from the storage sites and reduced with hydrocarbons, CO and H_2.

NSR catalysts are relatively complex systems. The NSR catalyst contains three essential parts, a support material with high surface area, a storage component and noble metals. Below, a short discussion will follow about the choice of the compounds and reaction mechanisms [80-84].

5.1 Materials

Support materials. The main purpose of the support material is to provide a high surface area to carry the storage component and the noble metals. Durability is another important role for the support, for example thermal resistance. The most common support material is γ-Al_2O_3, which has a surface area of 100-200 m^2/g and is thermally stabile up to 850^{o}C before it starts sintering and hence temperatures above 850^{o}C should be avoided for these types of catalysts. Besides acting as a support, alumina has the ability to actively take part in the NSR process, due to its capacity to store NO_X at lower temperatures.

Storage components. The choice of storage component is thoroughly described in the literature. Takahashi et al. [85] and Kobayashi et al. [86] concluded that the more alkaline the element is, the higher the NO_X storage capacity is. Their studies showed that the NO_X storage performance at 350^{o}C decreased in the following order: K > Ba >Sr> Na >Ca> Li > Mg. However, the disadvantage with a strong alkaline catalyst is that the conversion of hydrocarbons is also reduced. Today, barium oxide (BaO) is the most used storage material for NSR catalysts.

Noble metals. Kobayashi et al. [86] studied the choice of the noble metals and ranked them in the following order, Pt/Rh >Pd/Rh> Pd. Additionally, in a comparative study by Salasc et al. [83] of Pt/BaO/Al_2O_3 and Pd/BaO/Al_2O_3 it was shown that the Pd based catalyst stored more NO_X at 300^{o}C while at 400^{o}C the Pt based catalyst showed higher storage capacity of NO_X. The noble metal plays several key roles in the NO_X storage and reduction reaction steps. In the lean period, hydrocarbons, carbon monoxide, and nitrogen oxides are oxidized over the noble metals and in the rich period the NO_X is reduced over the noble metals.

5.2 NO_X storage

One of the most significant steps in the NO_X storage process is oxidation of NO to NO_2. Nitrogen dioxide has shown to be more easily adsorbed on the storage material than NO. The kinetics for the NO oxidation has been investigated by Olsson et al. [87] where it was shown that the oxidation is kinetically limited at lower temperatures and thermodynamically limited at higher temperatures. Different species adsorbed over the barium oxides during the lean phase have been observed. Barium nitrites and barium nitrates have been identified, where nitrate formation dominates at higher temperatures while nitrite species are observed at lower temperatures. Several studies have shown that nitrites are formed in the beginning of the lean period. The nitrites are loosely bound and are oxidized to the more stable nitrates after continued exposure to NO and oxygen [88]. Formation of nitrites and nitrates on alumina has also been detected and it has been shown that alumina plays an important role as a storage site. Storage on alumina is high at temperatures between 100-300^{o}C [89]. Furthermore, Clayton et al. [90] have shown that the distance between Pt and Ba sites is important for effective NO_X

storage and proposed that the fastest NO_X storage over barium occurs at storage sites located close to Pt.

5.3 NO_X reduction

NO_X reduction is the mechanism where NO_X is converted from NO_X to N_2 using different reducing agents like H_2, CO, C_3H_6 and C_3H_8, where it has been concluded that H_2 is the most effective reductant. However, it has also been observed that CO is an effective reducing agent and under practical running conditions both CO and H_2 are available for NO_X reduction, but it has been shown that when they are both present the efficiency is lower compared to when H_2 is present alone. Hydrogen is present in the exhaust during rich engine operations and can also be catalytically produced by the water-gas-shift reaction of CO and H_2O according to:

$$CO + H_2O \leftrightarrow CO_2 + H_2 \quad (5.1)$$

When using H_2 as reducing agent the desired product is N_2, but other byproducts can be formed such as NH_3 and N_2O (from the formed NH_3). Reducing mechanisms have been proposed where the produced NH_3 may further react with the oxygen and the adsorbed NO_X species.

5.4 Combining NSR and NH_3-SCR

NH_3-SCR catalysts can achieve relatively high NO_X conversions, but require an onboard urea storage and delivery system, which is not optimal for light-duty vehicles. However, NSR catalysts have the potential for being applied for both light- and heavy-duty vehicles. During regeneration of the NSR catalyst, ammonia can be formed which is a toxic gas and emissions of ammonia are not desired. To decrease the ammonia slip from exhaust aftertreatment systems, combined NSR and SCR concepts have recently gained attention [91]. Ammonia produced in the NSR catalyst is captured by the NH_3-SCR catalyst which is placed downstream the NSR catalyst and thus the SCR catalyst will improve the overall NO_X reduction and simultaneously decrease the NH_3 slip from the aftertreatment system. The economical aspect of combining the two catalysts is also important, since a fraction of the expensive NSR catalyst can be replaced by a much cheaper SCR catalyst and the need of a urea system disappears. The formed ammonia during the rich phase is stored in the SCR catalyst. During the lean phase when NO_X is stored in the NSR catalyst, the previously (during the rich phase) stored NH_3 in the SCR catalyst reacts with NO_X that was not successfully stored in the NSR catalyst. However, to combine NSR and SCR catalysts, the spatial formation of NH_3 during the rich phase needs to be well understood. In **Paper XIII**, a kinetic model is developed with focus on the spatial formation of NH_3 in NSR catalysts.

6 Experimental methods

6.1 Sample preparation

For **Paper I** a 6 wt. % Fe-BEA model SCR catalyst with a SiO_2/Al_2O_3 molar ratio of 29 was used. The catalyst consists of a washcoated ceramic monolith (400 cpsi) with 21 wt. % active material (i.e. zeolite and iron).

The catalysts used in **Papers II-XI** were prepared using incipient wetness impregnation. 1 wt. % Fe-BEA catalysts were prepared using 9.9g H-BEA with a SiO_2/Al_2O_3 molar ratio of 38, obtained by Zeolyst International, which was first dried at 120^0C for 2h. 0.72 grams of Fe $(NO_3)_3 \cdot 9H_2O$ (Fisher Scientific) was measured to correspond to 0.1 grams of Fe and dissolved in 9.9 ml of distillated water. The Fe-BEA sample was finally calcined at 450^0C for 2h. Cordierite monolith substrates (400 cpsi, 21 mm in diameter and 20 mm in length) were used and washcoated with the prepared Fe-BEA catalyst. To facilitate the attachment of the catalyst to the cordierite substrate, the monoliths were first washcoated with a thin layer of alumina, using boehmite (Disperal D). The coated monoliths were finally calcined at 500^0C for 2h. Figure 5.1 shows a monolith washcoated with Fe-BEA. The same procedure was used when Fe-BEA with 0.5-4 wt. % of iron was prepared.

The Cu-zeolite catalysts in **Paper XII** were prepared by mixing dry powder of CuO or Cu_2O and zeolites with MFI, *BEA and CHA framework structure with Si/Al ratio between 12 and 15 by simple grinding with a total copper content of 12.5 wt. % in the final catalyst.

6.2 Hydrothermal treatment and chemical deactivation

The catalysts in **Paper I-XI** were hydrothermally or chemically deactivated (aged) in an ageing reactor. The rig consists of a gas-preheater, an oven where the samples are placed, mass flow controllers, and a temperature and gas flow regulating system. The gas flow through the oven during the hydrothermal ageing was 4000 ml/min and consisted of 5% H_2O, 6% O_2 and N_2 as inert gas. The samples were treated at 600^0C for 24-100 h and at 700^0C for 3-48 h.

Furthermore, the gas flow through the reactor during the phosphorous or potassium exposure was 4000 ml/min and consisted of 10 or 50 ppm H_3PO_4 or KNO_3, and 10 % H_2O, 6 % O_2 and N_2 as inert gas. Phosphorous or potassium was mixed with distilled water in the feed system of the ageing reactor and thereafter the diluted solution was introduced to the preheater separately via a controlled evaporator mixer system and mixed with inert gas, heated to 350^oC and fed to the ageing reactor.

The catalyst samples in **Paper III** were thermally aged in ambient air using an oven at 700^0C for 12, 24 and 48 h, and at 800 and 900^0C for 48 h.

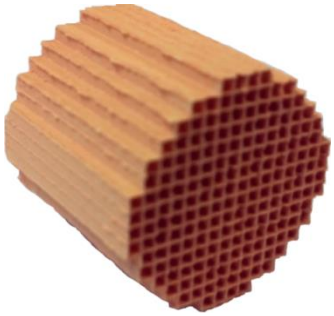

Figure 5.1. *A monolith substrate coated with Fe-BEA catalyst.*

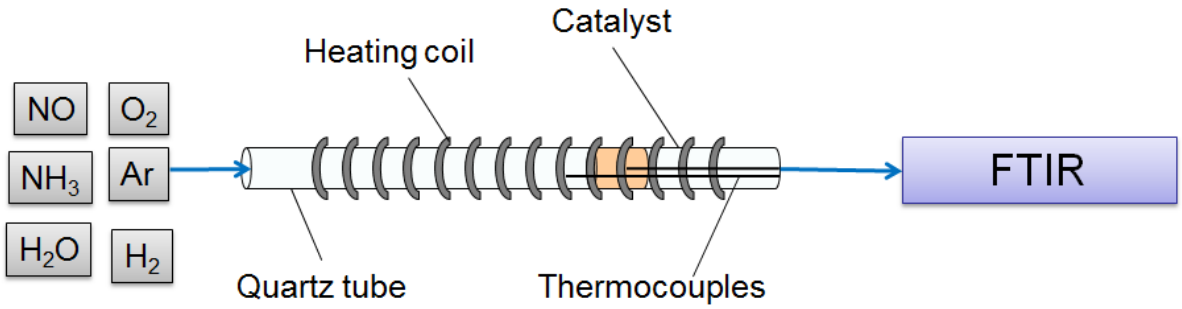

Figure 5.2. *Schematics of the flow reactor system. Mass flow controllers (gray) for each gas where the gas flow direction is shown with blue arrows. The outlet gas composition is analyzed with a Fourier transform infrared spectrometer (FTIR).*

6.3 Flow reactor system

The samples were characterized and evaluated with respect to catalytic performance in a continuous flow reactor system, described in Figure 5.2, in **Paper I-XI**. Briefly the reactor consists of a horizontal quartz tube equipped with a heating coil and insulation. The heating unit is controlled by a temperature controller (Eurotherm). The sample is placed in the quartz tube with a thermocouple placed about 10 mm in front of the catalyst to control the inlet gas temperature. A second thermocouple is placed inside the center of the sample to measure the sample temperature. The gas mixing system contains of separate mass flow controllers (Bronkhorst) for NO, NH_3, O_2 and Ar. Water is added downstream of the mixed gases in an evaporator which is heated to 150^{o}C. The amount of water added to the feed is controlled by a mass flow controller (Bronkhorst). Gas phase analysis is performed using a gas phase FTIR spectrometer (MKS 2000 FTIR). Furthermore, for the H_2-treatment experiments, hydrogen is added with a separate mass flow controller (Bronkhorst) for the hydrogen treatment. The total gas flow was kept constant at 3500 ml/min which corresponds to a space velocity (GHSV) of 27,600 h^{-1}. Prior to each flow reactor experiment the catalyst was oxidized using 8% O_2 at 500^{0}C to clean the surface.

The catalytic measurements in **Paper XII** were carried out in a fixed-bed quartz reactor (i.d. 2 mm) using 10 mg catalyst sample (150-300 µm fraction) and connected to a Gasmet CX4000 FTIR analyzer.

6.4 Sample characterization

The physiochemical properties of the samples were characterized by different methods; X-ray photoelectron spectroscopy (XPS), X-ray diffraction (XRD), Ultraviolet-visible spectroscopy (UV-Vis), nitrogen physisorption (BET), temperature programmed desorption (TPD) and scanning transmission electron microscopy (STEM).

X-ray photoelectron spectroscopy (XPS) is one of the most used techniques in catalysis to determine the elemental composition on the sample surface [92]. In this thesis XPS is used to determine the oxidation states of elements on the surface of the samples with focus on iron. X-ray photoelectron spectroscopy is based on the photoelectric effect. The sample is irradiated with a focused beam of X-rays whereby photoelectrons are emitted from the surface of the sample. The number and energy of the emitted electrons are measured. The number of emitted electrons depends on the energy and intensity of the X-ray beam. However, XPS is a very surface sensitive characterization technique. If the sample contains well dispersed particles the intensity will be high due to high coverage on the surface of the studied particle. Samples with larger particles, i.e. low dispersion will emit a relatively low intensity from the surface. Furthermore, as the emitted photoelectrons from the sample surface are easily absorbed by surrounding gas, the XPS measurements are performed at ultra-high vacuum (UHV) conditions, about 10^{-9} mbar, to minimize

loss of emitted photoelectrons. In this thesis the instrument used for the XPS measurments was a PerkinElmer PHI 5000C ESCA system using monochromatic Al Kα radiation and 45° take-off angle.

X-ray diffraction (XRD) is the most frequently used characterization technique to identify the crystalline phases that are present in the sample [92]. An advantage with XRD is that the technique can be used under realistic reaction conditions in specially designed in situ reactors. In this work, XRD is used to study the particle phase and size in the washcoat of the studied samples with focus on the zeolites and the exchanged metal. XRD is performed by focusing a beam of monochromatic X-ray photons onto the sample. The photons will scatter the incoming X-rays after interacting with atoms in a periodic lattice. The scattered X-rays that are in phase will give constructive interference and allow one to derive the lattice spacing. Furthermore, different crystal structures have individual angles of the crystal planes and by changing the incident angle of the X-rays, a diffraction pattern can be achieved, which gives information about the studied sample. The main instrument used in this thesis was a Siemens D500 X-ray diffractometer with Bragg-Brentano geometry and a Cu Kα source.

In-situ FTIR spectroscopy is the first modern spectroscopic technique to have a general acceptance in the field of catalysis [92]. Molecules or solid lattices vibrate when gaining energy due to absorption of photons or by scattering of photons, electrons or neutrons. Infrared spectroscopy is the most common form of vibrational spectroscopy and falls into three categories where the vibration frequency of molecules which lays in the range 200- 4000 cm^{-1} is the one used in this work. The type of bond and the masses of the atoms in the molecule are the properties which affect the energy difference between the vibrational states, where the vibrational frequencies increase with increasing bond strength and with decreasing mass of the vibrating atoms [92]. Molecules vibrate due to absorption of photons only if the dipole moment of the molecule changes during the vibration. Molecules without a changing dipole moment such as N_2 and O_2 cannot be detected using IR spectroscopy. By irradiating a sample with infra-red radiation one obtains a spectrum over the photons that are not absorbed by the sample as a function of photon energy, given as wavenumber or frequency.

Several forms of infrared spectroscopy are in use, where one of the most common techniques is diffuse reflectance infra-red Fourier transformed spectroscopy (DRIFTS), which is used to identify adsorbed species on the surface of a catalyst. Diffusely scattered radiation is collected by parabolic mirrors and makes it possible to qualitatively measure the vibrational modes of the adsorbed species on the surface. The technique is possible to perform in-situ which provides time-resolved information about changes in surface species caused by changes in reaction conditions.

Ultraviolet-visible spectroscopy (UV-Vis) is another technique to study metal species in a sample. UV-Vis is an absorption technique, measuring the reflectance or the absorption of the ultraviolet-visible beam focused on the sample. Molecules can absorb energy in form of ultraviolet or visible light to excite electrons to a higher anti-bonding molecular orbital. Different molecules absorb energy at different wavelengths, which results in a UV-Vis spectrum with varying intensities at different wavelengths depending on the nature of the sample. UV-Vis was used in this study to identify different iron species when varying the iron content in the prepared samples. The UV-Vis spectra were collected using a Cary 5000 UV-Vis-NIR spectrophotometer equipped with an External DRA-2500 unit. The spectra were recorded in the 200-1500 nm wavelength range. Furthermore, a Gaussina-Lorentzian function was fitted for the different iron types to compare the concentration of species.

Nitrogen physisorption is used to determine the specific surface area of a material [93]. The sample is cooled using liquid nitrogen (87 K) and exposed to gaseous nitrogen at increasing relative pressures, p/p0, where p is the equilibrium pressure and p0 is the saturation pressure. The gas molecules weakly adsorb (i.e. physisorb) on the sample surface with increasing pressure. The amount of adsorbed nitrogen can be calculated with the ideal gas law. By this method the total surface area or

specific surface area of a sample can be calculated, using the so-called BET (Brunauer-Emmett-Teller) equation, from the amount of nitrogen adsorbed. BET is used in this thesis to measure the change in specific surface area for the different samples.

Temperature programmed desorption (TPD) or thermal desorption spectroscopy (TDS) can be used to examine the desorption of gases from a material. TPD offers interesting opportunities to interpret desorption in terms of desorption kinetics [27, 92]. In this thesis TPD of NH_3, NO and NO_2 was performed in the flow reactor to study the adsorption strength and the number of available sites for adsorption of the molecules to the surface of the catalyst.

Transmission electron microscopy (TEM)

Electron microscopy is a technique to study size and shapes where relatively high resolution images are produced. Transmission electron microscopy (TEM) is similar to an optical microscope. However, the optical lenses are replaced by electromagnetic lenses. In a TEM an electron beam with high energy and intensity is created and passed through a condenser before it hits the sample. The condenser produces parallel rays (as in an optical microscope) which are focused on the sample. The electron transmitted through the sample is a projection of the samples mass which is magnified by the electron optics to produce a so-called bright field image. Electrons from the diffracted electron beams are used to form a so-called dark field image. Scanning transmission electron microscopy (STEM) is based on the principle of TEM, however, by scanning a focused beam of electrons across the sample in a raster pattern a virtual image is build. Furthermore, the STEM technique is also suitable for analysis techniques, e.g. energy dispersive X-ray spectroscopy (EDS).

6.5 Activity measurements

The catalytic activity for all samples was measured in the flow reactor to correlate changes in activity with structural changes of the metal-exchanged zeolites in **Paper I-XI**. NO and NH_3 oxidation experiments were performed exposing the samples to 400 ppm NO or NH_3, 8% O_2 and 5% H_2O whereby the temperature was stepwise increased from 150 to 500^{o}C (150, 200, 250, 300, 400 and 500^{o}C). The duration was 40 min for the first step, 30 min for step two and three, and 20 min for the last three steps. The heating rate between each temperature step was 20^{o}C/min, and the temperature did not exceed the set point more than 5^{o}C before stabilized at each step. Furthermore, the activity for selective catalytic reduction of NO_X with ammonia was studied for all samples. The feed gas consisted of 400 ppm NO, 400 ppm NH_3, 8% O_2 and 5% H_2O. The samples were exposed to the gas mixture at 150^{o}C for 40 min, 200, 250, and 300^{o}C for 30 min, and 400 and 500^{o}C for 20 min. The heating ramp between each step was the same as for the oxidation experiments. In **Paper XII**, the activity measurements were carried out in a fixed-bed quartz reactor using 500 ppm NO, 530 ppm NH_3, 10 % O_2 and 5 % H_2O balanced with N_2.

7 Theory and modeling

Different methods can be used to model catalysts and catalytic reactions. The most common methods for modeling are:

1. Density functional theory (DFT)
2. Monte Carlo simulations
3. Kinetic simulations (micro kinetics and global kinetics)
4. Computational fluid dynamics (CFD)

Kinetic simulations describe the rate at which reactions occur and make it possible to create a system of multiple reactions that give new fundamental understanding of the system studied. A good kinetic model may increase the understanding of the processes being studied for future catalyst development and design of catalytic processes. In this work a kinetic model is created to simulate the different activity measurements and TPD experiments for all samples in order to provide new understanding of the fundamental deactivation mechanisms for Fe-BEA as NH_3-SCR catalyst. The kinetic model is based on a mean field approximation, assuming that all adsorbed species are distributed randomly over the catalyst surface and there are no interactions (i.e. attractive or repulsive interactions) between the adsorbed species [27]. However, this assumption is seldom fulfilled. When the coverage of the adsorbed species is low the mean-field approximation usually works well. However, if the coverage of adsorbed species on the surface is high the mean-field approximation is not as good as for low surface coverage. The effect of high surface coverage can be adjusted by including surface coverage dependent activation energies for all adsorbed species to capture adsorbate - adsorbate interactions. This will be further discussed in Ch. 10.

7.1 Reactor model

A commercial program; AVL BOOST [94] was used in combination with user defined files in FORTRAN to conduct the kinetic modeling in **Papers VIII-X**. The same program was used to conduct the kinetic modeling of an NSR catalyst in **Paper XIII** as well. However, here details concerning the NH_3-SCR model presented in Paper VIII-X will be discussed. The ideal gas law is applied and all gas properties are evaluated depending on the temperature, pressure and gas composition. The channel was discretized into 15 longitudinally grid-points, where all equations including reactions were solved. The assumptions made for the reactor model in this thesis are:

i. Uniform radial flow distribution across the monolith.
ii. No diffusion resistance in the washcoat.
iii. The average coverage of the surface was used to model surface adsorption at each grid-point.
iv. The reaction heat during NH_3-SCR is very low and therefore no heat balances were solved [95].

The main governing equation for the gas phase species in a single channel model is [94]:

$$\varepsilon_g \frac{\partial \rho_g \cdot w_{k,g}}{\partial t} = \varepsilon_g \frac{\partial \rho_g \cdot w_{k,g} \cdot v_g}{\partial z} + MG_{k,g} \sum_i^{nr} v_{i,k} \cdot r_i(c_k, T_s, \theta_k) \quad (7.1)$$

The coverage of component k on the surface is solved by [94]:

$$\frac{\partial \theta_k}{\partial t}(\Theta \cdot GSA) = \sum_i^{nr} v_{i,k} \cdot r_i(c_k, T_s, \theta_k) \quad (7.2)$$

The geometric surface area per unit reactor volume, GSA, in Eq. 7.2 is given by [94]:

$$\frac{GSA}{d_{hyd}} = 4 \times (cell\ density) \tag{7.3}$$

Furthermore, mass-transport from gas bulk to the catalytic surface and vice versa is included. Under quasi steady-state conditions, the rates of the surface reactions balance the diffusive transport from the bulk gas to the surface. The molar surface concentration (c_k) of component k is evaluated using [94]:

$$GSA \cdot k_{k,m} \cdot (c_k - c_k^B) = \sum_i^{nr} v_{i,k} \cdot r_i(c_k, T_s, \theta_k) \tag{7.4}$$

where c_k^B is the concentration of species k in the gas bulk and $k_{k,m}$ is the mass transfer coefficient of the individual species calculated according to [94]:

$$k_{k,m} = \frac{Sh \cdot D_{k,g}}{d_{hyd}} \tag{7.5}$$

where $D_{k,g}$ is the diffusion coefficient of species k in the gas phase and the Sherwood number is calculated according to the Sieder/Tate relationship [96].

Mass-transport in the washcoat of Cu-ZSM-5 was examined by Olsson et al. [95] for NH_3-SCR. By simultaneously decreasing the amount of washcoat and the total flow with a factor of two the authors received the same conversion in the examined temperature interval (150-500°C). These results indicate that mass-transport resistance in the washcoat is limited. However, at medium to higher temperatures full conversion was reached which makes the evaluation of mass transfer at these temperatures difficult. In a recent study by Colombo [81] gradients in the washcoat were modeled during SCR conditions from 150 to 500°C and no significant concentration differences in the washcoat were observed. We have therefore not included mass-transport in the washcoat in the present work, which is also the case for several previous studies [37, 95, 97, 98]. There is still a possibility that there are mass-transfer limitations in the washcoat under our reaction conditions and therefore the received parameters should be considered as apparent rate parameters.

7.2 Kinetic parameters

The reaction rate is usually proportional to the concentration of the reactant and increases with increasing concentration. Furthermore, the reaction rate increases when the temperature increases. As rule of thumb (not always!), the rate of a reaction is doubled for every 10 K increase in temperature [27]. Therefore, in heterogeneous catalysis the reaction rate varies with the partial pressure of the reactants and temperature. To simulate and capture the temperature dependence, the Arrhenius equation is used for the rate constants, k:

$$k_i = A_i e^{-E_{A_i}/RT_s} \tag{7.6}$$

where A_i, called pre-exponential factor and E_{Ai}, the activation energy are fitted to the experiments. Furthermore, all fitted parameters in the model (**Papers VIII-X**) are fitted according to the Nelder-Mead method [99] to the corresponding experiments.

7.2.1 Thermodynamic restrictions

Thermodynamic restrictions for NH_3 spillover and NO oxidation were used to fulfill the equilibrium reactions, i.e. the net enthalpy and net entropy remain constant. Thermodynamic

restrictions are placed in the reactions in the models. For the enthalpy, this equation must be constant [100]:

$$\sum_i v_i E_{i,forw} - \sum_i v_i E_{i,rev} = \Delta H_{net} \quad (7.7)$$

where $E_{i,forw}$ and $E_{i,rev}$ is the activation energy for the forward and reverse reaction, respectively. The entropy change of an equilibrium reaction must also fulfill the restrictions according to:

$$\sum_i S_i = \Delta S_{net} \quad (7.8)$$

where ΔS is calculated according to:

$$\Delta S = R ln \frac{A_f}{A_b} \quad (7.9)$$

From the above equations the activation energy and pre-exponential factor can be determined and the equilibrium constant $K_{eq,i}$ according to:

$$\ln K_{eq,i} = -\frac{\Delta H_i}{RT} + \frac{\Delta S_i}{R} \quad (7.10)$$

8 Hydrothermal deactivation

The experimental studies in **Paper I-II** are used in this thesis to evaluate the ageing process of Fe-BEA as NH_3-SCR catalyst after (hydro-) thermal treatment. The focus is paid on the dynamics of the active sites after ageing. The changes in activity in **Paper I** are discussed in relation to changes of the characteristics of the samples caused by the hydrothermal treatment. Changes in storage capacity are studied in **Paper II** and discussed regarding high surface coverage of ammonia during the SCR reaction. Furthermore, in **Paper III** different iron species are identified and studied before and after thermal treatment using DRIFTS.

8.1 Catalyst characterization

8.1.1 Ammonia storage capacity

Temperature programmed desorption was performed to investigate the change in ammonia storage capacity after hydrothermal treatment. Figure 8.1a shows NH_3-TPD experiments in absence of water from **Paper II**. The ammonia storage capacity is considerably higher for the fresh than for the aged samples. As the capacity to store ammonia mainly is related to the amount of Brønsted acid sites and to minor extent also to the number of iron sites [7, 74, 98, 101, 102] the NH_3 storage capacity of the zeolite decreases if the Brønsted acidity is lost during hydrothermal treatment due to dealumination of the zeolite [74].

A kinetic model was developed to describe the experimental NH_3 desorption profiles Figure 8.1a, to obtain a more detailed understanding of the ammonia adsorption and desorption. Four different adsorption sites denoted W, $Z_{Br,S1}$, $Z_{Br,S2}$ and Z_L were used to model H-BEA. Furthermore, an additional site was included to represent ammonia adsorption on isolated iron sites, denoted Fe. The sites have different adsorption energies, where (W) represents weakly bound ammonia, ($Z_{Br,S1}$ and $Z_{Br,S2}$) describes Brønsted acid sites and (Z_L) represents strong Lewis sites. Previous studies have shown that the main desorption peak for H-BEA can be described by desorption from two main adsorption sites with different binding energies to ammonia which is the reason for including the two sites $Z_{Br,S1}$ and $Z_{Br,S2}$ to describe the main desorption peak in the present study [103, 104]. Furthermore, the adsorption energy of ammonia on iron sites (Fe) was fitted according to the found binding energy in the developed ageing model in **Paper VIII** (cf. Chapter 10). Figure 8.1a shows the results from the kinetic model of the ammonia desorption. The experiments and simulations show that the stronger adsorption sites are more sensitive to hydrothermal treatment than the weaker sites. This could be the reason of the shift in the desorption maximum towards lower temperature which is usually observed for NH_3-TPD experiments in presence of water.

Furthermore, XRD experiments for Fe-BEA samples in **Paper I** shown in Figure 8.1b, indicate a decrease of the zeolite crystals mean size and hence loss of Brønsted acidity. The FWHM of the diffraction peak at $2\theta = 22.7^0$ which is characteristic for the *BEA structure was used to calculate the mean size of the zeolite primary crystals using the Scherrer equation. Table 8.1 shows the mean size of the zeolite crystals before and after hydrothermal treatment.

8.1.2 Oxidation state of iron

XPS measurements were performed in **Paper I** to study the change in oxidation state of iron in the Fe-BEA samples after hydrothermal treatment. In order to analyze the XPS spectra for each sample, deconvolution of the Fe $2p_{3/2}$ peak was performed by fitting a Gaussian-Lorentzian (GL) function. The results from the XPS measurements are presented in Table 8.1 where the ratio between the fitted Fe^{3+} peak and the sum of the fitted Fe^{3+} and Fe^{2+} peaks are shown. The results show a clear increasing relative amount of Fe^{3+} with increasing ageing time and temperature, indicating a continuous formation of larger iron particles, Fe_2O_3.

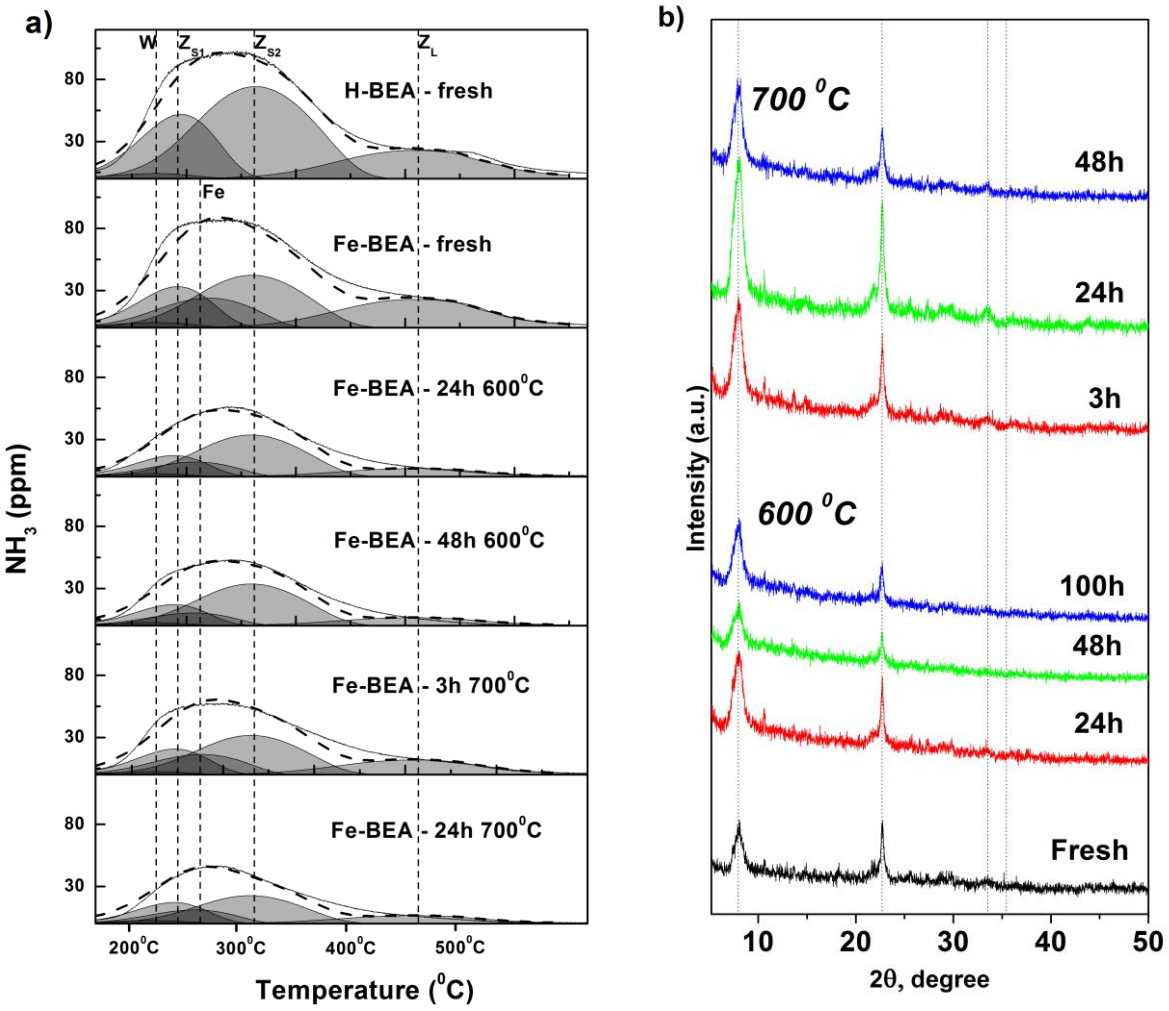

Figure 8.1. ***(a)*** *NH_3 outlet concentration during NH_3-TPD experiments and simulations of fresh and aged* ***1 wt. % Fe-BEA*** *and H-BEA samples. The positions of the modeled sites are marked with dashed lines through the figure for comparison between samples, W for weak adsorption site, Z_{S1} and Z_{S2} for Brønsted sites, Z_L for Lewis site, and Fe for iron site. The samples were exposed to 400 ppm NH_3 for 40 min at 150°C, followed by 30 min Ar and finally a temperature ramp of 10°C/min up to 500°C was applied.* ***(b)*** *X-ray diffractograms of fresh and aged* ***6 wt. % Fe-BEA*** *catalysts.*

Table 8.1. *Specific surface area, relative amount of Fe^{3+} and the calculated zeolite BEA mean crystal size calculated by the Scherrer equation for fresh and hydrothermally treated* ***6 wt. % Fe-BEA****.*

Ageing time (h)	Ageing temperature (°C)	Specific surface area (m^2/g)	$\frac{Fe^{3+}}{(Fe^{3+}+Fe^{2+})}$ [%]	Zeolite mean crystal size (nm)
Fresh	-	114	51	52
24	600	113	53	48
48	600	107	62	47
100	600	106	63	45
3	700	109	58	49
24	700	107	61	45
48	700	103	73	44

8.1.3 NO storage capacity

Temperature desorption of NO in absence of water was performed in **Paper II** to study the NO storage capacity after hydrothermal treatment, shown in Figure 8.2. The results show that adsorption of NO is strongly related to the iron species and not to the zeolite. Furthermore, similar to the NH_3-TPD experiments the storage capacity of NO is sensitive to hydrothermal treatment, indicating loss of adsorption sites for NO after deactivation. The decreased storage capacity of NO can be correlated to loss of isolated iron species due to formation of larger iron particles shown in the XPS results in Table 8.1.

8.2 Catalytic activity

8.2.1 NO and NH_3 oxidation

The results of the NH_3 and NO oxidation experiments from **Paper I** are shown in Table 8.2. NH_3 oxidation experiments at 500°C show a strong decrease in activity after short time of ageing. For Fe-ZSM-5, Brandenberger et al. [74] found a strong correlation between the concentration of dimeric iron species (Fe^{2+}) and the activity for NH_3 oxidation. The decreased activity for ammonia oxidation for the aged Fe-BEA samples in the present study can be correlated with the decreased relative amount of Fe^{2+} from the XPS measurements indicating decreased amount of dimeric iron species.

Furthermore, oxidation of NO to NO_2 has been shown to proceed over Fe_2O_3 particles (Fe^{3+}) [105]. The activity measurements in the present study show that all the aged samples have higher NO oxidation activity compared to the fresh sample. The XPS study shows that the relative amount of Fe^{3+} increases (c.f. Chapter 8.1.2) in the Fe-BEA samples with increased hydrothermal treatment. The increase in oxidation state could explain the increased activity for the aged samples during NO oxidation which agrees with other studies showing higher activity for NO oxidation with increased concentration of Fe_2O_3 particles [72, 105]. However, the samples with the shortest ageing time have the highest activity. The continuous increase of relative amount of Fe^{3+} in the samples indicates that the iron oxide particles grow with hydrothermal treatment forming larger iron oxide particles with lower total active surface area. Hence the growing particles could be the reason for the maximum in NO oxidation with hydrothermal treatment temperature and time.

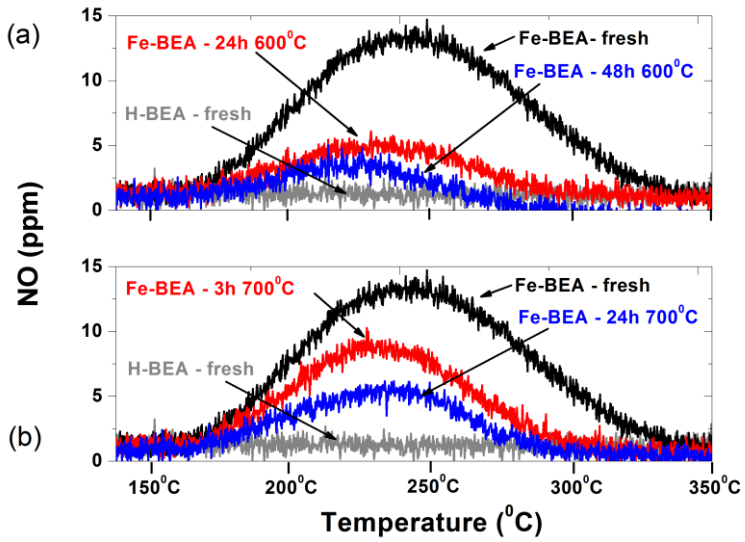

Figure 8.2. *NO outlet concentration during NO-TPD experiments. Fresh H-BEA and* ***1 wt. % Fe-BEA*** *samples compared with* ***1 wt. % Fe-BEA*** *aged at (a) 600°C for 24 and 48h and (b) 700°C for 3 and 24h. The samples were exposed to 400 ppm NO for 40 min at 150°C, followed by 30 min Ar and finally a temperature ramp of 10°C/min up to 500°C was applied.*

Table 8.2. *Conversion during NH_3 and NO oxidation for fresh and hydrothermally treated* ***6 wt. % Fe-BEA****. The samples were exposed to 400 ppm NH_3 or NO, 8% O_2 and 5% H_2O in Ar.*

Ageing time (h)	Ageing temperature (^{0}C)	NH_3 oxidation (%) at 500^{o}C	NO oxidation (%) at 400^{o}C
Fresh	-	73	15
24	600	32	19
48	600	26	18
100	600	23	18
3	700	35	23
24	700	17	19
48	700	12	17

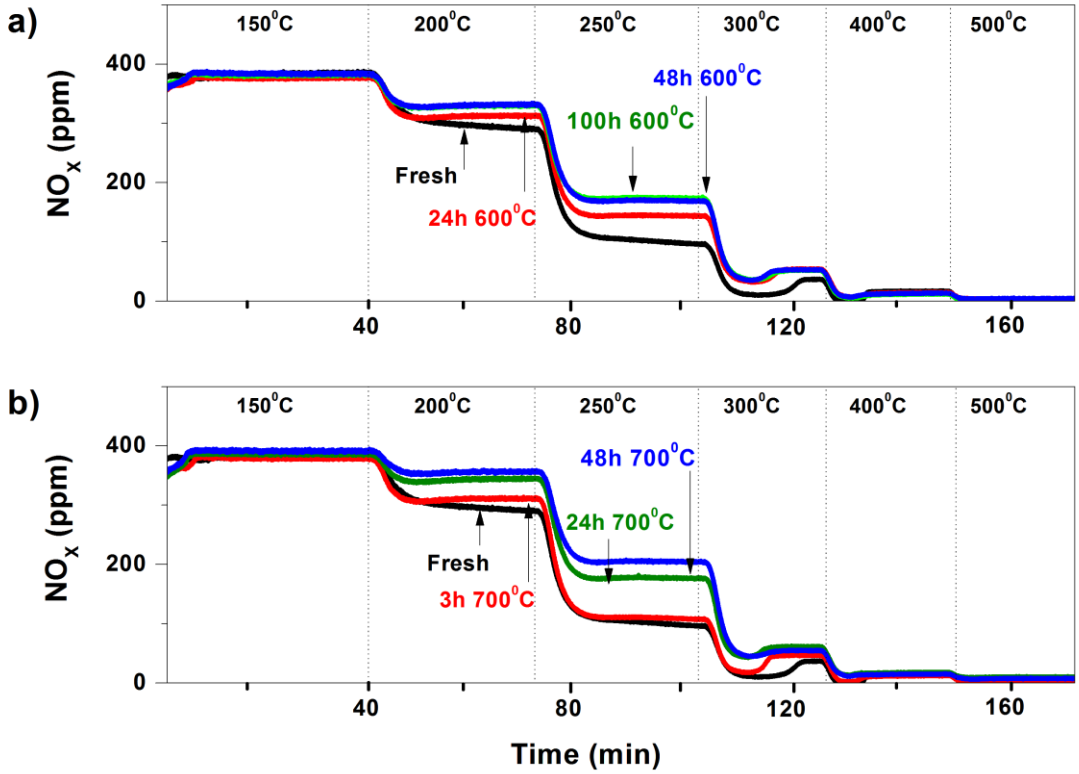

Figure 8.3. *Outlet concentration of NO_X during NH_3-SCR for* ***6 wt. % Fe-BEA*** *samples aged at 600 and 700^{o}C compared to a fresh 6 wt. % Fe-BEA sample. The samples were exposed to 400 ppm NO, 400 ppm NH_3, 8 % O_2 and 5 % H_2O in Ar and the temperature was stepwise increased from 150 to 500^{0}C.*

8.2.2 NH_3-SCR

NH_3-SCR experiments performed in **Paper I** to evaluate the ability of the samples to reduce NO_X before and after hydrothermal treatment are shown in Figure 8.3. The NH_3-SCR experiments show that the low-temperature SCR (below 300^{o}C) reaction is more sensitive to hydrothermal treatment, which indicates a significant loss of active iron species. However, a large fraction of the catalyst is not used at high temperatures due to high reaction rates. Therefore, the deactivation must be severe until it is observed at higher temperatures (> 400^{o}C), which could be the reason for the low degree of deactivation observed at high temperatures. Brandenberger et al. [74] found that growth of

iron particles occurred after migration of isolated iron species and proposed that migration of such species is the main reason for the decreased NO_X conversion. Different iron species cannot be resolved here, however, the increase of Fe^{3+} indicates an increase of the iron bound as Fe_2O_3 which is in line with the results in the study by Brandenberger et al. [74]. Furthermore, the decrease in ammonia storage capacity after ageing does not seem to affect the SCR activity. The least aged sample (700^{o}C for 3 h) did not show any significant decrease in activity even though the NH_3-TPD experiment showed a strong decrease in ammonia storage capacity (not shown). This indicates that the NO_X conversion is sensitive to the loss of active sites for the SCR reaction and not directly to the amount of ammonia adsorbed in the zeolite.

8.2.3 Ammonia inhibition

The effect of high storage capacity of ammonia during NH_3-SCR was further studied in **Paper II**, where ammonia inhibition experiments were performed, shown in Figure 8.4. During the ammonia inhibition experiments the gas feed consisted of 400 ppm NO, 400 ppm NH_3, 8% O_2 and 5% H_2O. The samples were exposed to the gas mixture at two temperature levels; 250 and 300^{0}C for 40 min each. The NH_3 feed was then cut off and compensated with inert gas to maintain constant total flow. The SCR activity was continuously measured before and after the ammonia cut-off. The results in Figure 8.4 show two very clear but different trends. The H-BEA samples showed a direct correlation between increased NO_X conversion (i.e. period with increased NO_X conversion after ammonia cut-off) and storage capacity of ammonia. The period with increased NO_X conversion decreases with decreasing ammonia storage. However, for the Fe-BEA samples a different trend is observed. When measuring the period with increased NO_X conversion the results indicate that high surface coverage of ammonia does not significantly affect the SCR activity over the Fe-BEA samples in the same way as for H-BEA. The fresh and aged Fe-BEA samples show a similar increased NO_X reduction time.

8.3 DRIFT spectroscopy

Figure 8.5 shows the in situ DRIFT spectra recorded just when the samples are saturated with nitric oxide during NO adsorption at 150^{0}C from the results in **Paper III**. Before NO exposure, the samples are pretreated in oxygen. Fresh H-BEA and 1 wt. % Fe-BEA are compared to thermally treated Fe-BEA. The DRIFT spectra show three distinct peaks centered around 2134, 1880-1870 and 1635 cm^{-1}. The absorption peak at 2134 cm^{-1} is assigned to stretching vibrations of ionic NO^+ species, strongly bound to Fe^{3+} sites [75, 106-108]. Furthermore, this peak has also been assigned to NO^+ ions bound to Brønsted acid sites in the zeolite [109-111]. The peak centered around 2134 cm^{-1} is seen both for H-BEA and for fresh Fe-BEA with increased intensity, indicating NO^+ ions bound to both Brønsted sites and Fe^{3+} species. For the aged Fe-BEA samples the intensity of this peak decreases indicating loss of adsorption sites for NO^+ ions after ageing, which agrees well with our previous study that a decrease of adsorption sites for NO, results in decreased NH_3-SCR activity for both H-BEA and Fe-BEA. The absorption bands in the range 1950-1800 cm^{-1} represent NO_X adsorption on different iron species [110, 112-114]. The spectra show two overlapping peaks at 1880 and 1870 cm^{-1}, representing isolated iron sites (Fe^{3+} or Fe^{2+}) [110, 112-114] and iron clusters (Fe_xO_y), respectively [110, 112], located in the porous system of the zeolite. The merged peak shifts towards the position of the peak for the iron clusters after ageing, indicating that the isolated iron species are sensitive to relatively mild ageing. These results agree well with the previous activity studies, which indicate that isolated iron species (monomeric and dimeric) are sensitive to ageing leading to decreased activity for both NH_3-SCR and NH_3-oxidation.

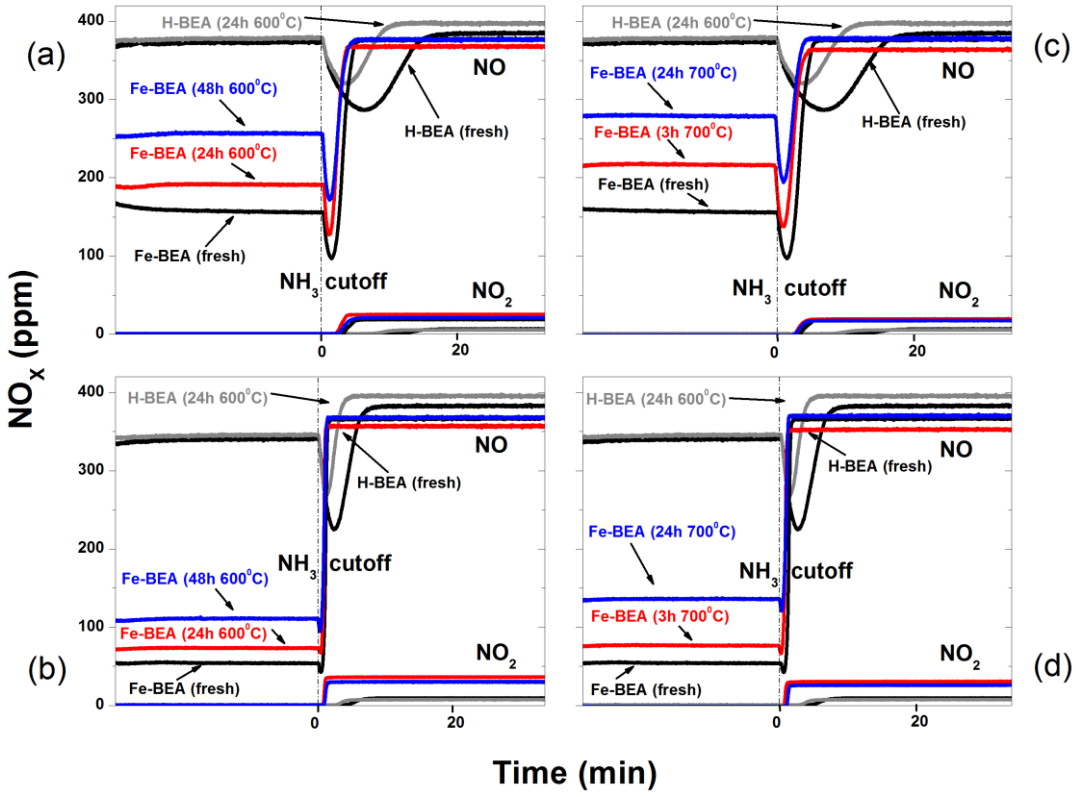

Figure 8.4. *Ammonia inhibition experiments.* ***(a)*** *and* ***(b)*** *show the outlet NO_X concentration during NH_3-SCR at 250 resp. 300^{0}C for the fresh H-BEA and* ***1 wt. % Fe-BEA*** *samples compared to the aged H-BEA (24h-600^{0}C) and aged* ***1 wt. % Fe-BEA*** *samples at 600^{0}C for 24 and 48 h.* ***(c)*** *and* ***(d)*** *show the results during NH_3-SCR at 250 resp. 300^{0}C for the fresh H-BEA and* ***1 wt. % Fe-BEA*** *samples compared to the aged H-BEA (24h-600^{0}C) and aged* ***1 wt. % Fe-BEA*** *samples at 700^{0}C for 3 and 24 h.*

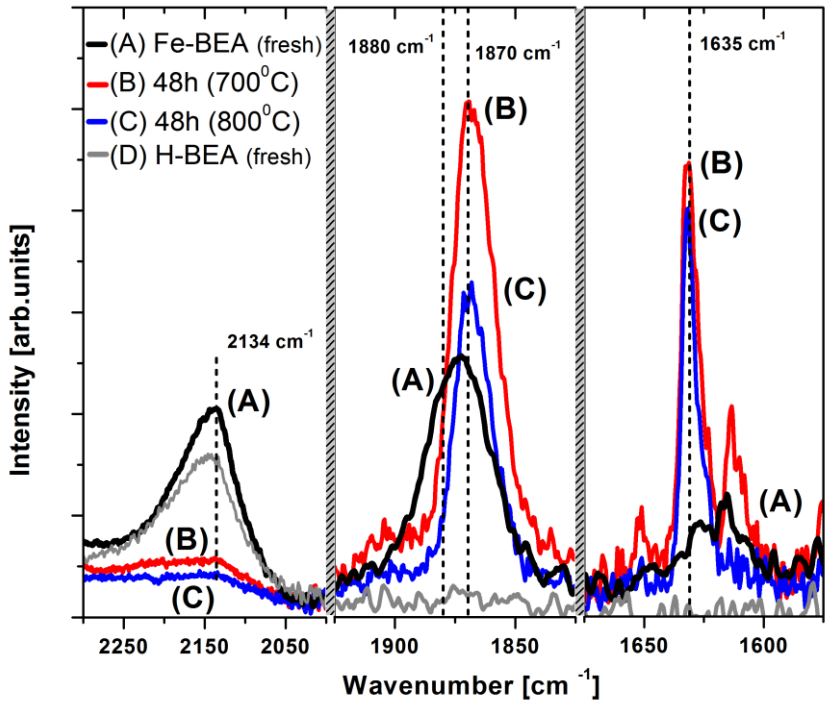

Figure 8.5 *DRIFT spectra of fresh H-BEA and* ***1 wt. % Fe-BEA****, and thermally treated Fe-BEA samples, during exposure to 400 ppm NO and Ar (inert) at 150^{0}C for 30 min.*

The absorption peaks around 1635 cm^{-1} in Figure 8.5, represent NO_2 adsorbed on Fe-species [114-116]. Mul et al. discussed the structure of the iron species giving rise to the absorption at 1635 cm^{-1} and concluded that these species are larger Fe_2O_3 particles, located outside the zeolite pores [110]. In the present study the intensity of the absorption peak at 1635 cm^{-1} increases with ageing after thermal treatment up to 700^{o}C which together with the evolution of the peak at 1870 cm^{-1}, indicate that growth of smaller iron clusters first occurs in the zeolite pores. Furthermore, the intensity of this peak decreases for the more severely aged samples at 800^{o}C, indicating loss of adsorption sites, most probably due to particle growth during ageing. The results from Mul et al. in combination with the DRIFTS results agree well with our activity results which show increased NO oxidation activity due to growth of iron oxide particles. However, the NO oxidation reached a maximum in activity with ageing, which can be explained by lower active surface area with particle growth due to ageing as seen in Figure 8.3 for the more severely aged samples.

8.4 H_2 - pretreatment

The effect of high-temperature hydrogen treatment of Fe-BEA is evaluated in relation to NH_3-SCR activity together with DRIFT and UV-Vis spectroscopy in **Paper IV and V**. Previously, it has been shown that H_2-pretreatment of Fe-ZSM-5 has a beneficial effect on the activity and stability of this type ofcatalyst [115, 117]. The main reason for the promotional effect of hydrogen pretreatment is suggested to be that smaller iron oxide clusters break into smaller units, which are stabilized by forming bonds to the zeolite matrix. H_2-treatment at higher temperatures could lead to re-dispersion of iron oxide clusters to smaller iron species in the zeolite, which thereafter leads to increased SCR activity. In **Paper IV**, 0.5-4 wt. % Fe-BEA catalysts were prepared to investigate if the hydrogen treatment is dependent on the iron concentration of the samples. All catalysts were characterized with UV-Vis spectroscopy before deposited on monoliths. It was observed that the concentration of larger iron species increases with the iron concentration of the samples, which agrees well with the results from Brandenberger et al. presented previously in Figure 4.4. The increase in NH_3-SCR activity was most pronounced for the 2 wt. % sample and the lowest increase was seen for the 0.5 wt. % sample. This could be correlated to the UV-Vis results, which showed that the 0.5 wt. % Fe-BEA sample had the lowest amount of iron clusters and almost no iron particles compared to the other samples with higher iron loading which could be the reason that hydrogen treatment did not result in an increased activity.

Table 8.3. *NO_X conversion during NH_3-SCR for the **2 wt. % Fe-BEA** sample after different pretreatment conditions: (a) fresh sample; (b) after H_2-pretreatment; (c) after hydrothermal aging at 700^{0}C for 24 h; (d) after H_2-treatment of the aged sample referred as regeneration.*

	NO_X conversion, (%)			
Temperature (^{o}C)	Fresh	H_2-treated	Aged	H_2-treated aged
150	2	2	1	2
200	16	25	11	15
250	55	72	41	45
300	87	90	77	80
400	95	92	91	91
500	98	94	93	93

Due to the relatively large activity increase for the 2 wt. % Fe-BEA sample, the effect of hydrogen treatment for a hydrothermally aged sample was studied. The fresh sample was initially treated with H_2, aged for at 700^0C for 24 h and finally treated with hydrogen again for regeneration. Table 8.3 shows the NO_X conversion during NH_3-SCR for the fresh, H_2-treated, aged and H_2-regenerated sample. As seen in Table 8.2 the hydrogen treatment affects the low-temperature SCR region significantly positively whereas the hydrothermal treatment has a negative impact on the same region. The increased activity observed after hydrogen treatment both before and after hydrothermal ageing indicates a higher concentration of isolated iron species due to the hydrogen treatment. However, the catalyst could only be partially and not fully regenerated after hydrothermal treatment. This is believed to be due to loss of Brønsted acid sites in the catalyst after hydrothermal treatment which are needed for the isolated iron species to bind to the zeolite structure.

The 2 wt. % Fe-BEA sample was further studied in **Paper V**, using DRIFT and UV-Vis spectroscopy after hydrogen treatment. The results are shown in Figure 8.6. The UV-Vis results show a significant decrease in the relative concentration of the larger iron species and increase of the relative amount of isolated iron species after hydrogen treatment. This is in good correlation with the activity study in **Paper IV**, where the low-temperature SCR activity increases significantly after hydrogen treatment. This strongly indicates that re-dispersion of the isolated iron species is the reason for the increased low-temperature SCR activity. The DRIFT spectra recorded just when the samples are saturated with nitric oxide during NO adsorption at 150^0C, show that the two overlapping peaks at 1880 and 1870 cm^{-1}, representing isolated iron sites (Fe^{3+} or Fe^{2+}) and iron clusters (Fe_xO_y), increases significantly after hydrogen treatment. When correlated to the UV-Vis results, the increased absorption peak is most likley due to isolated ison species and not to iron clusters. This results further indicates that hydrogen treatment of Fe-BEA increases the distribution of isolated iron species in the zeolite structure, hence increaseing the low-temperature SCR activity.

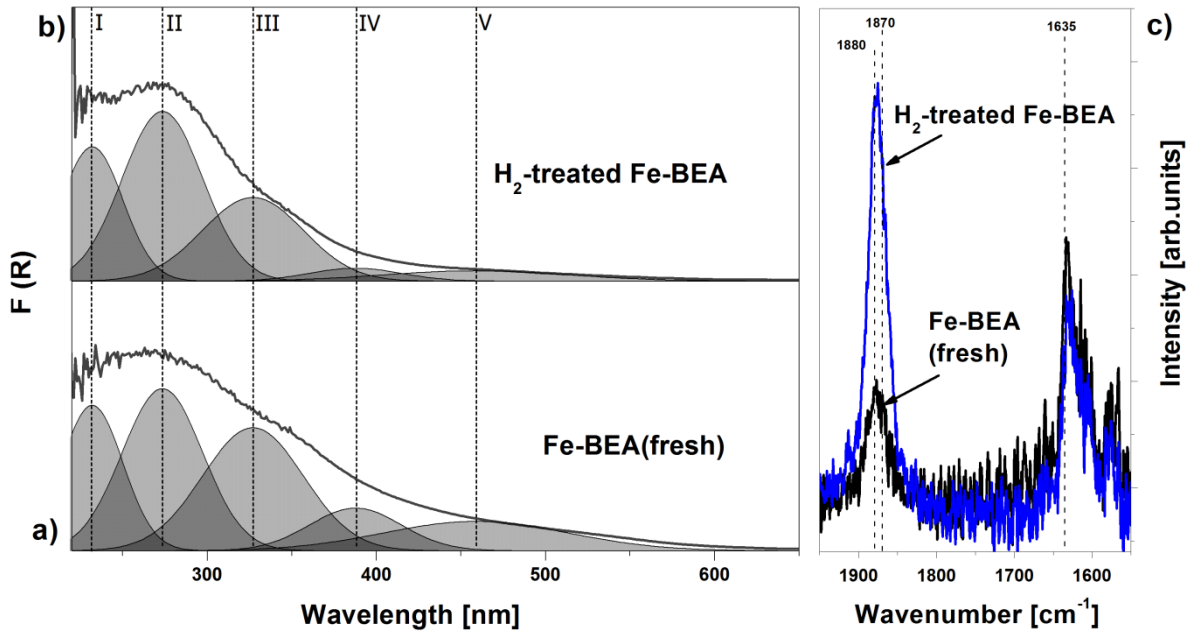

Figure 8.6. *UV-Vis spectra of iron from the* ***(a)*** *fresh and* ***(b)*** *H_2-treated* ***2 wt. % Fe-BEA*** *powder sample after subtraction of the corresponding spectrum for H-BEA. The deconvoluted peaks* ***(I-II)*** *represent monomeric iron species (220-290 nm),* ***(III-IV)*** *dimeric and smaller iron clusters (300-400 nm), and* ***(V)*** *larger iron oxide particles (>400 nm). (c) DRIFT spectra of fresh* ***2 wt. % Fe-BEA*** *and H_2-treated Fe-BEA samples, during exposure to 400 ppm NO and Ar (inert) at 150^0C for 30 min.*

9 Chemical deactivation

The experimental studies in **Paper VI and VII** are used in this thesis to evaluate the chemical deactivation (poisoning) mechanism of Fe-BEA as NH_3-SCR catalyst after phosphorous (**Paper VI**) and potassium (**Paper VII**) exposure. The focus is paid on the active iron sites, hence exposure of the catalyst to relative low amounts of chemical poison (10 and 50 ppm H_3PO_4 or KNO_3). The changes in activity for the catalysts are discussed in relation to changes of the characteristics of the samples caused by the poisoning. Changes in storage capacity are studied and discussed regarding to high surface coverage of ammonia during the SCR reaction. Furthermore, XPS is used to study phosphorous and iron species together with NO- and NO_2-TPD experiments and correlated with decreased catalytic activity.

9.1 Phosphorous exposure

The 1 wt. % Fe-BEA samples were exposed to 10 and 50 ppm phosphoric acid is gas phase for 14, 24 and 48 h at 350^{o}C. The results showed that the degree of deactivation is strongly dependent on the phosphorous exposure time and not on the concentration of phosphoric acid under those conditions. The rate of deactivation is the same for 10 and 50 ppm H_3PO_4, and therefore only the results for the samples exposed to 50 ppm phosphorous are shown and discussed in the coming sections.

9.1.1 Ammonia storage capacity

To investigate the ammonia storage capacity after phosphorous exposure, temperature programmed desorption of NH_3 was performed. The results are shown in Figure 9.1a, where the amount of desorbed ammonia in presence of water is summarized for the studied samples and compared to the amount of weakly and strongly bound ammonia for the samples exposed to 50 ppm H_3PO_4. All poisoned samples show a higher storage capacity of strongly bound ammonia compared to the fresh sample while the amount of weakly bound ammonia follows the opposite trend compared to the strongly bound NH_3. The XPS results show a relative high concentration of phosphorous pentoxides (P_2O_5) for the samples with shorter time of phosphorous exposure (14 and 24 h) while longer time of phosphorus exposure shows a relative decrease in P_2O_5. This indicates that the change in storage capacity may be due to the formed phosphorous pentoxides. The NH_3-TPD results show that the number of acid sites to store strongly bound ammonia increases at the expense of the sites for weakly bound ammonia likely do to formation of phosphorous pentoxides.

9.1.2 X-ray photoelectron spectroscopy and NO adsorption

XPS measurements were performed to study and identify the formed phosphorous species on the surface where the XPS results are correlated to the storage capacity of NO in the samples. Figure 9.1b shows the NO-TPD results correlated to the XPS results. The deconvolution of the XPS spectra of the phosphorous peak shows that metaphosphates, PO_3^-, are formed after longer time of exposure which can be correlated to the decreased storage capacity of NO. As previously discussed, the storage capacity of NO is related to isolated iron species; hence the formation of metaphosphates indicates that the hydroxyl (OH^-) groups on the active iron species are replaced with metaphosphates.

9.1.3 NO and NH_3 oxidation

The NO and NH_3 oxidation experiments from **Paper VI**, show a clear decrease in activity at higher temperatures (not shown). It has previously been discussed that the NH_3-oxidation over Fe-BEA is very sensitive to loss of active dimeric iron species. The results in the present study show a clear decrease in activity for NH_3 oxidation at 500^{O}C, indicating loss of active dimeric iron sites for the samples exposed to phosphorous for the longest time. It was discussed that the metaphosphates block the iron species. The decreased activity with increasing relative amount of metaphosphates

indicates that the hydroxyl groups are replaced by metaphosphates which deactivate the dimeric iron species by blocking the access to the iron site. Furthermore, the NO-oxidation activity is less affected. However, the results show a constant stepwise decrease in NO oxidation activity with increased phosphorous accumulation. NO oxidation has been shown to proceed over iron particles Fe_2O_3 and the stepwise decrease in activity indicates that the iron particles most likely are physically blocked by the accumulation of phosphorous on the surface. However, it should not be excluded that the deactivation of the iron particles is a combination of physical and chemical deactivation.

9.1.4 NH_3-SCR and ammonia inhibition

The NH_3-SCR experiments show a significant decrease in low-temperature SCR activity after longer time of phosphorous exposure indicating a significant decrease in the number of active monomeric iron sites, shown in Figure 9.2. However, during high-temperature SCR the activity is not significantly affected due to similar reasons as previously discussed for the hydrothermally treated samples. The decreased SCR activity can be correlated to the XPS measurements and NO-TPD experiments which suggest that monomeric iron species are chemically deactivated due to formation of metaphosphates.

Furthermore, the period with increased NO_X reduction after the ammonia cut-off decreases with increasing phosphorous exposure. This indicates that the increased amount of strongly bound ammonia due to phosphorous exposure does not participate in buffering the active iron sites with ammonia during the NH_3-SCR reaction.

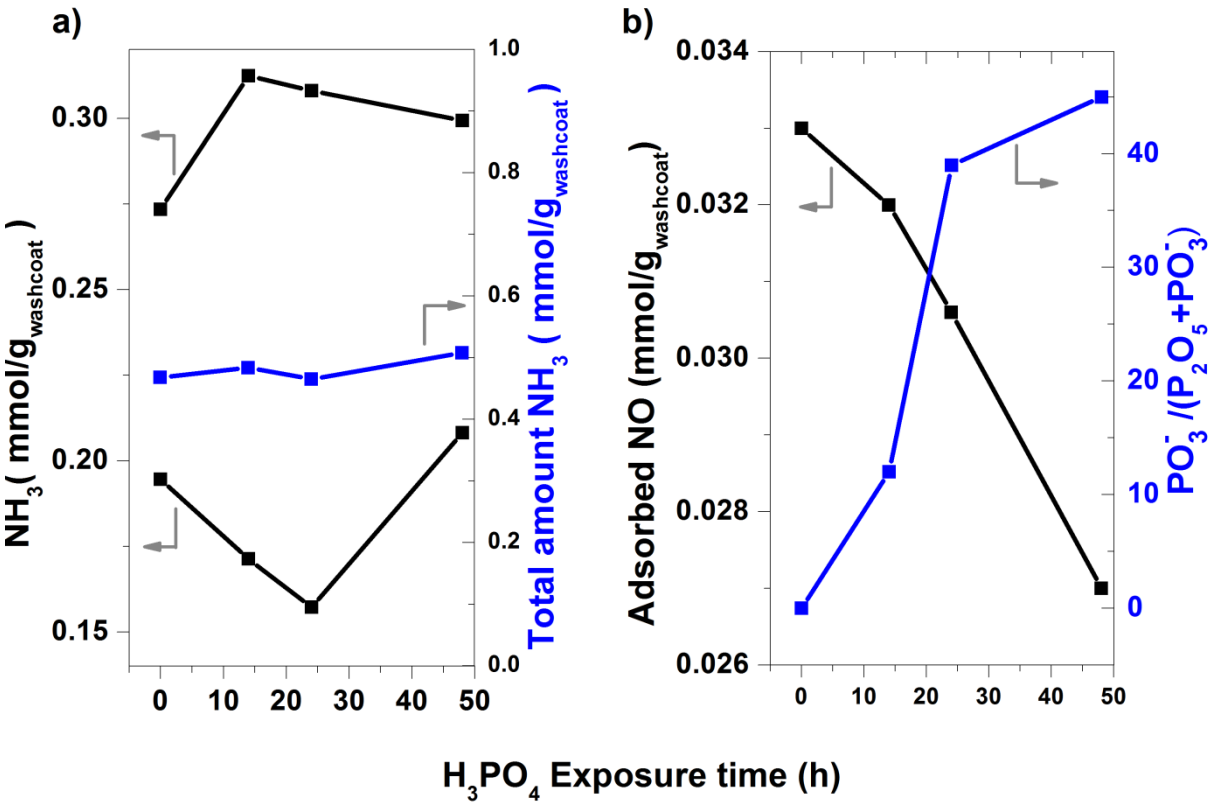

Figure 9.1. a) *The amount of weakly and strongly bound ammonia together with the total amount of ammonia desorbed during the NH_3-TPD experiments.* ***b)*** *Total amount of adsorbed NO during NO-TPD experiments compared to the relative concentration of PO_3^- calculated from the deconvoluted P 2p XPS spectra. The amount of stored NH_3 is shown as a function of the H_3PO_4 exposure time.* ***1 wt. % Fe-BEA*** *samples exposed to 50 ppm H_3PO_4 for 14, 24 and 48 h.*

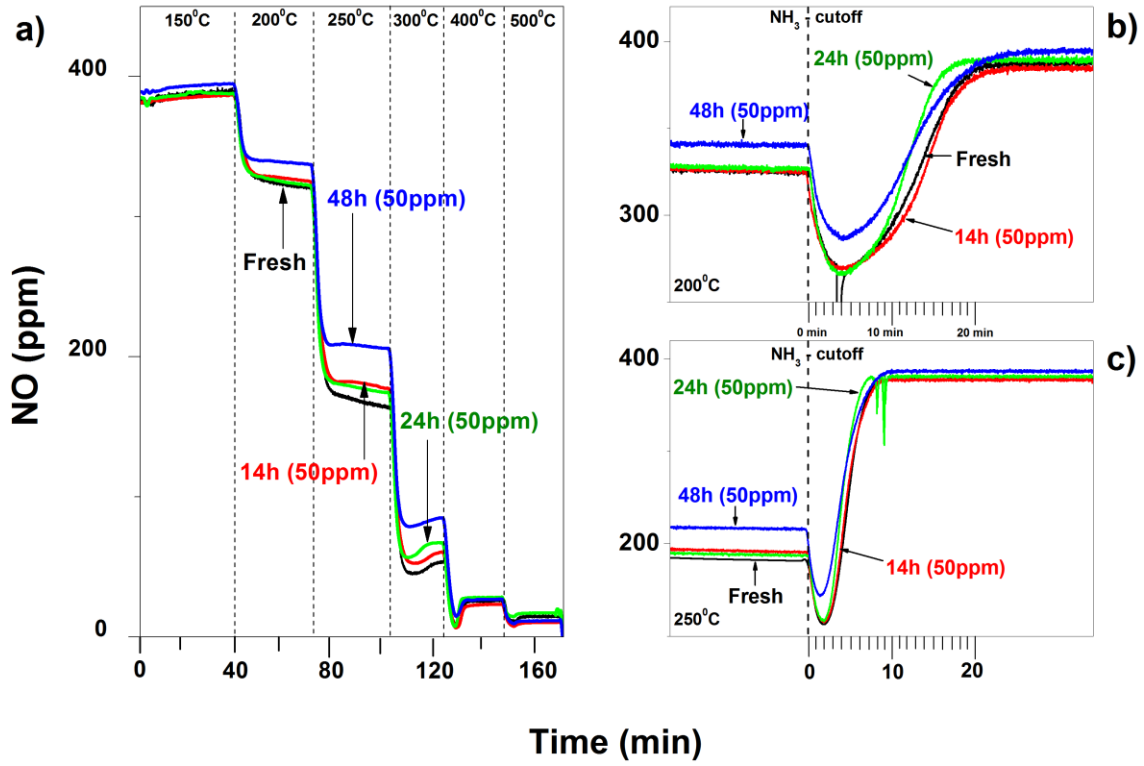

Figure 9.2. *Outlet concentration of NO during* ***(a)*** *NH_3-SCR and* ***(b-c)*** *ammonia inhibition experiments for* ***1 wt. % Fe-BEA*** *phosphorous deactivated samples compared to a fresh sample. The samples were exposed to 400 ppm NO, 400 ppm NH_3, 8 % O_2 and 5 % H_2O in Ar and the temperature was stepwise increased from 150 to 500^{0}C. Ammonia inhibition experiments were performed at 200 resp. 250^{0}C.*

9.2 Potassium exposure

The 1 wt. % Fe-BEA samples were exposed to 10 and 50 ppm potassium nitrate in gas phase for 14, 24 and 48 h at 350°C. The results showed that the degree of deactivation is dependent on both the potassium exposure time and the concentration of potassium nitrate under those conditions.

9.2.1 Ammonia storage capacity

The ammonia TPD experiments showed a clear decrease in storage capacity for all potassium exposed samples. Previous studies of iron-exchanged zeolites impregnated with potassium in solution [22] have shown a strong decrease in storage capacity. However, we do not observe such strong decrease in activity, indicating that impregnation with potassium results in more severe deactivation compared to phase flow exposure of potassium. Furthermore, the desorption maximum of the ammonia peak shifts first towards lower temperature thereafter towards higher temperatures after longer time of exposure, indicating that the weaker Brønsted site (c.f. section 8.1.1) is blocked after longer time of potassium exposure.

9.2.2 NO_X adsorption

H-BEA and Fe-BEA samples show a significant increase in NO_X storage capacity after potassium exposure as shown in Figure 9.3. I was previously shown that fresh H-BEA does not show any storage capacity of NO at all. However, after exposure to potassium a desorption peak of NO can be observed during the NO-TPD experiments, indicating formation of new adsorption sites in the zeolite. Furthermore, during NO_2-TPD experiments a new peak can be observed when the temperature reaches

around 250°C, which further indicates formation of a new adsorption site. It can be seen that the NO_2 desorption peak around 350°C decreases simultaneously during potassium exposure for the H-BEA sample. Similar trends are observed for the Fe-BEA samples. Potassium is a well-studied NO_X storage component for NO_X adsorbing catalysts. [86, 118-121]. Kobayashi et al. [86] studied the NO_X storage capacity of alkaline metals and found that potassium has the highest storage capacity. This could explain the increase in storage capacity for the potassium exposed H-BEA and Fe-BEA samples. Exposure to potassium appears to form new NO_X storage sites on the expense of Brønsted sites in the zeolite when correlated to the NH_3-TPD experiments.

9.2.3 NH_3-SCR and ammonia inhibition

The NH_3-SCR experiments in Figure 9.4 show a relatively large decrease in NO conversion in the low-temperature region (up to 300°C) for the Fe-BEA samples. However, the H-BEA samples show a significant increase in high-temperature SCR activity after potassium exposure. The increase in NH_3-SCR activity for the H-BEA samples can be correlated to the increased NO_X storage capacity. Nevertheless, increased NO_X storage capacity does not apply for the Fe-BEA sample, which indicates that exposure to potassium results in a decreased number of active sites.

Furthermore, the ammonia inhibition experiments show a clear difference between the fresh and potassium exposed samples. The period with increased NO reduction is strongly dependent on the total amount of ammonia stored in the catalyst. The samples exposed to 50 ppm potassium during NH_3-TPD showed a desorption peak maximum shifted towards higher temperatures which could explain the almost unchanged period with increased NO reduction, due to the slower release of ammonia. Furthermore, the potassium exposed samples have a lower steady-state NO_X reduction level compared to the fresh sample which could further explain the almost unchanged NO_X period with increased NO_X reduction.

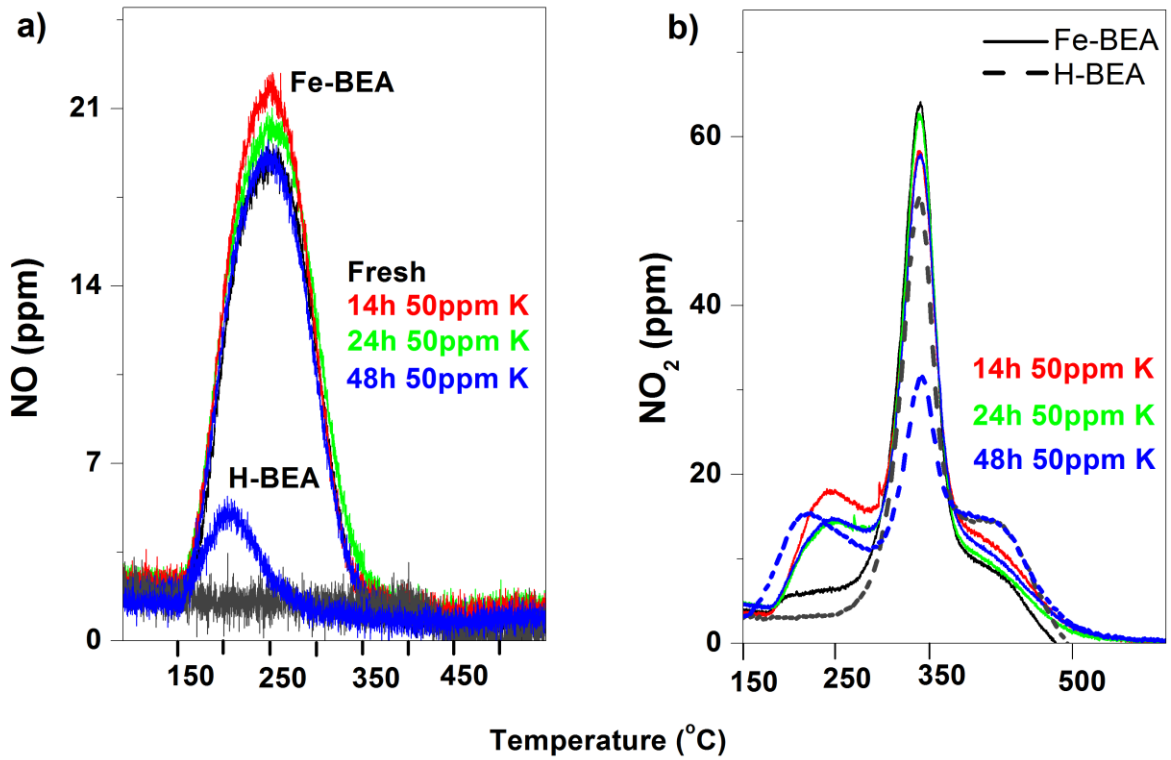

Figure 9.3. *NO and NO_2 outlet concentration during NO and NO_2-TPD experiments. Potassium exposed H-BEA and* ***1 wt. % Fe-BEA*** *samples compared with fresh samples. The samples were exposed to 400 ppm* ***(a)*** *NO or* ***(b)*** *NO_2 for 40 min at 150°C, followed by 30 min Ar and finally a temperature ramp of 10°C/min to 500°C was applied.*

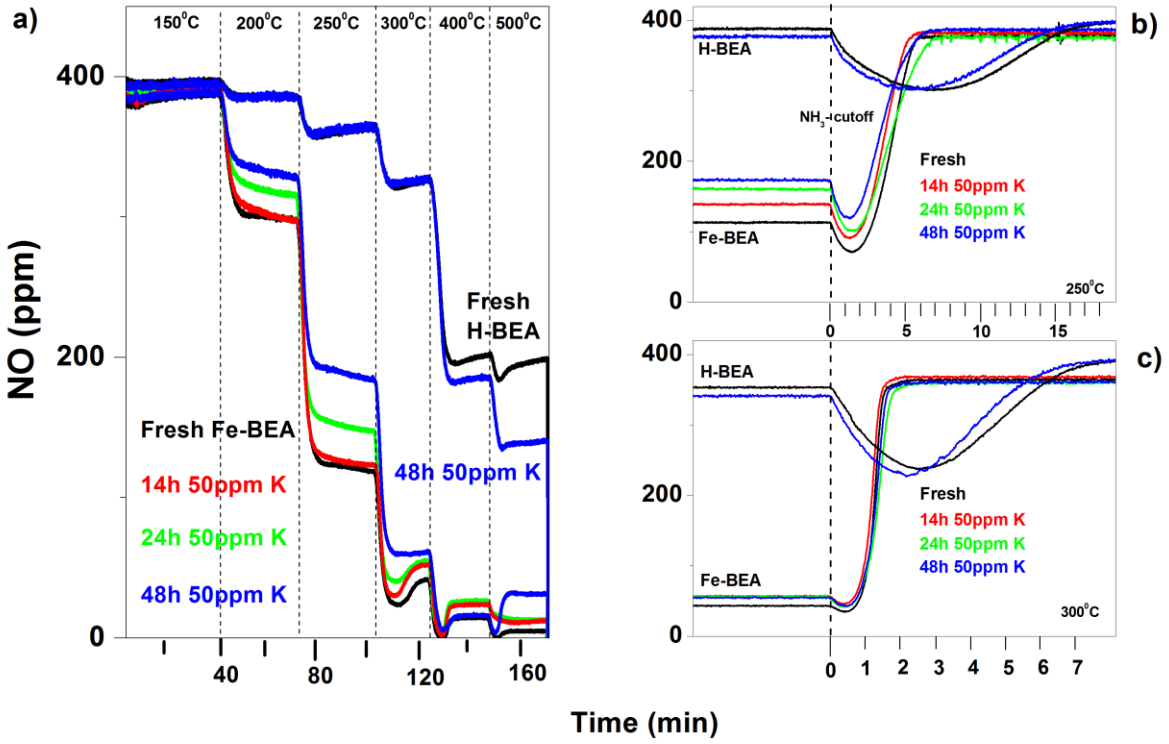

Figure 9.4. *Outlet concentration of NO during* ***(a)*** *NH_3-SCR and* ***(b-c)*** *ammonia inhibition experiments for* ***1 wt. % Fe-BEA*** *and H-BEA potassium deactivated samples compared to fresh sample. The samples were exposed to 400 ppm NO, 400 ppm NH_3, 8 % O_2 and 5 % H_2O in Ar and the temperature was stepwise increased from 150 to 500^{0}C. Ammonia inhibition experiments were performed at 250 resp. 300^{0}C.*

9.2.4 X-ray photoelectron spectroscopy

To further understand the nature of the iron species after potassium exposure, XPS measurements were performed. The deconvolution results from the XPS measurements of the Fe 2p peak for fresh and potassium exposed Fe-BEA show that the oxidation state of iron increases significantly with potassium exposure. The relative amount of Fe^{3+} increases from around 38 % for the fresh Fe-BEA catalyst to 55 % for the Fe-BEA sample exposed to 50 ppm potassium for 48 h. Furthermore, the activity results show a significant decrease for the potassium exposed samples indicating a significant loss of monomeric and dimeric iron species. For the hydrothermally treated samples the increase in oxidation state for iron indicates formation of iron cluster and particles due to migration of isolated iron species (monomeric and dimeric iron). However, the NO oxidation experiments for Fe-BEA do not show any activity change after potassium exposure, which indicates no formation of larger iron particles. Therefore the increase in oxidation state of iron after potassium exposure is most likely due to loss of isolated iron species forming trivalent iron clusters inside the zeolite pores. Furthermore, due to the relatively low exposure temperature (350°C) it is not likely that iron clusters migrate and form larger iron particles outside the zeolite pores similar to the hydrothermally treated samples. This indicates that when exposed to potassium the isolated iron species are exchanged with potassium forming smaller iron clusters inside the zeolite pores. Migration of iron inside zeolites has shown to occur at temperatures above 550°C [7, 74].

9.3 Summary of the deactivation and regeneration mechanism

Based on the experimental results from **Paper I-VII** the deactivation and regeneration mechanisms of Fe-BEA are summarized and schematically shown in Figure 9.5.

The ageing process of hydrothermally treated Fe-BEA proceeds into two steps where (i) milder ageing results in formation of iron clusters in the zeolite pores due to migration of isolated iron species, and (ii) more severe ageing results in continuous migration and formation of larger iron oxide particles located on the external surface of the zeolite crystals. Furthermore, the Brønsted sites in the zeolite are sensitive to hydrothermal treatment and therefore already after relatively mild ageing dealumination and loss of Brønsted sites occurs in the zeolite. By treating the catalyst with hydrogen at high temperatures, iron can be redispersed, forming isolated iron species. After hydrothermal treatment the catalyst can only be partially regenerated using hydrogen treatment due to loss of Brønsted sites which are required for the isolated iron species to bind to the zeolite structure.

The chemical deactivation of Fe-BEA by phosphorous can be summarized into two steps where (i) shorter time of phosphorous exposure results in formation of mainly phosphorous pentoxides (P_2O_5) which do not significantly affect the NO_X reduction, and (ii) longer time of phosphorous exposure results in a significant increase of the relative amount of metaphosphates which decrease the NO_X reduction by replacing the hydroxyl groups on the active isolated iron species.

Furthermore, exposure to potassium results in deactivation of Fe-BEA due to exchange and loss of active isolated iron species in the zeolite forming smaller iron clusters inside the zeolite pores.

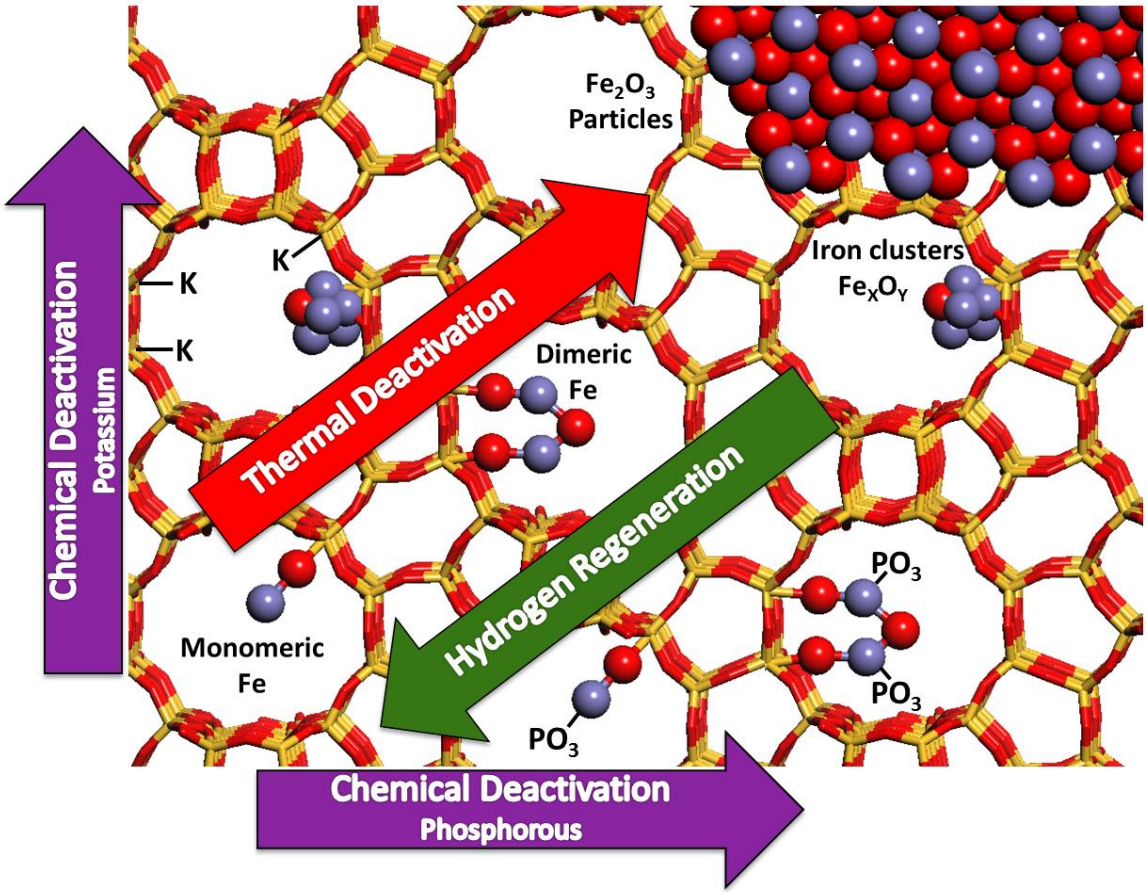

Figure 9.5. Schematic description of the mechanisms for hydrothermal and chemical deactivation, and hydrogen regeneration for iron-exchanged zeolite BEA.

To develop a kinetic model for simulating deactivation of Fe-BEA for NH_3-SCR applications, it is crucial to define the activity of the iron species in the catalyst. Based on a broad range of experimental results, which were discussed in the previous sections, a multi-site model is suggested. It is important for the model to include all iron species observed in the experimental measurements. Monomeric and dimeric iron species are included to catalyze the NH_3-SCR and NH_3-oxidation reactions and larger iron particles to facilitate NO oxidation. Brønsted sites in the zeolite are included to act as the main storage site for ammonia. Furthermore, we would like to emphasize the importance of high surface coverage of ammonia which could be observed in the ammonia inhibition experiment. There is a strong inhibiting effect by NH_3 during low-temperature NH_3-SCR for fresh and deactivated Fe-BEA. An ammonia spillover mechanism between the monomeric iron and Brønsted acid sites is therefore crucial to include in the model to predict the NO_X conversion during transient conditions. However, we would like to highlight that we do not conclude that ammonia spillover between other sites does not exist. A schematic figure is presented in Figure 9.6 for the proposed multi-site model of Fe-BEA as NH_3-SCR catalyst which shows the different iron species, the Brønsted acid sites and their main functions.

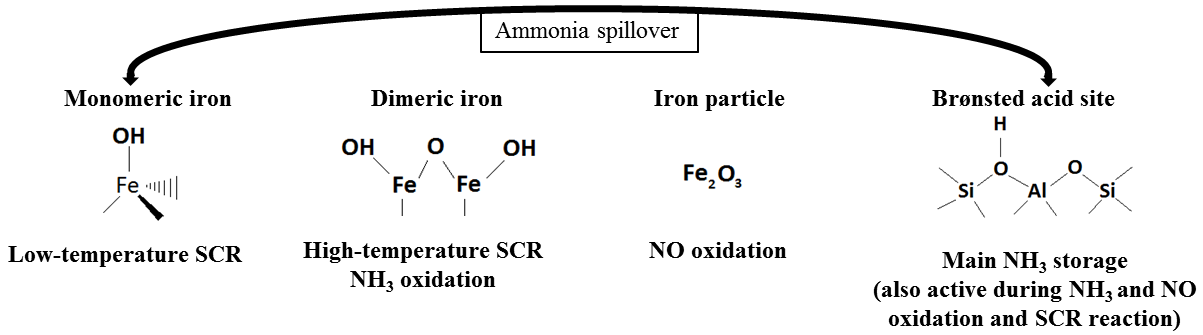

Figure 9.6. *Proposed multi-site model for Fe-BEA as NH_3-SCR catalyst.*

10 Kinetic deactivation model

A kinetic model is developed for H-BEA and Fe-BEA as NH_3-SCR catalysts, with focus on the dynamics of the active sites before and after hydrothermal treatment in **Paper VIII**. The model is based on the results from a broad range of experiments. The model is developed using subsystems where the first subsystem describes the adsorption of ammonia and NO on the Brønsted and iron sites which was found to be crucial to describe transient changes. The second subsystem describes the oxidation of NH_3 and NO. The two subsystems are combined together with additional reactions that account for the NH_3-SCR reactions in the third subsystem. The subsystems are fitted separately and finally the model is validated using separate ammonia inhibiting experiments which were not included in the fitting process of the kinetic parameters. The kinetic parameters and the site densities are fitted to the experimental results for fresh H-BEA and Fe-BEA. To simulate the decreased activity for the hydrothermally treated samples the kinetic parameters are kept constant, while the site densities are changed to simulate the effect of ageing. However, the binding energy of ammonia to the Brønsted sites needed to be decreased for the hydrothermally treated samples to fit the shift in the corresponding desorption peak observed in the NH_3-TPD experiments. Furthermore, the developed deactivation model is validated using phosphorous exposed Fe-BEA in **Paper IX** and potassium exposed H-BEA and Fe-BEA in **Paper X**.

10.1 Reaction rates

10.1.1 NH_3 and NO adsorption and desorption (subsystem 1)

The model includes reaction steps for adsorption and desorption of ammonia on zeolite and iron sites. First the H-BEA catalyst is modeled using sites for weakly bound ammonia (denoted W) [122] and Brønsted acid sites (denoted $Z_{Br,1}$) for stronger bound species [7, 101, 123]. As observed in the experiments, NH_3 showed an inhibiting effect at lower temperatures for Fe-BEA and for this reason we assume that NH_3 only adsorbs on monomeric iron species to simplify the model. Furthermore, two ammonia molecules have been shown to adsorb on each monomeric iron species [104] and therefore the monomeric iron sites, Fe_M, are defined as two sites, $Fe_{M,1}$ and $Fe_{M,2}$, with equal site density, where each site can host one ammonia molecule. According to the literature the heat of adsorption for ammonia varies between about 75-180 kJ/mol for zeolites; about 180 kJ/mol for H-ZSM-5[95] and 75-120 kJ/mol for H-BEA [124] and Cu-BEA [124].

Furthermore, for H-ZSM-5 [123] and H-BEA [124] it has previously been shown that the heat of adsorption for NH_3 is coverage dependent, which also has been used in several kinetic models [95, 98, 125] to describe ammonia desorption. The present model includes such surface coverage dependent activation energy for all NH_3 adsorption sites according to the expression:

$$E_{a,i} = E_{a,i}(0)\left(1 - \alpha_{i,k}\theta_k\right) \tag{10.1}$$

To describe transient changes at lower temperatures where ammonia inhibition is observed, it was required to include NO adsorption and desorption steps in the model and an NH_3 spillover mechanism. Small amounts of NO are assumed to adsorb on the Brønsted and monomeric iron sites. NO is set to adsorb on the Brønsted acid sites denoted $Z_{Br,2}$, where $Z_{Br,2}$ represents a small fraction of the main Brønsted sites $Z_{Br,1}$. For the Fe-BEA catalyst NO is adsorbed on one of the monomeric iron sites $Fe_{M,2}$. A spillover mechanism is included for the H-BEA and Fe-BEA model, which previously has been included for iron-exchanged zeolites by Nova et al. [126]. Ammonia is assumed to spillover from the main zeolite storage sites ($Z_{Br,1}$) to one of the monomeric iron sites ($Fe_{M,1}$). The thermodynamics for gas phase equilibrium reactions must be fulfilled thus thermodynamic constrains are taken into consideration for the spillover mechanism [127]. The equilibrium constant K_{eq} for the spillover

mechanism is obtained from the standard state Gibbs free energy of formation as shown previously (c.f. 6.2.1).

The reaction steps that are included in the first subsystem are summarized below (10.2-10.9).

$$NH_3 + W \Leftrightarrow NH_3 - W \quad (10.2)$$

$$NH_3 + Z_{Br,1} \Leftrightarrow NH_3 - Z_{Br,1} \quad (10.3)$$

$$NH_3 + Z_{Br,2} \Leftrightarrow NH_3 - Z_{Br,2} \quad (10.4)$$

$$NH_3 + Fe_{M,1} \Leftrightarrow NH_3 - Fe_{M,1} \quad (10.5)$$

$$NH_3 + Fe_{M,2} \Leftrightarrow NH_3 - Fe_{M,2} \quad (10.6)$$

$$NH_3 - Z_{Br,1} + Fe_{M,1} \Leftrightarrow Z_{Br,1} + NH_3 - Fe_{M,1} \quad (10.7)$$

$$NO + Z_{Br,2} \Leftrightarrow NO - Z_{Br,2} \quad (10.8)$$

$$NO + Fe_{M,2} \Leftrightarrow NO - Fe_{M,2} \quad (10.9)$$

10.1.2 NH_3 and NO oxidation (subsystem 2)

During NH_3 and NO oxidation no transient effects could be observed under the present experimental conditions. Therefore the oxidation steps are modeled as gas phase reactions. In order to simplify the model we used gas phase concentrations, but we would like to emphasize that this does not mean that these reactions do not proceed between adsorbed species, it is only a simplification for a global kinetic step.

For the H-BEA model, ammonia oxidation is set to take place over $Z_{Br,2}$ sites and for the Fe-BEA model the ammonia oxidation proceeds over dimeric iron sites (denoted Fe_D).

Devadas et al. [72] showed that Fe_2O_3 particles are not active in the SCR reaction but in the oxidation of NO. Therefore NO-oxidation is modeled as a gas phase reaction over Fe_2O_3 particles (denoted Fe_P). For the H-BEA catalyst minor oxidation of NO was observed and thus a similar gas phase reaction is added over the active Brønsted site, $Z_{Br,2}$, in the zeolite. The reaction steps that are included in the second subsystem are summarized below (10.10-10.13).

$$4\,NH_3 + 3\,O_2 \xrightarrow{Z_{B,2}} 2\,N_2 + 6\,H_2O \quad (10.10)$$

$$4\,NH_3 + 3\,O_2 \xrightarrow{Fe_D} 2\,N_2 + 6\,H_2O \quad (10.11)$$

$$2\,NO + O_2 \xleftrightarrow{Z_{B,2}} 2\,NO_2 \quad (10.12)$$

$$2\,NO + O_2 \xleftrightarrow{Fe_P} 2\,NO_2 \quad (10.13)$$

10.1.3 NH_3-SCR

The two previous subsystems are combined together with three additional reactions that account for the NO reduction during NH_3-SCR. The objective of the kinetic model is to further understand the dynamics of the active sites, particularly after thermal and chemical deactivation. Therefore, the role of NO_2 during NH_3-SCR has not been investigated in this study, and NO oxidation is not included in the SCR simulations. For the H-BEA model the standard SCR reaction is modeled to proceed between adsorbed NO and NH_3 species on Brønsted sites, $Z_{Br,2}$ and $Z_{Br,1}$, respectively. For Fe-BEA we assume that the NH_3-SCR reaction is mainly catalyzed by two different active sites with different activation energies, where at lower temperatures (150-300^{0}C), monomeric iron species are the governing sites for

the SCR reaction and at higher temperatures (400-500^{0}C) the reaction is assumed to proceed primarily over dimeric iron species. Therefore, two parallel reactions were included; (i) low-temperature standard SCR between adsorbed NO and NH_3 on monomeric iron species, $Fe_{M,2}$ and $Fe_{M,1}$, respectively, and (ii) high-temperature SCR over dimeric iron species, Fe_D. A high-temperature SCR step over Fe-zeolites has previously been included by Sjövall et al. [37]. The NO conversion at higher temperatures is relatively fast, indicating direct reaction between NO and NH_3 when adsorbed on the dimeric sites. Therefore the second SCR reaction is modeled as a gas phase reaction over the dimeric iron sites, however, it should be emphasized again that this does not mean that the reaction does not proceed between adsorbed species, but only a simplified global kinetic step. The activation energies for the two SCR reactions over Fe-BEA are fixed according to the experimentally found values presented by Brandenberger et al. [65]. The SCR reaction steps are summarized below (10.14-10.16).

$$4\,NH_3 - Z_{Br,1} + 4\,NO - Z_{Br,2} + O_2 \Rightarrow 4\,N_2 + 6\,H_2O + 4\,Z_{Br,1} + 4\,Z_{Br,2} \quad (10.14)$$

$$4\,NH_3 - Fe_{M,1} + 4\,NO - Fe_{M,2} + O_2 \Rightarrow 4\,N_2 + 6\,H_2O + 4\,Fe_{M,1} + 4\,Fe_{M,2} \quad (10.15)$$

$$4\,NH_3 + 4\,NO + O_2 \overset{Fe_D}{\Longrightarrow} 4\,N_2 + 6\,H_2O \quad (10.16)$$

10.2 Results

10.2.1 NH_3 and NO storage and oxidation

The kinetic parameters from the fresh H-BEA model were kept constant for the simulation of the aged H-BEA samples except for the decreased binding energy of ammonia on the Brønsted sites, $Z_{Br,1}$, due to the hydrothermal treatment, which is shown in Table 10.1. By decreasing the site density for weakly bound ammonia, W, and the main Brønsted sites, $Z_{Br,1}$, the simulated ammonia concentration in the outlet feed follows the NH_3-TPD experiments well. The hydrothermally treated Fe-BEA samples show the same experimental trend with ageing time as for the H-BEA samples. However, no difference in loosely bound ammonia between the aged and fresh Fe-BEA samples could be seen. The decrease in desorption energy of ammonia over the Brønsted sites agrees well with our study in **Paper II**, where it was shown that the stronger Brønsted sites are more sensitive to hydrothermal treatment compared to the weaker sites, resulting in a decreased mean desorption energy for ammonia, as shown in Table 10.1. The NO adsorption and desorption simulations were fitted from NO-TPD experiments. Due to relatively low adsorption in presence of water, the NO-TPD experiments were performed in absence of water. The simulations explained the NO adsorption well for both the fresh H-BEA and Fe-BEA samples as well as for the hydrothermally treated samples by decreasing the site density of $Z_{Br,2}$ for the H-BEA model and of $Fe_{M,2}$ for the Fe-BEA model.

Table 10.1. *Site density normalized towards fresh sample and desorption energy of NH_3 from Brønsted sites for all hydrothermally treated samples used in* ***Paper VIII****.*

Sample	HT treatment	W (x 10^{-5})	$Z_{Br,1}$ (x 10^{-5})	$Z_{Br,2}$ (x 10^{-5})	$Fe_{M,1\ or\ 2}$ (x 10^{-5})	Fe_D (x 10^{-5})	Fe_P (x 10^{-5})	Act. Energy E_a (kJ/mol)[a]
Fe - BEA	fresh	1	1	1	1	1	1	77.7
Fe - BEA	3h – 700^{0}C	1	0.63	0.80	0.72	0.42	1.1	77.6
Fe - BEA	24h – 700^{0}C	1	0.58	0.80	0.47	0.13	0.80	77.3
H - BEA	fresh	1	1	1	-	-	-	79.6
H - BEA	24h – 600^{0}C	0.86	0.54	0.80	-	-	-	77.3

[a] – Desorption energy of NH_3 from Brønsted acid sites ($Z_{Br,1}$)

Furthermore, the ammonia oxidation experiments were well predicted by the model by decreasing the density of the active sites for the aged samples. However, for the NO oxidation a different trend compared to the ammonia oxidation was seen. As previously discussed (c.f. 8.2.1), the NO oxidation increased with ageing for the Fe-BEA samples. Therefore, the density of the iron particles had to be increased for the aged samples to fit the experiments well. The simulations predicted the NO oxidation well for the aged samples by first increase the site density and then, after reaching a maximum in activity, decrease the site density which agrees well with the trend in the DRIFTS measurements from **Paper III**.

10.2.2 NH_3-SCR

Figure 10.1 shows the effect of hydrothermal treatment on the SCR activity for the samples used for the ageing simulations. As previously mentioned, at lower reaction temperatures (up to 300^0C) the SCR reaction over Fe-BEA was observed to be more affected by ageing compared to higher temperatures (400-500^0C), while H-BEA showed a constant decrease in activity with ageing over the entire temperature range.

Figure 10.2 shows the simulated and experimental outlet concentrations of NO and NH_3 for the fresh Fe-BEA catalyst during NH_3-SCR together with the calculated mean coverage of NO on $Fe_{M,2}$ sites and NH_3 on $Z_{Br,1}$, $Fe_{M,1}$ and $Fe_{M,2}$ sites. During the SCR experiment the reaction parameters for the NH_3-SCR reaction steps are fitted. The model predicts the experiments well, where the monomeric iron species are the governing species at temperatures up to 300^0C, while between 400 and 500^0C the NO_X reduction cannot be predicted over monomeric iron species alone, hence the dimeric iron species compensate for NH_3-SCR at that temperature region.

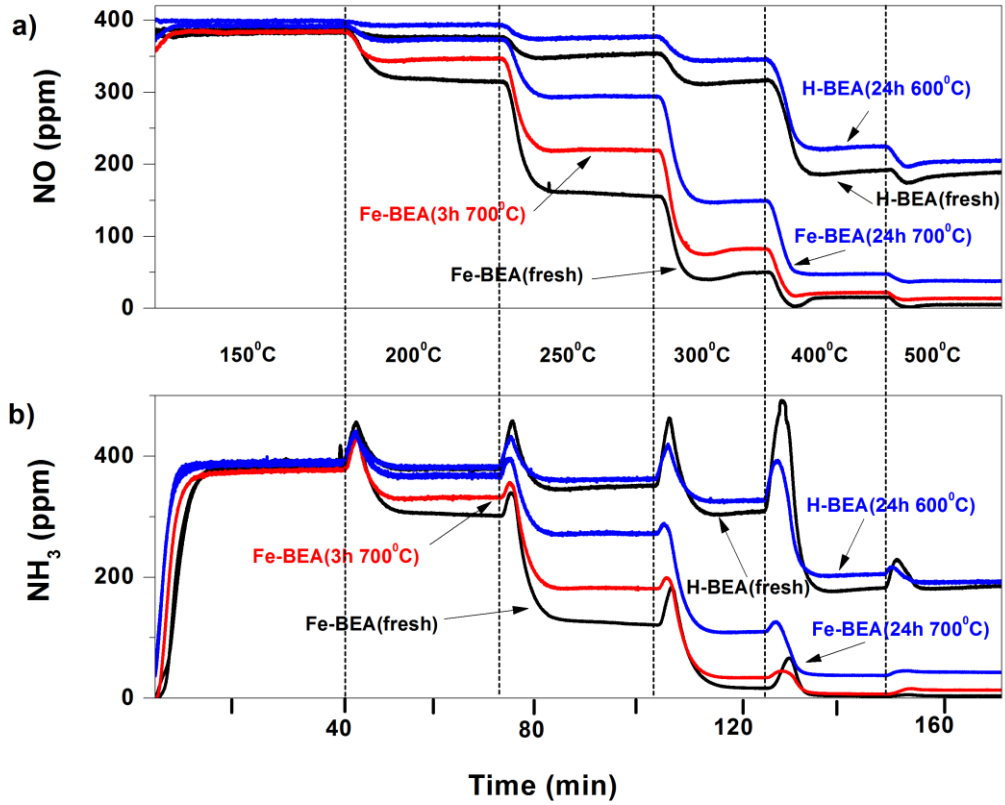

Figure 10.1. *Evolution of* ***(a)*** *NO and* ***(b)*** *NH_3 concentrations during NH_3-SCR over H-BEA catalyst aged at 600^0C for 24 h and Fe-BEA catalysts aged at 700^oC for 3 and 24 h compared to fresh samples. The samples were exposed to 400 ppm NO, 400 ppm NH_3, 8 % O_2 and 5 % H_2O and the temperature was stepwise increased from 150 to 500^0C. The total flow rate was 3500 ml/min.*

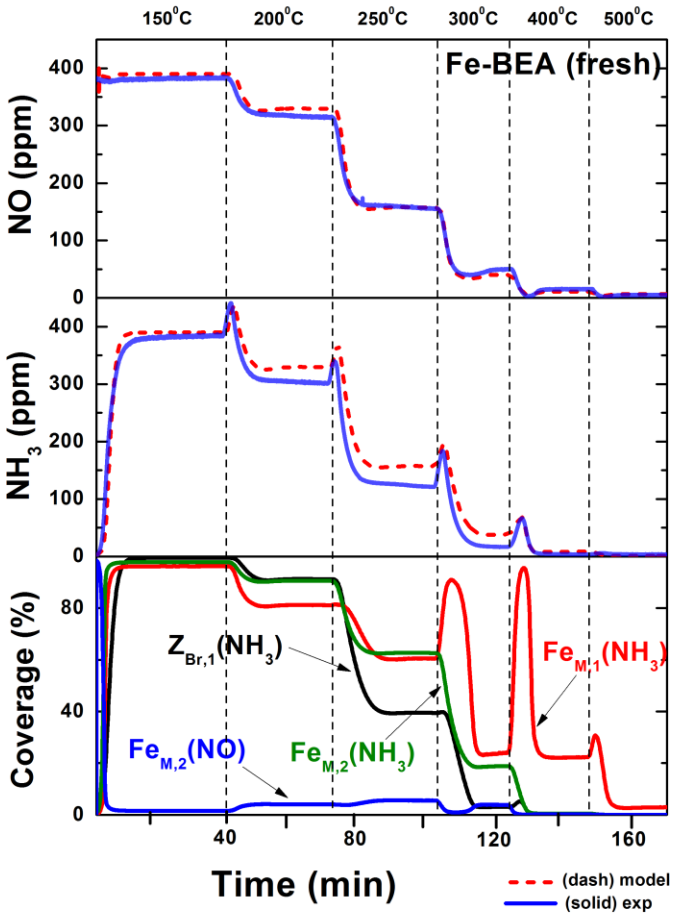

Figure 10.2 . *Measured and calculated outlet NO and NH_3 concentrations during NH_3-SCR with surface coverage of NO and NH_3 over $Z_{Br,1}$, $Fe_{M,1}$ and $Fe_{M,2}$ sites for fresh Fe-BEA. Upper and middle panel: The red dashed line shows the calculated concentration and the solid blue line shows the measured concentration. Lower panel: The black solid line represents NH_3 on Brønsted sites, $Z_{Br,1}$. The red and green solid line represents NH_3 on monomeric iron sites, $Fe_{M,1}$ and $Fe_{M,2}$, respectively. The blue solid line shows the coverage of NO on monomeric iron sites, $Fe_{M,2}$.*

The spillover effect is also observed in Figure 10.2 where the adsorbed ammonia on the Brønsted sites, $Z_{Br,1}$, starts to desorb during the temperature ramp, buffering the monomeric iron sites, $Fe_{M,1}$, with ammonia and hence temporarily increased surface coverage of ammonia adsorbed over active iron sites for NH_3-SCR.

Furthermore, Figure 10.3, shows the simulated and experimental outlet concentrations of NO and NH_3 for the aged Fe-BEA catalysts (Fe-BEA aged at 700^0C for 3 and 24 h) during NH_3-SCR together with the mean coverage of NO on $Fe_{M,2}$ sites and NH_3 on $Z_{Br,1}$, $Fe_{M,1}$ and $Fe_{M,2}$ sites. Furthermore, an overconsumption of ammonia can be observed, which previously has been observed by Sjövall et al. [37]. The molar stoichiometry between NO and NH_3 during SCR is 1:1 in the present model, while Sjövall et al. [37] compensated the overconsumption of ammonia by changing the stoichiometry of the SCR reaction. Furthermore, Nedyalkova et al. [128] showed, using isotopic labeled experiments, that this overconsumption is due to so-called parasitic NH_3 oxidation. However, to keep the model simple, we choose to keep the stoichiometry at 1:1. To simulate the deactivated samples, the fitted kinetic parameters from the fresh sample are kept constant and only the site densities are changed to simulate ageing. The decreased density of the dimeric iron sites is fitted together with the NH_3-oxidation experiments while the decreased density of the monomeric iron sites is calculated from the NO-TPD experiments together with the SCR experiments.

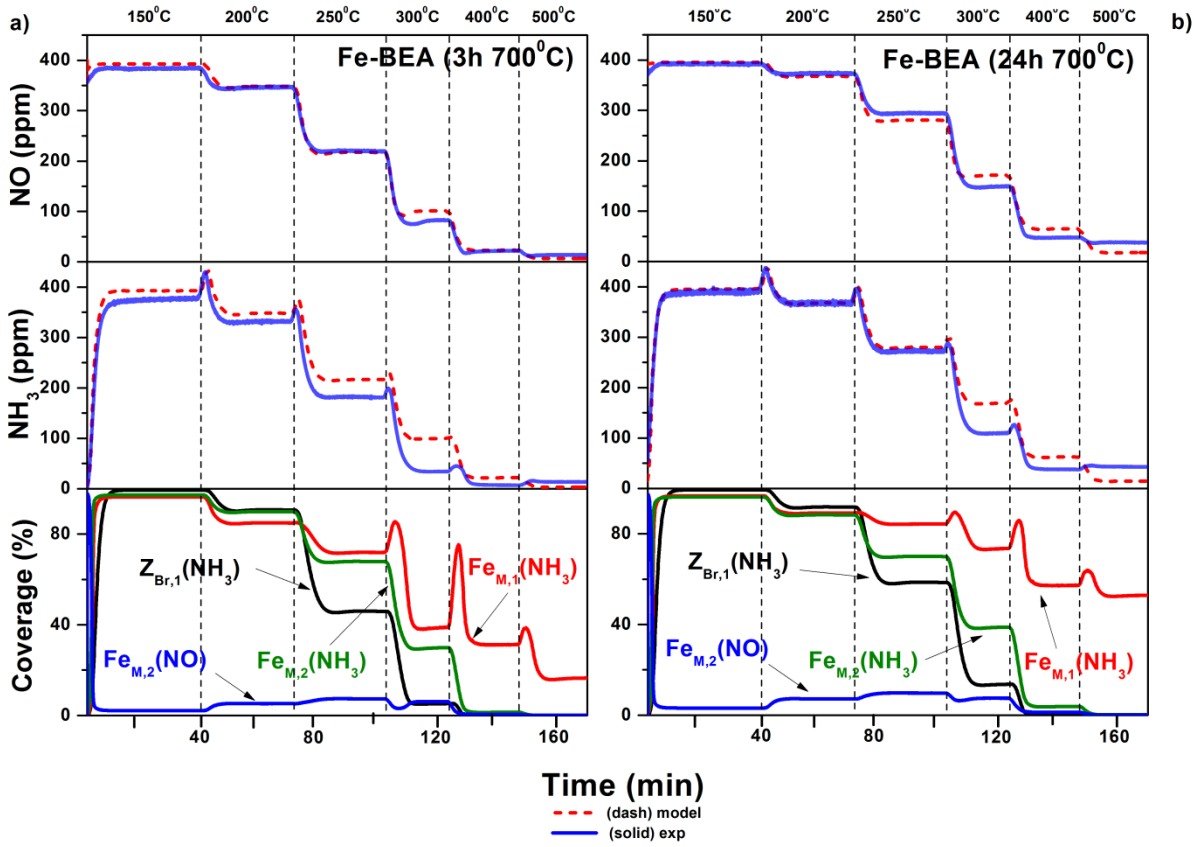

Figure 10.3. *The measured and calculated outlet NO and NH_3 concentrations during NH_3-SCR with surface coverages of NO and NH_3 over $Z_{Br,1}$, $Fe_{M,1}$ and $Fe_{M,2}$ sites for Fe-BEA aged at* ***(a)*** *700^0C for 3h and* ***(b)*** *at 700^0C for 24 h. Upper and middle panel: The red dashed line shows the calculated concentration and the solid blue line shows the measured concentration. Lower panel: The black solid line represents NH_3 on Brønsted sites, $Z_{Br,1}$. The red and green solid line represents NH_3 on monomeric iron sites, $Fe_{M,1}$ and $Fe_{M,2}$, respectively. The blue solid line shows the coverage of NO on monomeric iron sites, $Fe_{M,2}$.*

The decrease site density for the dimeric iron sites was found to be more pronounced compared to the decreased concentration of monomeric iron sites, indicating that the dimeric sites are more sensitive towards hydrothermal treatment than the monomeric iron sites.

It was further found that the spillover rate has to be independent of the site density of the involved species and only dependent on the fraction of free sites for the aged samples. This result indicates that the number of Brønsted sites buffering each iron site is unaffected by the hydrothermal treatment. If the reaction rate is dependent on the number of sites ($Z_{Br,1}$ and $Fe_{M,1}$, c.f. eq. 10.7) the spillover rate will be too low due to decreased site density and the consequence will be a deficit in ammonia available for the SCR reaction which in turn will result in lower NO_X conversion. The simulations of the aged H-BEA samples also agree well with the experiments by keeping the fitted kinetic parameters from the fresh H-BEA model constant and only decreasing the density of the active Brønsted site, $Z_{Br,2}$, for the aged H-BEA sample. Table 10.1 summarizes the changes in site density and desorption energy of ammonia due to hydrothermal treatment for the H-BEA and Fe-BEA model.

10.2.3 Ammonia inhibition

The developed ageing model was tested with independent ammonia inhibition experiments from **Paper II** which were not included in the parameter fitting process. Figure 10.4 shows the experimental measured and simulated outlet concentrations of NO and produced NO_2 during SCR at 250°C. Due to

the observed NO_2 production, the NO-oxidation mechanism was included in the reaction just after NH_3 cut-off to validate the steady state level of NO and the amount NO_2 produced.

It can be observed in Figure 10.4 that the calculated period with increased NO_X reduction after ammonia cut-off is slightly shorter compared to the experiments, indicating a deficit of total amount of ammonia buffering the active iron sites. The model only takes into account spillover from the main Brønsted site, $Z_{Br,1}$, to the monomeric iron site, $Fe_{M,1}$, while more than 50 % of the amount of ammonia is assumed to adsorb on the weak adsorption sites, W, which are not involved in the spillover in this model. Thus, this could explain the deficit of ammonia spillover to the monomeric iron sites. If the amount stored ammonia is increased by 50%, by increasing the site density of the main Brønsted sites, $Z_{Br,1}$, the increased NO_X reduction period fits well with the experiment, marked as the solid red line in Figure 10.4. It can be further observed that the increase in ammonia storage does not affect the steady state reduction of NO_X. This agrees well with other studies [7, 101], indicating that high density of Brønsted acid sites to achieve high activity for the NH_3-SCR reaction is not needed.

The model predicts the activity over the fresh samples well and the same trend can be observed for the aged samples, where it was required to increase the density of the Brønsted sites, $Z_{Br,1}$, by 50% to predict the increased NO_X reduction well.

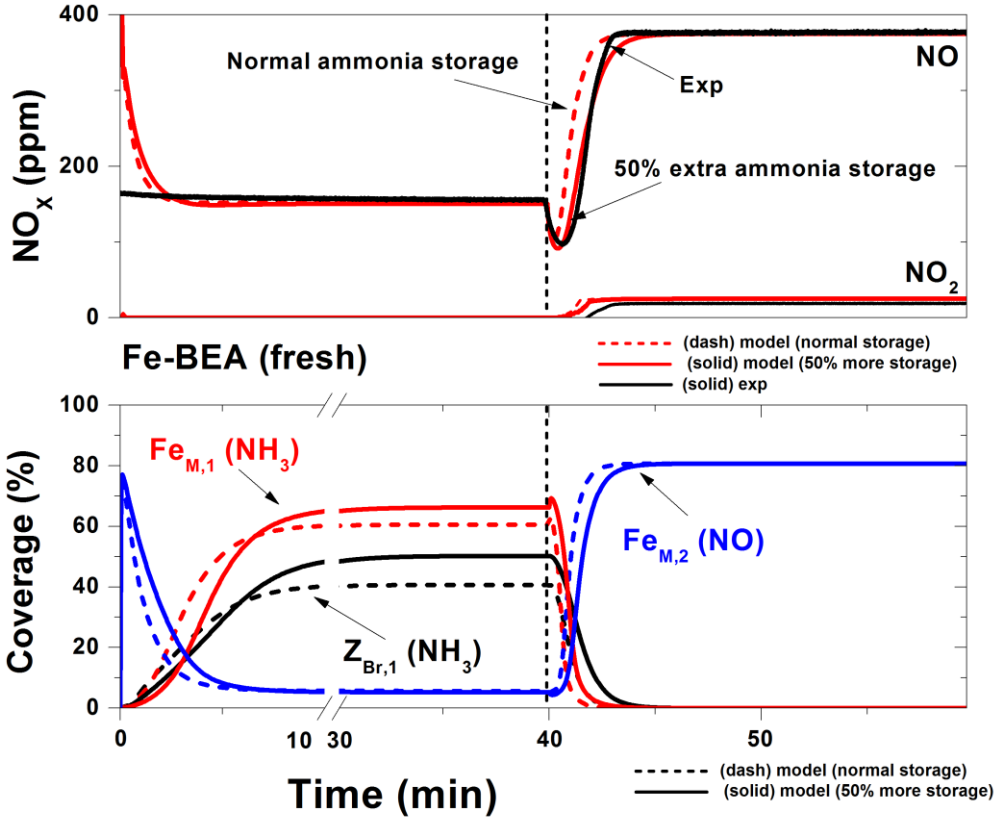

Figure 10.4. M*easured and calculated outlet NO and NO_2 concentrations during NH_3-SCR with surface coverages of NO and NH_3 over, $Z_{Br,1}$, $Fe_{M,1}$ and $Fe_{M,2}$ sites for fresh Fe-BEA. Upper panel: The red line shows the calculated concentration and the black line shows the measured concentration. Lower panel: The black line represents NH_3 over Brønsted sites, $Z_{Br,1}$. The red line represents NH_3 while the blue line represents NO over monomeric iron sites, $Fe_{M,1}$ and $Fe_{M,2}$, respectively. The dashed line represents the calculated results with normal ammonia storage, and the solid line represents the calculated results with increased ammonia storage.*

Figure 10.5 shows the NO_X conversion for all fresh and aged samples with 50 % increase in ammonia storage capacity to fit the inhibition experiments well. Furthermore, it has previously been shown that the adsorption of ammonia over H-BEA can be described by a distribution of 16 adsorption sites [103] where the binding energy varies from 50 to 325 kJ/mol. If the model would have included stronger acid sites for NH_3 adsorption, releasing ammonia slower, the deficit in the amount ammonia participating in the SCR reaction could have been compensated further. However, the present model is simplified to include only one type of Brønsted site (Z_{Br}) responsible for desorption of ammonia from the strong Brønsted acid sites. The model describes the dynamics of the adsorbed species well after the ammonia cut-off, when the amount of stored ammonia is increased. Furthermore, after ageing it was noted that the rate of NH_3 spillover between the main Brønsted sites and the monomeric iron sites, needs to be kept unchanged, and therefore the spillover rate has to be independent of the site density of the involved species and only dependent on the fraction of free sites. This indicates that the amount of Brønsted sites buffering the iron sites is unaffected by the hydrothermal treatment.

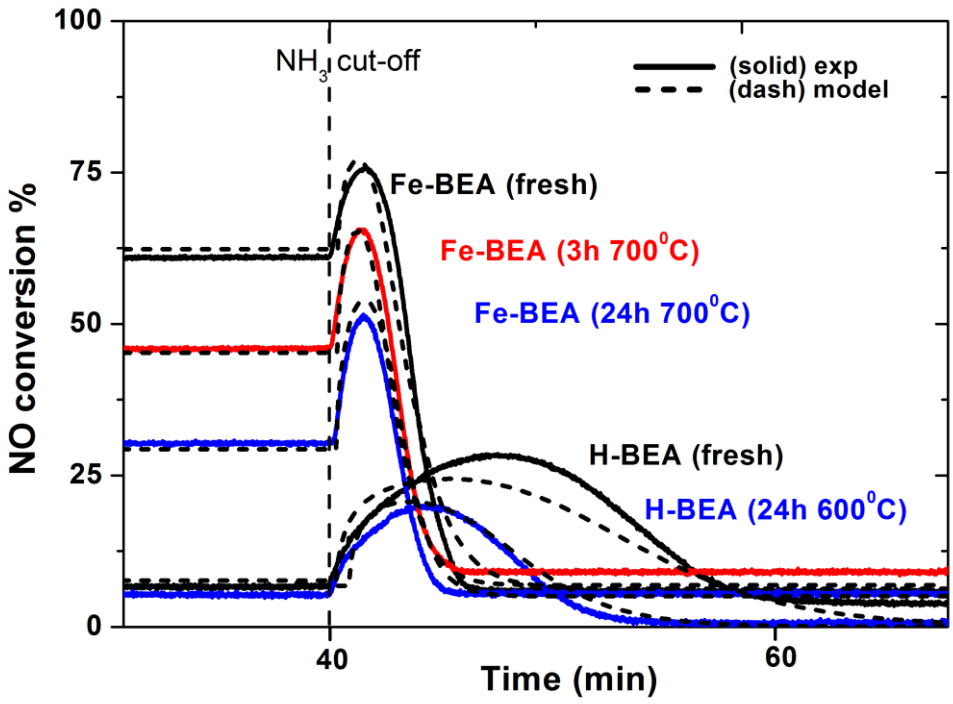

Figure 10.5 *Validation simulation showing the measured and calculated NO conversion during NH_3-SCR for fresh and aged H-BEA and Fe-BEA, with 50 % increased storage capacity of ammonia.*

10.3 Comparison and validation to chemically deactivated Fe-BEA

The kinetic model developed based on hydrothermally treated H-BEA and Fe-BEA was validated using phosphorous and potassium exposed samples. The chemical deactivation mechanism includes loss of active sites similar to the hydrothermally treated samples. However, even though the chemical deactivation mechanisms are different, the same kinetic model can be applied. If the active site is chemically deactivated the consequences will be the same. The site density decreases due to chemical impurities blocking the active site, while the site density decreases due to loss of active sites for hydrothermally treated samples.

To simulate chemical deactivation due to phosphorous or potassium exposure, the kinetic parameters are kept constant but the site density is decreased to simulate deactivation, similar to the simulation of hydrothermally treated samples. The model is able to predict and simulate the decreased NO_X reduction due to phosphorous or potassium exposure during steady state conditions as well as during transient conditions. Furthermore, similar to the hydrothermally treated samples, it was found that the decrease in the number of monomeric sites in the model is the single most crucial factor for the decreased NO_X reduction, hence a comparison between the three different deactivation treatments is shown in Figure 10.6. The decrease in the number of monomeric iron sites for the deactivated samples is compared after normalization to the number of monomeric iron sites in the corresponding fresh sample. It presents that the hydrothermal treatment at 700^{o}C for 3 h is comparable to chemical deactivation using 50 ppm potassium exposure for 48 h, showing that the hydrothermal treatment is more severe compared to the chemical deactivation, with respect to the monomeric iron sites.

The results in Figure 10.6 show that the chemical deactivation is less severe than the hydrothermal deactivation with respect to monomeric iron sites of the NO_X reduction performance. However, due to a continuous exposure of impurities in the exhaust gas of commercial engines, the chemical deactivation may be more significant after longer time of exposure compared to hydrothermal deactivation.

Furthermore, by simulating deactivation by only decreasing the number of active sites indicates that there is the possibility to define deactivation rate expressions for the active sites. By making a systematic study of different deactivation mechanisms one might define a deactivation rate for the active site as a function of concentration of poison, flow, temperature, time etc. Finding and designing deactivation rates in this way is of great interest for optimizing operation conditions and especially for sizing the catalyst for the lifetime of the vehicle due to performance loss over time for the NH_3-SCR catalyst. However, it should be noted that different compounds may interact forming other types of species, e.g. potassium phosphates or particulates [79, 129] which might affect the deactivation rate more or less severely that might need to be taken into consideration to describe the deactivation rate.

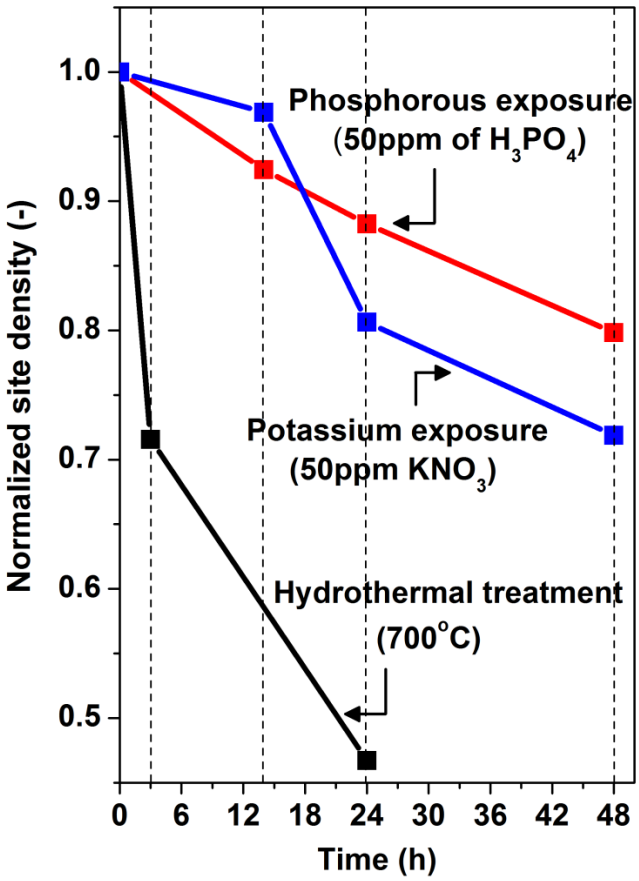

Figure 10.6. Change in site density of monomeric iron after hydrothermal treatment of **1 wt. % Fe-BEA** (at 700°C for 3 and 24 h) compared to chemically deactivated **1 wt. % Fe-BEA** due to phosphorous and potassium exposure using 50 ppm of H_3PO_4 or KNO_3 for 14, 24 and 48 h. The site densities are normalized to the corresponding site density of monomeric iron for the fresh Fe-BEA sample.

11 Low-temperature solid-state ion-exchange of copper

Copper-exchanged zeolites are an alternative to iron-exchanged zeolites for NH_3-SCR applications. As previously discussed, zeolite exchanged with copper have a higher low-temperature activity compared to iron-exchanged zeolites under standard SCR conditions. In **Paper XII**, the preparation of highly active copper-exchanged zeolites has been studied. The conventional method to introduce copper into the zeolite is by aqueous ion-exchange with Cu^{2+} ions or by high-temperature solid state ion-exchange (SSIE) using a metal salt or oxide [58]. However, there are several drawbacks with these two methods. Aqueous ion-exchange requires that the procedure is repeated several times and the method is also sensitive to the zeolite structure. Aqueous ion-exchange is difficult to use for zeolites with CHA structure due to its polar framework [130]. Furthermore, high-temperature solid-state ion-exchange requires relatively high temperatures for the metal ions to diffuse into the zeolite, which restricts the method to only thermally stable zeolites.

Dry powder mixtures of $Cu^{II}O$ and zeolites with MFI, *BEA and CHA framework structure were ion-exchanged by exposing the mixtures to well-defined gas atmospheres at constant temperature. It was found that copper migrates and exchanges into the zeolite under SCR conditions (NO, NH_3, O_2 and H_2O) already at 250°C. Figure 11.1, shows the SCR activity at 200°C, before and after treatment at 250°C in SCR atmosphere. The activity is measured continuously during the treatment at 250°C. It can be seen that the SCR activity continuously increases, indicating formation of active copper sites.

Copper exchange at 250°C in SCR atmosphere is a considerably lower temperature than any other reported temperature for SSIE using $Cu^{II}O$. This indicates that some of the components in the SCR atmosphere enhance the migration of copper significantly. By varying the gas composition during the exchange process it was found that by just using NH_3 in the feed during treatment at 250°C, the NO_X reduction reached 36 % (activity measured at 200°C) after 10 h. It was observed that by adding NO to the NH_3 feed ([NO + NH_3]-SSIE) improved the copper exchange significantly, reaching 53 % NO_X conversion (activity measured at 200°C) after 10 h treatment in NO and NH_3 at 250°C. [NO + NH_3]-SSIE was performed using copper mixtures of *BEA and CHA compared to conventionally aqueous ion-changed Cu-*BEA, shown in Table 11.1. It was further found that using Cu^{I}_2O as copper precursor improved the exchange significantly in presence of NH_3 only. This shows that when using $Cu^{II}O$ as copper precursor, the mobility of Cu is the result of the reduction of Cu^{II} to Cu^{I}, which is enhanced by the presence of NO, and formation of Cu^{I}-ammine complexes. The formation of Cu^{I} when using Cu^{II} was confirmed by in situ XRD measurements, showing that by exposing Cu^{II} to NO and NH_3, reduction to Cu^{I} occurred.

The results show that in presence of NH_3, copper becomes highly mobile at considerably lower temperatures ($T \leq 250$°C) than during conventional SSIE. This may be used to prepare highly active copper-exchanged zeolites with high copper loading by a relatively fast and simple method for a number of technical uses, e.g. NH_3-SCR applications.

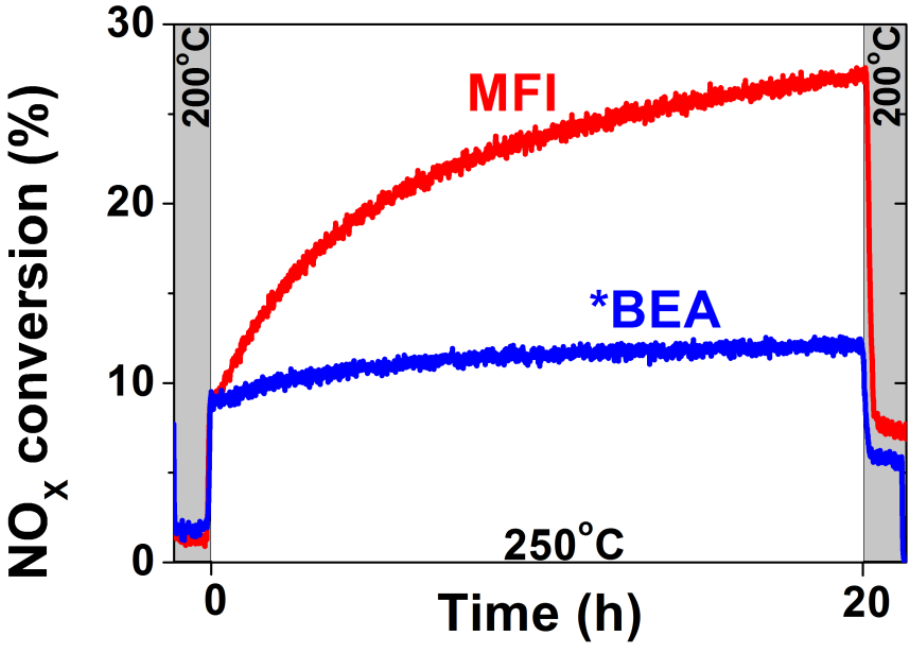

Figure 11.1. *Measured NH_3-SCR activity at 200°C of $Cu^{II}O$ + H-MFI or H-*BEA during 20 h treatment in SCR conditions at 250°C. NH_3-SCR conditions: 500 ppm NO, 530 ppm NH_3, 5 % H_2O, 10 % O_2 and N_2 as inert gas. The activity was continuously measured during the treatment at 250°C.*

Table 11.1. *Measured NH_3-SCR activity at 200°C of $Cu^{II}O$ + zeolite (*BEA, CHA and MFI) mixtures after treatment in NO (500 ppm) and NH_3 (530 ppm), and Cu^{I}_2O for MFI treated in 530 ppm NH_3 at 250°C for 5 and 10 h in comparison with aqueous ion-exchanged Cu-*BEA.*

Sample		X_{NOx} (%)	Reaction rate x 10^{-3} (mmol/s g $_{sample}$)
0.8 wt.% Cu-*BEA[a]		7.4	0.49
1.4 wt.% Cu-*BEA[a]		16	1.07
2.0 wt.% Cu-*BEA[a]		28	1.87
2.6 wt.% Cu-*BEA[a]		43	2.87
$Cu^{II}O$ + H-*BEA	Fresh	1.7	0.11
	5 h	49	3.27
	10h	50	3.34
$Cu^{II}O$ + H-CHA	Fresh	1.0	0.06
	5 h	45	3.00
	10 h	46	3.07
$Cu^{II}O$ + H-MFI	Fresh	1.6	0.11
	5 h	51	3.40
	10 h	53	3.53
Cu^{I}_2O + H-MFI (treated in NH_3 only)	Fresh	1.2	0.08
	5 h	59	3.94
	10 h	61	4.04

[a] Prepared by aqueous ion-exchange.

12 Ammonia formation in NO_X storage and reduction catalysts

In order to meet the upcoming NO_X and greenhouse gas emissions standards especially for light duty vehicles, combination of NSR and NH_3-SCR catalysts is a promising system for exhaust-gas aftertreatment [91, 131]. Combining NSR and SCR catalysts can enhance the NO_X reduction and at the same time decrease the loading of expensive PGMs in the NSR catalyst. Combining the two different systems, the *in situ* produced NH_3 by the NSR catalyst during the rich phase is captured by the SCR catalyst, where the SCR catalyst can enhance the overall NO_X reduction and decrease the NH_3 slip from the aftertreatment system. To implement a combined system in this way, further understanding of the ammonia formation mechanisms and zone design of the two catalysts is required. Lindholm et al. [91], showed that combining a Pt/Ba/Al with an Fe-BEA catalyst, resulted in superior NO_X removal efficiency and lower ammonia slip compared to the NSR catalyst alone. Furthermore, it was found by Pihl et al. [132] that the formation of NH_3 is favored when the concentration of H_2 is high, which agrees well with the results by Lindholm et al. [91] who showed that 99.5 % NO_X removal could be achieved at 300^{o}C when the H_2 concentration is relatively high in the combined NSR and SCR system.

A global kinetic model of an NSR catalyst was developed in **Paper XIII**, with focus on the formation and breakthrough of NH_3 during the rich phase. Intra-catalyst storage and reduction measurements (SpaciMS) were used to validate the model with respect to the formation of ammonia along the catalyst axis. The SpaciMS results show that most of the NO_X is stored in the first half of the catalyst. Furthermore, the experiments show that high amounts of ammonia also are produced in the first half of the catalyst, the so-called "buildup region", which further moves along the catalyst axis in a "plug flow" behavior. In the kinetic model, NH_3 formation is set to occur during the rich phase between stored NO_X and H_2. Furthermore, in order to predict the NH_3 breakthrough correct it was crucial to include formation of N_2O between stored NO_X and formed NH_3. Other mechanisms influencing the NH_3 formation and breakthrough were evaluated and tested. However, it was not necessary to include such mechanisms in order to predict the NH_3 formation well and therefore they were not included to keep the model as simple as possible. The model was able to predict the formation and breakthrough of NH_3 (and N_2O) well due to the above described mechanisms. Figure 12.1 shows the experimental and simulation results from long NSR cycles at 300^{o}C, where ammonia and nitrous oxide are marked. Furthermore, to confirm the ammonia formation **trend** in the model, the simulation was validated with SpaciMS measurements, shown in Figure 12.2. It can be noted in Figure 12.2 that the measurements have a progressive delay and a tailing edge. This is generally characteristic of the spatiotemporal nature, especially when measuring ammonia. Similar tailing edges are observed in Figure 12.1 as well, when measuring ammonia. Understanding and predicting formation of ammonia during the rich phase is of great interest when designing new catalysts and optimizing aftertreatment systems where NSR and SCR catalysts are combined. Recently, passive-ammonia or "urealess" SCR systems are developed where by cycling between lean and rich phase, ammonia is produced [133, 134]. However, in those systems a TWC catalyst is used instead of an NSR catalyst. Similar simulations performed for NSR catalysts may be implemented using TWC catalysts to optimize and improve the operation conditions for the aftertreatment system.

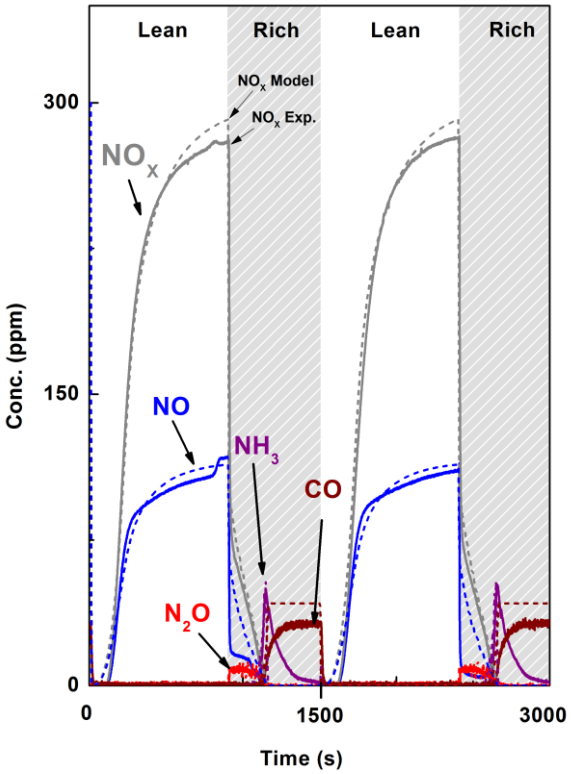

Figure 12.1. *Long NSR cycle performance. Measured (solid) and calculated (dashed) outlet NO_X, NO, N_2O, NH_3 and CO concentrations during NSR cycles at 300℃. NO_X desorption peak marked. The catalyst was exposed to 300 ppm NO, 10 % O_2, 5 % H_2O and 5 % CO_2 during the lean period (900 s) and to 375 ppm H_2, 625 ppm CO, 5 % H_2O and 5 % CO_2 during the rich period (600 s). The rich period is marked in gray.*

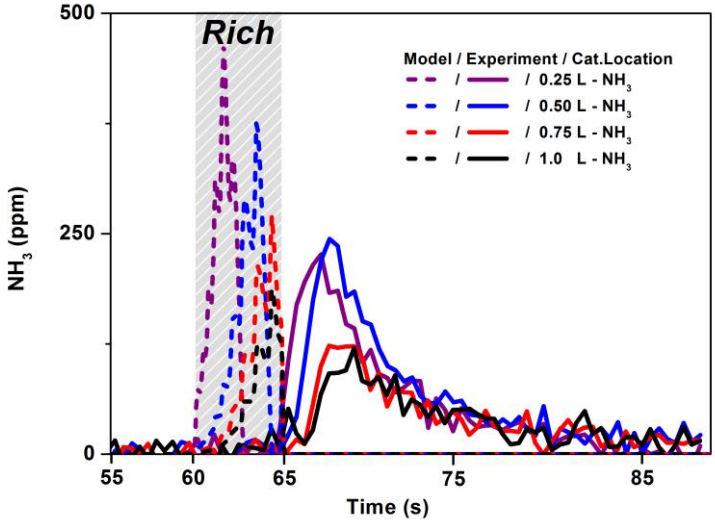

Figure 12.2*: Ammonia formation at different axial positions of the catalyst during one NSR cycle. Measured (solid) and calculated (dashed). The catalyst was exposed to 300 ppm NO, 10 % O_2, 5 % H_2O and 5 % CO_2 during the lean period (60 s) and to 2 % H_2, 5 % H_2O and 5 % CO_2 during the rich period (5 s) at 325^{0}C. The rich period is marked in gray. Note the magnification of the rich phase.*

13 Concluding discussion

The aim of this thesis is to gain deeper understanding on the active sites and deactivation of metal-exchanged zeolites for NH_3-SCR applications. The main focus is paid on thermal and chemical deactivation of iron-exchanged zeolites. This is accomplished by experimental studies and kinetic modeling with focus on the active iron species in the catalyst. Furthermore, the preparation of copper-exchanged zeolites is studied as well as the formation of ammonia from an NSR catalyst. The main conclusions from the different studies are summarized below.

Different deactivation mechanisms caused by hydrothermal treatment and chemical poisoning due to phosphorous and potassium exposure, and regeneration due to high-temperature hydrogen-treatment are identified. A multi-site kinetic model is developed and validated using the results from the experimental mechanistic studies of the deactivation mechanisms of Fe-BEA. The model is fitted to the kinetics of NH_3-SCR, NO and NH_3 oxidation, and NH_3 and NO storage for a fresh Fe-BEA catalyst. Deactivation is modelled by decreasing the number of active sites only and keeping all other kinetic parameters constant when simulating the decreased NO_X reduction. It is suggested that by performing a systematic study of different deactivation mechanisms due to hydrothermal treatment and chemical deactivation, a full deactivation model for iron-exchanged zeolite for NH_3-SCR application could be developed.

The hydrothermal deactivation of Fe-BEA is concluded to proceed in two steps; (i) formation of oligomeric iron clusters in the zeolite pores due to migration of isolated iron species after milder ageing, and (ii) continuous migration and formation of larger iron oxide particles located on the external surface of the zeolite crystals, resulting in a significant decrease in SCR activity after more severe ageing. Furthermore, the Brønsted sites in the zeolite are sensitive to hydrothermal treatment and therefore already after relatively mild ageing dealumination and loss of Brønsted sites occur in the zeolite. However, no strong correlation between high Brønsted acidity and SCR activity could be found. Additionally, the hydrothermally deactivated catalyst can be partially regenerated by high-temperature hydrogen exposure which results in a redispersion of the isolated iron species.

The chemical deactivation of Fe-BEA by phosphorous is concluded to proceed in two steps where (i) short time of phosphorous exposure results mainly in formation phosphorous pentoxides (P_2O_5) that do not significantly affect the NO_X reduction, while (ii) longer time of phosphorous exposure results in a significant increase of the relative amount of metaphosphates which decrease the SCR activity by replacing hydroxyl groups on the active isolated iron species with metaphosphates.

Furthermore, the chemical deactivation of Fe-BEA by potassium is concluded to be due to exchange and loss of active isolated iron species in the zeolite forming smaller iron clusters inside the zeolite pores.

The kinetic model is developed based on the fresh and hydrothermally treated samples and validated using the chemically deactivated samples. The model is a combination of three subsystems where the first subsystem describes the adsorption and desorption mechanisms of NO and NH_3. The second subsystem describes the oxidation of NO and NH_3 while the third subsystem accounts for the NH_3-SCR reactions. The subsystems are fitted separately and finally the model is validated using separate ammonia inhibition experiments which were not included in the fitting process of the kinetic parameters. Deactivation is simulated by decreasing the number of active sites in the model, while all other kinetic parameters are kept constant after fitted to a fresh sample; hence the deactivation is based only on the density of active sites.

The effect of atmosphere during solid-state ion-exchange of copper-zeolites was studied. It was found that highly active copper-exchanged zeolites for NH_3-SCR could be prepared by exposing physical mixtures of copper oxides with zeolites to NO and NH_3 at such low temperature as 250^{o}C. It is concluded that copper becomes highly mobile due to formation of copper-ammine complexes in

presence of NH_3 after reduction of Cu^{II} to Cu^{I} by adding NO in the exposing gas during the solid state ion-exchange.

Finally, the ammonia formation during the rich periods of NSR cycles was studied for the possibility of combining NSR and SCR catalysts. A global kinetic model of an NSR catalyst was developed with focus on the formation of ammonia and validated using intra-catalyst measurements. It is concluded that ammonia is formed from stored NO_X and hydrogen from the gas in the first half of the catalyst. However, to predict the ammonia formation well, N_2O formation from stored NO_X and NH_3 has to be included in the model.

Acknowledgments

This work has been performed within the FFI program, which is financially supported by the Swedish Energy Agency and partly within the Competence Centre for Catalysis (KCK), which is hosted by Chalmers University of Technology and financially supported by the Swedish Energy Agency and the member companies AB Volvo, ECAPS AB, Haldor Topsøe A/S, Scania CV AB, Volvo Car Corporation AB and Wärtsilä Finland Oy.

Professor Magnus Skoglundh, my examiner and main supervisor. Thank you for all your support and inspiration during my research. This work would not have been possible without your supervision, guidance and all the great discussions we had. It has been a great pleasure working with you! Thank you again for everything!

Professor Louise Olsson, my supervisor. Your constant support is always highly appreciated. Thank you for the interest you showed in my current and previous work and for always being available for discussions!

Dr. Jonas Jansson. It has been a pleasure discussing my work with you. Your advice, support and collaboration is highly appreciated.

Dr. Pär Gabrielsson. Thank you for giving me the opportunity to do research in your group and for the warm welcoming when I arrived.

Dr. Peter N.R. Vennestrøm and **Dr. Ton V.W. Janssens.** It was a pleasure working with you during those months! Thank you for your friendship, support and all the good times as well!!

Dr. Radka Nedyalkova and Dr. John Korsgren. I'm very grateful for all your help and advice in my research.

Dr. Miroslawa Milh, thank you for all your help and discussions we had during this project.

Prof. Henrik Grönbeck, Dr. Per-Anders Carlsson, Dr. Anders Hellman and Dr. Hanna Härelind. Thank you for your constant support and the stimulating discussions we have.

Thanks to my current and previous colleagues at **KCK** with special thanks for the ones I first meet when I started. You know who you are! Thank you for your friendship and all the great time we had during this time!

Our colleagues and friends at **TYK**, thank you all for creating a great atmosphere in the coffee room and during our leisure time.

My family and especially my **parents, brother and sister** for all their support during these years!

Last but not least, I would like to thank my wife, **Ghazaleh**, for all the encouragement and support during this time!

Nomenclature

A_i	Pre-exponential factor for reaction i. Depends on the rate expression
c_k	Mole fraction at the reaction layer of species k (-)
c_k^B	Mole fraction in the gas bulk of species k (-)
d_{hyd}	Hydraulic diameter of the channel (m)
$D_{k,g}$	Diffusion coefficient of species k in the gas bulk
$E_{a,i}$	Activation energy for reaction i (J/mol)
GSA	Geometric surface area per reactor volume (m^{-1})
ΔH	Enthalpy change (kJ/mol)
$k_{k,m}$	Mass transfer coefficient of species k (mol/ m^2 s)
K	Equilibrium constant (-)
k_i	Rate constant for reaction i. Depends on the rate expression
$MG_{k,g}$	Molar mass of gas phase species k (kg/kmol)
r_i	Reaction rate for reaction i (kmol/s $m^3_{wash\text{-}coat}$)
R	Gas constant (J/mol K)
ΔS	Entropy change (J/mol K)
Sh	Sherwood number (-)
W	Weak zeolite adsorption site
$Z_{Br,1}$	Brønsted zeolite site, 1
$Z_{Br,2}$	Brønsted zeolite site, 2
$Fe_{M,1}$	Monomeric iron site, 1
$Fe_{M,2}$	Monomeric iron site, 2
Fe_D	Dimeric iron site
Fe_P	Iron particle site
T_s	Temperature at catalyst surface (K)
t	Time (s)
$v_{k,i}$	Stoichiometric coefficient of species k in reaction i
v_g	Gas velocity (m/s)
$w_{k,g}$	Mass fraction of species k in gas phase (-)
z	Spatial coordinate in axial direction (m)

Greek letters

$\alpha_{k,i}$	Coverage dependence for species k in reaction i (-)
ε_g	Volume fraction of gas phase in entire system (-)
θ_k	Coverage of species k (-)
ρ_g	Density of the gas phase (kmol/ m^3)
Θ_j	Surface site density of storage site j (mol/ m^2)

References

[1] G.T. Miller, Living in the Enviroment - Principles, Connections and Solutions, 15th ed., 2007.
[2] R. Burch, Catal. Rev.-Sci. Eng. 46 (2004) 271-333.
[3] G.C. Bond, Hetrogeneous Catalysis: Principles and Applications, 2 ed., Claredon Press, Oxford, 1987.
[4] R.M. Heck, R.J. Farrauto, Catalytic Air Pollution Control: Commercial Technology, Can Nostrand Reinhold, New York, 1995.
[5] H. Sjövall, Selective Catalytic Reduction of NO_X with NH_3, Chemical and Biological Engineering, Chalmers University of Technology, Göteborg, Sweden, 2009.
[6] S.i. Matsumoto, CATTECH 4 (2000) 102-109.
[7] S. Brandenberger, O. Krocher, A. Tissler, R. Althoff, Catal. Rev.-Sci. Eng. 50 (2008) 492-531.
[8] P. Forzatti, L. Lietti, I. Nova, E. Tronconi, Catal. Today 151 (2010) 202-211.
[9] K. Kamasamudram, N.W. Currier, X. Chen, A. Yezerets, Catal. Today 151 (2010) 212-222.
[10] H. Sjövall, L. Olsson, E. Fridell, R.J. Blint, Applied Catalysis B: Environmental 64 (2006) 180-188.
[11] K. Rahkamaa-Tolonen, T. Maunula, M. Lomma, M. Huuhtanen, R.L. Keiski, Catal. Today 100 (2005) 217-222.
[12] S. Kieger, G. Delahay, B. Coq, B. Neveu, J. Catal. 183 (1999) 267-280.
[13] J.H. Park, H.J. Park, J.H. Baik, I.S. Nam, C.H. Shin, J.H. Lee, B.K. Cho, S.H. Oh, J. Catal. 240 (2006) 47-57.
[14] J.A. Sullivan, J. Cunningham, M.A. Morris, K. Keneavey, Appl. Catal. B-Environ. 7 (1995) 137-151.
[15] H. Sjövall, E. Fridell, R. Blint, L. Olsson, Top. Catal. 42-43 (2007) 113-117.
[16] A. Grossale, I. Nova, E. Tronconi, D. Chatterjee, M. Weibel, J. Catal. 256 (2008) 312-322.
[17] A. Grossale, I. Nova, E. Tronconi, Catal. Today 136 (2008) 18-27.
[18] O. Kröcher, M. Devadas, M. Elsener, A. Wokaun, N. Söger, M. Pfeifer, Y. Demel, L. Mussmann, Applied Catalysis B: Environmental 66 (2006) 208-216.
[19] A. Grossale, I. Nova, E. Tronconi, Catal. Lett. 130 (2009) 525-531.
[20] C.H. Bartholomew, Applied Catalysis A: General 212 (2001) 17-60.
[21] V. Kröger, Poisoning of Automotive Exhaust Gas Catalyst Components, Process and Enviromental Engineering, University of Oulu, Oulu, Finland, 2007.
[22] P. Kern, M. Klimczak, T. Heinzelmann, M. Lucas, P. Claus, Applied Catalysis B: Environmental 95 (2010) 48-56.
[23] L. Ma, J.H. Li, Y.S. Cheng, C.K. Lambert, L.X. Fu, Environ. Sci. Technol. 46 (2012) 1747-1754.

[24] J. Li, R. Zhu, Y. Cheng, C.K. Lambert, R.T. Yang, Environ. Sci. Technol. 44 (2010) 1799-1805.
[25] C. He, Y. Wang, Y. Cheng, C.K. Lambert, R.T. Yang, Applied Catalysis A: General 368 (2009) 121-126.
[26] M.A. Vannice, Kinetics of Catalytic Reactions, Springer, 2005.
[27] I. Chorkendorff, J.W. Niemantsverdriet, Concepts of Modern Catalysis and Kinetics, Wiley-VCH, Weinheim, 2003.
[28] R.K. Srivastava, W. Neuffer, D. Grano, S. Khan, J.E. Staudt, W. Jozewicz, Environmental Progress 24 (2005) 181-197.
[29] W. Held, A. Koenig, T. Richter, SAE Technical Paper 900496 (1990).
[30] M. Koebel, M. Elsener, M. Kleemann, Catal. Today 59 (2000) 335-345.
[31] A. Lundström, Urea Decomposition for Urea-SCR Applications, Chemical and Biological Engineering, Chalmers University of Technology, Gothenburg, Sweden, 2010.
[32] M. Devadas, O. Kröcher, M. Elsener, A. Wokaun, N. Söger, M. Pfeifer, Y. Demel, L. Mussmann, Applied Catalysis B: Environmental 67 (2006) 187-196.
[33] M. Koebel, M. Elsener, G. Madia, (2001).
[34] L. Lietti, G. Ramis, F. Berti, G. Toledo, D. Robba, G. Busca, P. Forzatti, Catal. Today 42 (1998) 101-116.
[35] S.J. Schmieg, J.-H. Lee, (2005).
[36] S.D. Yim, S.J. Kim, J.H. Baik, I.S. Nam, Y.S. Mok, J.H. Lee, B.K. Cho, S.H. Oh, Industrial & Engineering Chemistry Research 43 (2004) 4856-4863.
[37] H. Sjövall, R.J. Blint, A. Gopinath, L. Olsson, Industrial & Engineering Chemistry Research 49 (2010) 39-52.
[38] S. Ogunwumi, R. Fox, M.D. Patil, L. He, (2002).
[39] G. Tuenter, W.F. van Leeuwen, L. Snepvangers, Industrial & Engineering Chemistry Product Research and Development 25 (1986) 633-636.
[40] G. Centi, S. Perathoner, D. Biglino, E. Giamello, J. Catal. 152 (1995) 75-92.
[41] M. Mauvezin, G. Delahay, F. Kißlich, B. Coq, S. Kieger, Catal. Lett. 62 (1999) 41-44.
[42] M. Amblard, R. Burch, B.W.L. Southward, Catal. Lett. 68 (2000) 105-108.
[43] M.W. Kumthekar, U.S. Ozkan, Applied Catalysis A: General 151 (1997) 289-303.
[44] F.J.J.G. Janssen, F.M.G. Van den Kerkhof, H. Bosch, J.R.H. Ross, The Journal of Physical Chemistry 91 (1987) 6633-6638.
[45] B. Coq, M. Mauvezin, G. Delahay, J.-B. Butet, S. Kieger, Applied Catalysis B: Environmental 27 (2000) 193-198.
[46] J.A.Z. Pieterse, S. Booneveld, R.W. van den Brink, Applied Catalysis B: Environmental 51 (2004) 215-228.
[47] R. Moreno-Tost, J. Santamaría-González, E. Rodríguez-Castellón, A. Jiménez-López, M.A. Autié, E. González, M.C. Glacial, C.D.l. Pozas, Applied Catalysis B: Environmental 50 (2004) 279-288.

[48] F. Radtke, R. Köppel, A. Baiker, Catal. Today 26 (1995) 159-167.
[49] J.A. Dumesic, N.Y. Topsoe, H. Topsoe, Y. Chen, T. Slabiak, J. Catal. 163 (1996) 409-417.
[50] I.E. Wachs, G. Deo, B.M. Weckhuysen, A. Andreini, M.A. Vuurman, M. deBoer, M.D. Amiridis, J. Catal. 161 (1996) 211-221.
[51] M. Koebel, G. Madia, F. Raimondi, A. Wokaun, J. Catal. 209 (2002) 159-165.
[52] N.Y. Topsoe, H. Topsoe, J.A. Dumesic, J. Catal. 151 (1995) 226-240.
[53] W.E.J. van Kooten, B. Liang, H.C. Krijnsen, O.L. Oudshoorn, H.P.A. Calis, C.M. van den Bleek, Appl. Catal. B-Environ. 21 (1999) 203-213.
[54] M. Colombo, I. Nova, E. Tronconi, Catal. Today 151 (2010) 223-230.
[55] K. Kamasamudram, N.W. Currier, T. Szailer, A. Yezerets, SAE Int. J. Fuels Lubr. 3 (2010) 664-672.
[56] W.M. Meier, D.H. Olson, C. Baerlocher, Atlas of Zeolite Structure Types, Elsevier, London, 1996.
[57] A. Dyer, An introduction to zeolite molecular sieves, J. Wiley, 1988.
[58] P.N.R. Vennestrøm, A. Katerinopoulou, R.R. Tiruvalam, A. Kustov, P.G. Moses, P. Concepcion, A. Corma, ACS Catalysis 3 (2013) 2158-2161.
[59] H.V. Bekkum, Introduction to Zeolite Science and Practice, Elsevier, 2001.
[60] R.Q. Long, R.T. Yang, J. Catal. 194 (2000) 80-90.
[61] R.Q. Long, R.T. Yang, J. Catal. 207 (2002) 224-231.
[62] R.Q. Long, R.T. Yang, J. Catal. 207 (2002) 158-165.
[63] A. Ates, Appl. Catal. B-Environ. 76 (2007) 282-290.
[64] H.-Y. Chen, W.M.H. Sachtler, Catal. Today 42 (1998) 73-83.
[65] S. Brandenberger, O. Kröcher, A. Tissler, R. Althoff, Applied Catalysis B: Environmental 95 (2010) 348-357.
[66] S. Andonova, E. Vovk, J. Sjöblom, E. Ozensoy, L. Olsson, Applied Catalysis B: Environmental 147 (2014) 251-263.
[67] S.S.R. Putluru, A. Riisager, R. Fehrmann, Applied Catalysis B: Environmental 101 (2011) 183-188.
[68] M. Schwidder, M.S. Kumar, K. Klementiev, M.M. Pohl, A. Bruckner, W. Grunert, J. Catal. 231 (2005) 314-330.
[69] M.S. Kumar, M. Schwidder, W. Grünert, A. Brückner, J. Catal. 227 (2004) 384-397.
[70] L. Capek, V. Kreibich, J. Dedecek, T. Grygar, B. Wichterlova, Z. Sobalik, J.A. Martens, R. Brosius, V. Tokarova, Microporous Mesoporous Mat. 80 (2005) 279-289.
[71] L.B. Gutierrez, E.E. Miro, M.A. Ulla, Appl. Catal. A-Gen. 321 (2007) 7-16.
[72] M. Devadas, O. Kröcher, M. Elsener, A. Wokaun, G. Mitrikas, N. Söger, M. Pfeifer, Y. Demel, L. Mussmann, Catal. Today 119 (2007) 137-144.
[73] F. Kapteijn, J. RodriguezMirasol, J.A. Moulijn, Appl. Catal. B-Environ. 9 (1996) 25-64.

[74] S. Brandenberger, O. Kröcher, M. Casapu, A. Tissler, R. Althoff, Applied Catalysis B: Environmental 101 (2011) 649-659.
[75] K. Krishna, M. Makkee, Catal. Today 114 (2006) 23-30.
[76] B. Moden, J.M. Donohue, W.E. Cormier, H.X. Li, Top. Catal. 53 (2010) 1367-1373.
[77] T.J. Wallington, E.W. Kaiser, J.T. Farrell, Chemical Society Reviews 35 (2006) 335-347.
[78] L. Ponti, A.P. Gutierrez, Bulletin of Science, Technology & Society 29 (2009) 493-504.
[79] F. Castellino, S.B. Rasmussen, A.D. Jensen, J.E. Johnsson, R. Fehrmann, Applied Catalysis B: Environmental 83 (2008) 110-122.
[80] A. Lindholm, Kinetic Studies of NOx Storage and Reduction Catalysts : Flow rector experiments and microkinetic modeling, Department of Chemical and Biological Engineering, Chalmers University of Technology, Gothenburg, 2009.
[81] M. Colombo, I. Nova, E. Tronconi, Chemical Engineering Science 75 (2012) 75-83.
[82] E. Fridell, M. Skoglundh, B. Westerberg, S. Johansson, G. Smedler, J. Catal. 183 (1999) 196-209.
[83] S. Salasc, M. Skoglundh, E. Fridell, Applied Catalysis B: Environmental 36 (2002) 145-160.
[84] B. Westerberg, E. Fridell, Journal of Molecular Catalysis A: Chemical 165 (2001) 249-263.
[85] N. Takahashi, H. Shinjoh, T. Iijima, T. Suzuki, K. Yamazaki, K. Yokota, H. Suzuki, N. Miyoshi, S.-i. Matsumoto, T. Tanizawa, T. Tanaka, S.-s. Tateishi, K. Kasahara, Catal. Today 27 (1996) 63-69.
[86] T. Kobayashi, T. Yamada, K. Kayano, SAE Int. J. Engines 97-07-45 (1997).
[87] L. Olsson, H. Persson, E. Fridell, M. Skoglundh, B. Andersson, The Journal of Physical Chemistry B 105 (2001) 6895-6906.
[88] L. Olsson, R.J. Blint, E. Fridell, Industrial & Engineering Chemistry Research 44 (2005) 3021-3032.
[89] M. Colombo, I. Nova, E. Tronconi, V. Schmeißer, B. Bandl-Konrad, L.R. Zimmermann, Applied Catalysis B: Environmental 142–143 (2013) 337-343.
[90] Z. Huang, X. Gu, W. Wen, P. Hu, M. Makkee, H. Lin, F. Kapteijn, X. Tang, Angewandte Chemie International Edition 52 (2013) 660-664.
[91] A. Lindholm, H. Sjövall, L. Olsson, Applied Catalysis B: Environmental 98 (2010) 112-121.
[92] J.W. Niemantsverdriet, Spectroscopy in Catalysis An Introduction, 4 ed., Wiley-VCH, Weinheim, 2007.
[93] S. Brunauer, P.H. Emmett, E. Teller, Journal of the American Chemical Society 60 (1938) 309-319.
[94] AVL BOOST Aftertreatment manual, AVL, www.avl.com, 2011.

[95] L. Olsson, H. Sjövall, R.J. Blint, Applied Catalysis B: Environmental 81 (2008) 203-217.
[96] J.R. Welty, C.E. Wicks, R.E. Wilson, G. Rorrer, Fundamentals of Momentum, Heat, and Mass Transfer, John Wiley & Sons, Inc, USA, 2001.
[97] S. Malmberg, M. Votsmeier, J. Gieshoff, N. Soger, L. Mussmann, A. Schuler, A. Drochner, Top. Catal. 42-43 (2007) 33-36.
[98] H. Sjövall, R.J. Blint, L. Olsson, The Journal of Physical Chemistry C 113 (2009) 1393-1405.
[99] AVL DoE and Optimization manual, AVL, www.avl.com, 2011.
[100] J.A. Dumesic, R. Dale F, A. Luis M, R. James E, T. A.A, The Microkinetics of Heterogeneous Catalysis, American Chemical Society, Washington, D.C, 1993.
[101] S. Brandenberger, O. Kröcher, A. Wokaun, A. Tissler, R. Althoff, J. Catal. 268 (2009) 297-306.
[102] I. Nova, C. Ciardelli, E. Tronconi, D. Chatterjee, B. Bandl-Konrad, Aiche J. 52 (2006) 3222-3233.
[103] R.R. Pinto, P. Borges, M. Lemos, F. Lemos, J.C. Vedrine, E.G. Derouane, F.R. Ribeiro, Appl. Catal. A-Gen. 284 (2005) 39-46.
[104] M. Hoj, M.J. Beier, J.D. Grunwaldt, S. Dahl, Appl. Catal. B-Environ. 93 (2009) 166-176.
[105] G. Delahay, D. Valade, A. Guzman-Vargas, B. Coq, Appl. Catal. B-Environ. 55 (2005) 149-155.
[106] D. Klukowski, P. Balle, B. Geiger, S. Wagloehner, S. Kureti, B. Kimmerle, A. Baiker, J.D. Grunwaldt, Applied Catalysis B: Environmental 93 (2009) 185-193.
[107] G.S. Qi, R.T. Yang, Appl. Catal. B-Environ. 60 (2005) 13-22.
[108] P.E. Petit, F. Farges, M. Wilke, V.A. Sole, J. Synchrot. Radiat. 8 (2001) 952-954.
[109] G. Mul, M.W. Zandbergen, F. Kapteijn, J.A. Moulijn, J. Perez-Ramirez, Catal. Lett. 93 (2004) 113-120.
[110] G. Mul, J. Perez-Ramirez, F. Kapteijn, J.A. Moulijn, Catal. Lett. 80 (2002) 129-138.
[111] G. Spoto, A. Zecchina, G. Berlier, S. Bordiga, M.G. Clerici, L. Basini, J. Mol. Catal. A-Chem. 158 (2000) 107-114.
[112] K. Segawa, Y. Chen, J.E. Kubsh, W.N. Delgass, J.A. Dumesic, W.K. Hall, J. Catal. 76 (1982) 112-132.
[113] G. Grubert, M.J. Hudson, R.W. Joyner, M. Stockenhuber, J. Catal. 196 (2000) 126-133.
[114] S.M. Park, G. Seo, Y.S. Yoo, H.S. Han, Korean J. Chem. Eng. 27 (2010) 1738-1743.
[115] M. Iwasaki, K. Yamazaki, K. Banno, H. Shinjoh, J. Catal. 260 (2008) 205-216.

[116] M. Santhosh Kumar, M. Schwidder, W. Grünert, U. Bentrup, A. Brückner, J. Catal. 239 (2006) 173-186.
[117] G.D. Pirngruber, P.K. Roy, N. Weiher, J. Phys. Chem. B 108 (2004) 13746-13754.
[118] Y. Tamura, S. Kikuchi, K. Okada, K. Koga, T. Dogahara, O. Nakayama, H. Ando, Development of Advanced Emission-Control Technologies for Gasoline Direct-Injection Engines, SAE International, 2001.
[119] D. Dou, J. Balland, Impact of Alkali Metals on the Performance and Mechanical Properties of NOx Adsorber Catalysts, SAE International, 2002.
[120] T.J. Toops, D.B. Smith, W.P. Partridge, Applied Catalysis B: Environmental 58 (2005) 245-254.
[121] T.J. Toops, D.B. Smith, W.S. Epling, J.E. Parks, W.P. Partridge, Applied Catalysis B: Environmental 58 (2005) 255-264.
[122] M. Colombo, G. Koltsakis, I. Nova, E. Tronconi, Catal. Today (2011).
[123] C. Busco, A. Barbaglia, M. Broyer, V. Bolis, G.M. Foddanu, P. Ugliengo, Thermochim. Acta 418 (2004) 3-9.
[124] N. Wilken, K. Wijayanti, K. Kamasamudram, N.W. Currier, R. Vedaiyan, A. Yezerets, L. Olsson, Applied Catalysis B, Environmental 111-112 (2012) 58-66.
[125] H. Sjövall, R.J. Blint, L. Olsson, Applied Catalysis B: Environmental 92 (2009) 138-153.
[126] I. Nova, M. Colombo, E. Tronconi, Oil Gas Sci. Technol. 66 (2011) 681-691.
[127] A. Lindholm, N.W. Currier, J.H. Li, A. Yezerets, L. Olsson, J. Catal. 258 (2008) 273-288.
[128] R. Nedyalkova, K. Kamasamudram, N.W. Currier, J. Li, A. Yezerets, L. Olsson, J. Catal. 299 (2013) 101-108.
[129] O. Kröcher, M. Elsener, Applied Catalysis B: Environmental 77 (2008) 215-227.
[130] A.V. Kucherov, A.A. Slinkin, Zeolites 6 (1986) 175-180.
[131] Y. Zheng, Y. Liu, M.P. Harold, D. Luss, Applied Catalysis B: Environmental 148–149 (2014) 311-321.
[132] J.A. Pihl, J.E. Parks, C.S. Daw, T.W. Root, Product Selectivity During Regeneration of Lean NOx Trap Catalysts, SAE Technical Paper 2006-01-3441, 2006.
[133] C.D. DiGiulio, J.A. Pihl, J.E.P. Ii, M.D. Amiridis, T.J. Toops, Catal. Today 231 (2014) 33-45.
[134] E.C. Adams, M. Skoglundh, M. Folic, E.C. Bendixen, P. Gabrielsson, P.-A. Carlsson, Applied Catalysis B: Environmental 165 (2015) 10-19.